2022

Pushing the physical limits of infrared chemical imaging: intravascular photoacoustic & mid-infrared photothermal

BOSTON UNIVERSITY

GRADUATE SCHOOL OF ARTS AND SCIENCES

Dissertation

PUSHING THE PHYSICAL LIMITS OF INFRARED CHEMICAL IMAGING: INTRAVASCULAR PHOTOACOUSTIC & MID-INFRARED PHOTOTHERMAL

by

YI ZHANG

B.S., University of Science and Technology of China, 2015

Submitted in partial fulfillment of the

requirements for the degree of

Doctor of Philosophy

2022

Approved by

First Reader

Ji-Xin Cheng, Ph.D.
Professor of Biomedical Engineering
Professor of Electrical and Computer Engineering

Second Reader

Jerome C. Mertz, Ph.D.
Professor of Biomedical Engineering

Third Reader

Shyamsunder Erramilli, Ph.D.
Professor of Physics

Fourth Reader

Kenneth Rothschild, Ph.D.
Professor of Physics

DEDICATION

I would like to dedicate this work to my parents

ACKNOWLEDGMENTS

First and foremost, I am extremely grateful to my supervisor, Prof. Ji-Xin Cheng for their invaluable advice, continuous support and patience during my PhD study. His immense knowledge and plentiful experience have encouraged me in all the time of my academic research and daily life. I am honored to have Dr. Jerome Mertz, Dr. Shyamsunde Eramilli, Dr. Kenneth Rothschild, and Dr. Joseph Larkin as my committee members, who have been extremely helpful on my thesis work.

I would like to thank all the members, past and present, of the Cheng group. It is their kind help and support that have made my study and life here a wonderful time. I would like to thank Dr. Xiaojie Li, Dr. Jie Hui for the tremendous help on instrumentation. I am very grateful for the support in biology from Dr. Meng Zhang, Dr. Cheng Zong, Dr. Celalettin Yuradkul, Dr. Jian Zhao, Haonan Zong, Yuying Tan, Yuewei Zhan, and Linli Shi for the constructive discussions or contributions to my work. In addition, I would like to thank our collaborators from the James Hamilton lab, Lei Tian Lab for the productive collaborations. Finally, I would like to express my gratitude to my parents. Without their tremendous understanding and encouragement in the past few years, it would be impossible for me to complete my study.

PUSHING THE PHYSICAL LIMITS OF INFRARED CHEMICAL IMAGING

YI ZHANG

Boston University, Graduate School of Arts and Sciences, 2022

Major Professor: Ji-Xin Cheng, Ph.D.
Moustakas Chair Professor in Photonics and Optoelectronics
Professor of Biomedical Engineering
Professor of Electrical and Computer Engineering
Professor of Materials Science and Engineering
Professor of Chemistry
Professor of Physics

ABSTRACT

Providing molecular fingerprint information, vibrational spectroscopy is a powerful tool for chemical analysis. In the mid-infrared window, FT-IR spectroscopy and microscopy has been routinely used for sample characterization. In the near-IR window, near infrared spectroscopy has been widely used for tissue analysis and for detection of lipids in arterial wall. Yet, these traditional linear spectroscopies have intrinsic limitations. FT-IR spectroscopy suffers from a poor spatial resolution and strong water absorption for study of living systems. Near infrared spectroscopy avoids water absorption, yet it suffers from a poor, millimeter-scale spatial resolution in tissue analysis. My thesis focuses on breaking these limitations through photoacoustic and photothermal detection approaches.

The first part of my thesis is on improving the spatial resolution in catheter-based intravascular photoacoustic (IVPA) imaging. By near-infrared excitation of lipids and acoustic detection, IVPA allows depth-resolved identification of lipid-laden atherosclerotic plaque. Thus far, most IVPA endoscopes use multimode fibers, which do not allow tight focusing of photons. Recent experiments on pulse propagation in

multimode graded-index fibers have shown a nonlinear improvement in beam quality. Here, we harness this nonlinear phenomenon for fiber-delivery of nanosecond laser pulses. We built a photoacoustic catheter 1.4 mm outer diameter, offering a lateral resolution as fine as 30 μm within a depth range of 2.5 mm. Such resolution is one order of magnitude better than current multi-mode fiber based intravascular photoacoustic catheters. At the same time, the delivered pulse energy can reach as high as 20 μJ, which is two orders of magnitude higher than that of an optical resolution photoacoustic endoscope built with a single mode fiber. These improvements are expected to promote the biomedical application of photoacoustic endoscopes which require both high resolution and high pulse energy. Based on the technical advanced, my thesis work further demonstrated longitudinal imaging of the same plaque in the same living animal.

Recently developed mid-infrared photothermal (MIP) microscopy overcomes the limitations in FT-IR microscopy by probing the IR absorption-induced photothermal effect using a visible light. MIP microscopy yields sub-micrometer spatial resolution with high spectral fidelity and much reduced water background. The second part of my thesis work pushes the physical limits of MIP microscopy in aspects of detection sensitivity and imaging speed using two approaches. First, taking advantage of the interference scattering effect, the scattering signal from the sample can be greatly enhanced. Together with the relatively large infrared absorption coefficient, the sensitivity of infrared spectrum is greatly improved and single virus detection is achieved. Second, by using fluorescence as

a thermo-sensitive probe, the temperature raise by infrared absorption can be retrieved in a more efficient way and much higher imaging speed and sensitivity is thus accomplished.

PREFACE

The basis for this research originally stemmed from my passion for developing better methods of observing the Microcosm. The desire of see the construction of a complex biosystem down to the atom level and its highly organized arrangement, which may unravel the mystery of the complex system operation. It is my passion to not only find out, but to develop tools to break down barriers of accessibility for future generation.

In truth, I could not have achieved my current level of success without a strong support group. First of all, my parents, who supported me with love and understanding. And secondly, my committee members, each of whom has provided patient advice and guidance throughout the research process. Thank you all for your unwavering support.

TABLE OF CONTENTS

LIST OF FIGURES

CHAPTER ONE - INTRODUCTION

1.1 Advanced Detection of Molecular Vibrational Spectroscopy

Vibrational spectroscopy is a method for direct measurement of specific chemical bonds of absorbed atoms and molecules. Almost any compound having covalent bonds, whether organic or inorganic, absorbs various frequencies of electromagnetic radiation in the infrared region of the electromagnetic spectrum.

There are two kinds of vibrational spectroscopy, one is mid-infrared spectroscopy, which is widely used for chemical analysis, and the other is near-infrared spectroscopy, which has been used for lipid plaque detection. Each has its advantages and limitations, and my thesis work aimed to overcome these limitations through developing advanced infrared absorption detection methods.

The first method is photoacoustic detection. Photoacoustic imaging is a noninvasive technology that utilizes optical absorption (electronic or vibrational) and ultrasonic detection to map biological tissue at centimeter depths. The quantized vibration of chemical bonds provides a way of targeting specific molecules in a complex tissue environment. Based on near infrared overtone absorption, intravascular photoacoustic catheters are developed for mapping lipids deposited inside the lumen of a blood vessel. However, current intravascular photoacoustic system suffers from limited spatial resolution, decided by ultrasound. My thesis work aimed to improve the resolution to optical resolution in a catheter-based design.

The second method is photothermal detection. Mid-Infrared spectroscopic imaging using inherent vibrational contrast is a powerful analytical tool for sample identification

and characterization. Yet, the low spatial resolution and large water absorption associated with the long IR wavelengths hinder its biological applications. Recently developed mid-infrared photothermal (MIP) microscopy overcomes these limitations by probing the IR absorption-induced photothermal effect, but still suffers from low modulation depth. My thesis work aimed to improve the sensitivity and selectively of the mid-infrared photothermal method by introducing fluorescence as the sensitive thermal sensor.

1.2 Intravascular Photoacoustic Imaging

Atherosclerosis is a long-term, systematic disease characterized by plaques building up in the blood vessel wall. The disease claims tens of thousands of lives in the U.S. each year[1]. The rupture of vulnerable atherosclerotic plaques is a major contributor to acute cardiovascular events and sudden cardiac deaths[2]. The vulnerability of an atherosclerotic plaque, its susceptibility to rupture, is known to be related to the composition of the plaque, the distribution of mechanical stress within it, and the presence and extent of associated inflammation[3]. One of the most common types of vulnerable plaques is the thin cap fibroatheroma. These lesions are characterized by a thin fibrous cap, weakened by the presence of macrophages, covering a lipid-rich necrotic core. Rupture of the cap due to high mechanical stress will release the thrombogenic contents of the necrotic core into the bloodstream. The subsequent formation of a platelet-rich thrombus may result in occlusion, either at the location of the rupture or downstream from the lesion site. If this occlusion takes place in a coronary artery, the result may be unstable angina or a myocardial infarction[4].

Intravascular photoacoustic (IVPA) is the most recent addition to spectroscopic diagnostic techniques applied to atherosclerosis. IVPA has the ability to directly image tissue components in the vessel wall, with high chemical specificity for lipid type. In photoacoustic (PA) imaging, the tissue is irradiated by short laser pulses with a duration of several nanoseconds. Absorption of laser light transfers the optical energy to the tissue, which causes a transient pressure rise[5]. This initial pressure rise acts as an acoustic source that generates a broadband wave propagating through the tissue. The acoustic wave can be detected with an ultrasound transducer. The image can be created by scanning the optical beam and deriving depth resolution from the time of flight of the ultrasound wave. In IVPA, this principle needs to be miniaturized to fit on a catheter. Light is delivered through an optical fiber, while signal detection is performed by the same type of ultrasound transducer that is used in IVUS.

The goal of IVPA imaging is the chemical characterization of vessel wall components. Introduction of infrared sources prompted investigation of a wider range of excitation wavelengths (680-1800 nm). Blood absorption is especially low in the wavelength range from 680 – 1300 nm. In this wavelength range, the absorption spectrum of lipids exhibits a large peak around 1210. IVPA imaging at 1720 nm was also demonstrated on human coronary atherosclerosis[6]. And show that in-vivo imaging without flushing the blood from the artery is possible. In most IVPA experiments, lipid rich atherosclerotic plaques were distinguished from normal arterial tissue by simply comparing the tissue spectral signature to the absorption spectra of lipids. A more

sophisticated spectroscopy inversion approach could provide robust identification of a wider range of tissue types, including collagen, elastin and calcification.

Introduction to mid-infrared photothermal microscopy

Mid-infrared (IR) spectroscopy has become a versatile molecular analysis tool. Every molecule has slightly different vibrational modes from all other molecules. Thus, the infrared spectrum of a given molecule is unique and can be used to identify that molecule. Infrared spectra give far more detailed information than simply allowing the presence or absence of certain functional groups to be recognized.

The recently developed mid-infrared photothermal (MIP) microscopy not only overcomes the diffraction limit in far-field IR imaging but also circumvents the limitations in AFM-IR. In MIP microscopy, a visible beam probes the thermal effects induced by an intensity-modulated IR beam. The thermal effects induced by an intensity-modulated IR beam. The thermal effects include thermal expansion, pressure wave emission, refractive index change, and Gruneisen parameter change. Unlike the direct measurement of the absorption in IR spectroscopy, the temperature rise induced by photothermal effect is the origin of MIP signal. In addition, water background is reduced since it has a large heat capacity, resulting in a small temperature increase. Moreover, water has relatively low thermo-optic and thermal expansion coefficients, resulting in a small MIP back-ground. These properties allow MIP imaging of intact specimens in liquid environment including living cells, which is beyond the reach of the direct IR and AFM-IR technologies. The MIP signals can be measured by a transmission dark-field

geometry[7-8], by reflection[9], interferometrically[10] and acoustically in a stage scanning mode[11]. The MIP effect can be measured in a widefield manner through an interferometric reflectance microscope, a quantitative phase microscope, or a low-coherence interferometric microscope. In the widefield MIP, the IR pump beam is weakly focused onto the sample that is illuminated by the visible probe beam in Kohler arrangement. A complementary metal-oxide semiconductor (CMOS) camera enables multiplex signal readout, which drastically improves the imaging speed. Moreover, thermal confinement after a short IR pulse excitation offers sub micrometer spatial resolution.

The MIP signal originates from a nonradiative relaxation process that happens in an absorber after IR photon excitation. The absorbed energy dispersed into the form of heat results in a local temperature increase, which changes the sample's optophysical properties[12] and is detectable by various mechanisms. Previously developed visible photothermal microscopy for imaging nano-objects with electronic absorption introduced comprehensive theories and physical models to explain the signal's origin and push the sensitivity limit down to single molecules in room temperature. In these models, nano-absorbers are treated as a point heat source, and a thermal transfer medium around the objects is carefully selected to enhance the signal. Therefore, the photothermal contrast is mainly originated from the refractive index modulation of the surrounding medium, other than the nano-objects themselves. Differently, the MIP microscopy is based on vibrational absorption; the target size is typically comparable with the diffraction limit spot of the visible probe beam, and the target itself acts as a signal source. This feature

enables the detection of the MIP signal by temperature-sensitive optical methods without a need for a thermal medium. On the instrumentation side, a sinusoidal modulation is typically applied to the pump beam in the electronic absorption-based photothermal systems to create a time-dependent temperature gradient, and a lock-in amplifier is used to extract this periodically modulated signal. In comparison, the MIP systems deploy a pulsed IR source, which can provide a heat confinement that results in a larger signal a higher spatial resolution compared with sinusoidal modulation. Therefore, an independent description of contrast mechanism is needed for MIP microscopy.

The major type of MIP mechanism is based on optical scattering, and the MIP signal is generated from the scattering intensity difference between IR on and IR off states. Therefor, a dark field geometry can be applied to minimize the unchanged illumination background and increase the signal-to-noise ratio (SNR) accordingly. The group of Hartland and Kuno have modeled scattering in a MIP system and compared the contribution of particle size and refractive index to signal generation[13].

Introduction to fluorescent detected mid-infrared photothermal microscopy

Despites the successes of MIP, MIP measured by perturbation of a probe beam suffers from several limitations. First, refractive index is a fairly weak function of temperature, changing by ~0.01% per Kelvin for water at room temperature[14]. Second, it is well-known that the photothermally induced deflection of a probe beam in transmission approaches zero for a point source centered in the probe beam focus and is maximized with an axial offset between the probe beam and photothermal lens of $\sqrt{3}\,Z_0$ (Z_0 is the

Rayleigh range, equal to half the depth of focus)[15]. As such, an MIP measurement of a point source along the optical axis based on detection of beam deflection is only expected to produce peak signals in homogeneous media when the probe beam focus is displaced by nearly full depth of field relative to the photothermal source, potentially producing nontrivial 3D point spread functions. The whole path for the optical detection beam may be influenced by the mid-infrared pump, leading to refractive index change. Thus, it can be hard to calculate the accurate z position which leads the change.

Many pharmaceutical materials exhibit significant turbidity and heterogeneity, creating challenges for analytically modeling and interpreting photothermal changes in backscattered intensity from chemically and physically heterogeneous samples. In many instances, the optical constants associated with temperature change are not known, complicating quantitative interpretation of the magnitude of MIP responses. Furthermore, the detected backscattered signal can depend on both depolarization and scattering in ways that may depend nontrivially on the particle size distribution within compacted or powdered samples.

We explore the potential viability of using fluorescence intensity to detect local changes in temperature induced by mid-infrared absorption. The quantum efficiency of fluorescence is well established to vary sensitively with temperature[16]. Virtually all luminescent molecules and materials display a T-dependent emission[17]. This is due to the Boltzmann distribution, and the dependence on T is a function of the specific electronic band structure of the material. At higher Ts, thermal energy excites the electrons within the excited states transitions to the electronic states with varying vibrational levels that

are overlapping at different energy levels, so that non-radiative decays become possible. The rate of non-radiative transitions is related to T via the Arrhenius equation:

$$k_{nrt} \sim e^{-\frac{\Delta E}{kT}}$$

Where ΔE is the energy gap between the lowest level of the excited state and the overlap point to a possible non-radiative decay state, and k is the Boltzmann constant. The quantum yield (QY) of luminescence represents the ratio of the number of emitted photons to the number of excited photons. It decreases with T according to:

$$QY = \frac{\Gamma}{\Gamma + \mathrm{k_{nrt}}}$$

Where Γ represents the emissive rate of the luminophore. The luminescence lifetime (decay time) is defined as the average time a luminophore remains in its excited state prior to deactivation. Lifetime is thermally quenched with increasing T via:

$$\tau = \frac{1}{\Gamma + k_{nrt}}$$

As the T around the fluorophore undergoes changes, its intensity, decay lifetime, spectral positions and shape, and polarization may alter. These effects make all probes be T-sensitive probes to some extent.

Luminescent molecular probes enable high spatial resolution and have a fast response, often in a time scale comparable to that of cellular processes. Several features are desirable for a good T-sensitive probe: (a) the signal is expected to undergo a large change with T; implies good sensitivity. (b) Absorption and emission should occur at long wavelengths so as to reduce interferences by the intrinsic color or fluorescence of samples which is strong in the UV or under UV and shortwave visible photoexcitation.

(c) The probes should display good photostability so as to enable long-term monitoring without any photodecomposition during optical interrogation. (d) The probes must not be toxic if an in vivo use is intended. (e) High brightness, defined as the product of QY and molar absorbance is a highly desirable parameter and supposed to be >20000, ideally > 100000 $cm\ M^{-1}$.

Rhodamine and its derivatives have long been known for the sensitivity of their fluorescence to T. The rhodamine family of fluorophores displays high quantum yields, brightness, and excitation bands in the visible range. The quantum yield of rhodamine B is highly T-dependent, in that its quantum yield decreases with an increase in T up to 373 K[18]. Their luminescence dependency on T is particularly expressed in the range from 272 to 373 K. These features make them most suitable as molecular probes for sensing T in microfluidic devices, cells, or in planar sensor films. Fluorescein is another highly luminescent probe with a quantum yield of almost 1. Fluorescein and its derivatives are mainly used as pH probes. Like all the other fluorophores, fluorescein also undergoes thermal quenching at elevated T. It was covalently linked to starch and its response to T and pH was studied in detail. The material responds linearly to T in the range from 273 to 333 K.

Following optical excitation, increases in temperature enable access to a greater suite of thermally accessible relaxation pathways, all of which compete with fluorescence for a net reduction in fluorescence intensity. Temperature-dependent changes in autofluorescence emission have been reported in microscale thermophoresis, which target measurements of protein mobility and thermal stability[19]. Compared to refractive index

change, the change in fluorescence quantum efficiency can be quite large, routinely changing by ~2-3%/K for tryptophan and ~1-2%/K for aqueous solution of rhodamine B, corresponding to an ~100 fold higher relative change than refractive index detection. Given the high signal-to-noise with which fluorescence measurements are regularly recorded, this sensitivity has the potential to be more than sufficient to enable fluorescence detection of local temperature perturbations of <1K induced by mid-infrared absorption.

The F-MIP is distinct from prior studies on fluorescence encoded IR by Tokmakoff and co-workers, based on IR+Vis two photon excited fluorescence. In FE-IR spectroscopy, the infrared absorber must necessarily be energetically coupled to the electronic transition to support coherent two photon absorption, with corresponding improvements in selectivity for particular fluorophores of interest. As such, FEIR provides information on strongly coupled vibrational modes. FEIR spectroscopy operates by the double resonance. An IR pulse or pulse pair resonantly drives vibrations into their first excited state, after which an electronically preresonant visible pulse selectively brings the fluorophore to its electronic excited state. The resulting fluorescence emission intensity is therefore dependent on the excited vibrational population created by the IR field on the ground electronic state and is used as an action signal that encodes vibrational information. In practice, the weak IR-vibrational absorption cross sections and picosecond lifetimes necessitate intense pulse with comparable or shorter durations to ensure the overall excitation process is competitive against relaxation. Furthermore, high repetition rates benefit single-photon counting but must be balanced with the technical

requirements of generating intense, ultrashort mid-IR pulses and potential heating artifacts.

Volumetric fluorescent detected mid-infrared photothermal microscopy

Observing the various anatomical and functional information that spans many spatiotemporal scales with high resolution provides deep understanding of the fundamentals of biological systems. This is especially important for the chemically imaging of the components inside the cell.

Attempts have been made to utilize the vast potential of mid-IR. Despite these important advances in MIP, the total acquisition time for volumetric images is still rather long and relies on lateral raster scanning of the beam, rendering current approaches less practical for time-sensitive applications. Furthermore, signal levels appear insufficient for examining weak signal in organic materials. Here, we apply the Fourier light field microscope technique combined with F-MIP to achieve fast and high sensitivity 3D chemical imaging.

Light -field microscopy simultaneously captures both the 2D spatial and 2D angular information of the incident light, allowing computational reconstruction of the full 3D volume of a specimen from a single camera frame. Recently, Fourier imaging schemes have been proposed as a promising path to improve the current LFM techniques. The FLFM achieved high-quality imaging and rapid light-field

reconstruction. By recording the 4D light field in the Fourier domain, and the fluorescence intensity modulation by the infrared in time domain, the volumetric chemical imaging is achieved.

CHAPTER TWO - HIGH-RESOLUTION PHOTOACOUSTIC ENDOSCOPE THROUGH BEAM SELF-CLENANING IN A GRADED INDEX FIBER

The work in this chapter was published in Optica Letters[20]. Reprinted with permission form the Optical Society publishing group.

Intravascular photoacoustic imaging can potentially improve the identification of lipid-laden atherosclerotic plaque. Most intravascular photoacoustic endoscopes use multimode fibers, which do not allow tight focusing of photons. Recent experiments on pulse propagation in multimode graded-index fibers have shown a nonlinear improvement in beam quality. Here, we harness this nonlinear phenomenon for fiber-delivery of nanosecond laser pulses. We built a photoacoustic catheter 1.4 mm outer diameter, offering a lateral resolution as fine as 30 μm within a depth range of 2.5 mm. Such resolution is one order of magnitude better than current multimode fiber-based intravascular photoacoustic catheters. At the same time, the delivered pulse energy can reach as high as 20 μJ, which is two orders of magnitude higher than that of an optical resolution photoacoustic endoscope built with a single mode fiber. These improvements are expected to promote the biomedical application of photoacoustic endoscopes which require both high resolution and high pulse energy.

Introduction

Light self-cleaning and its application

A photoacoustic endoscope, which embodies photoacoustic imaging in a miniaturized probe, can provide depth-resolved imaging of an internal organ with optical contrast[21-24]. This technique has shown great potential for the detection of colon cancer[25] and lipid-laden plaques[26-27]. In most cases, a step-index multimode fiber (MMF) is used to allow high-energy pulse delivery; however, the spatial resolution is not optimal[28-29]. A significant problem to be solved is the effective coupling and stable transmission of a diffractionlimited beam from a single mode (SM) laser source into an MMF, where interference between the different fiber modes occurs, which results in a complex speckle pattern at the output. Such a speckle pattern prohibits tight focusing of photons through a microlens. To improve the spatial resolution, a design with the combination of a single mode fiber and a graded index (GRIN) lens was reported[30]. Nevertheless, the low laser damage threshold prohibits the use of single mode fibers for delivery of high-energy laser pulses which are often needed in high-quality photoacoustic imaging. Though the GRIN lens can tightly focus the Gaussian beam from the single-mode fiber, it cannot focus effectively a beam delivered by an MMF.

To further illustrate this issue, a simulation of the focusing effect with the GRIN lens was performed. We used the beam propagation method[22]. to analyze the performance of the GRIN lens on the Gaussian beam and the complex speckle pattern from the multimode fiber. Specifically, we adopted an aberration-free GRIN lens with a gradient constant 0.5 mm−1. Figure 2.1(a) shows that the GRIN lens can effectively focus a

Gaussian beam tightly. However, as shown in Fig. 2.1(b), the output beam from the multimode fiber has random mode and cannot be focused by a GRIN lens.

To achieve high-resolution photoacoustic imaging, we harness the reported spatial beam self-cleaning effect in a graded index multimode fiber (GRIN MMF)[31-32] to improve the beam quality significantly. Despite the high number of permitted guided modes in a GRIN MMF, light self-cleaning enables a robust, effective propagation of spatially bell-shaped beams. The self-cleaning effect can be explained by the four-wave mixing interaction among a large population of the guided modes. Spatial self-induced periodic imaging and Kerr nonlinearity create a periodic longitudinal modulation of the refractive index of the fiber core, and this permits quasi-phase matching and energy exchange between guided modes through four-wave mixing[33]. The fundamental mode shows nonreciprocal nonlinear energy exchange with the high order modes and traps all the energy transformed to it. As a result, the beam profile coalesces from a highly irregular to a well-defined bell-shaped structure in the core center. This process effectively improve the beam quality and enhances the focus. Also, spatial beam self-cleaning does not lead to frequency spectrum changes or nonlinear loss of energy. Notably, GRIN MMF with spatial beam cleaning has a larger mode area than SMF and could deliver a high-quality beam with two orders of magnitude higher laser pulse energy[34-35].

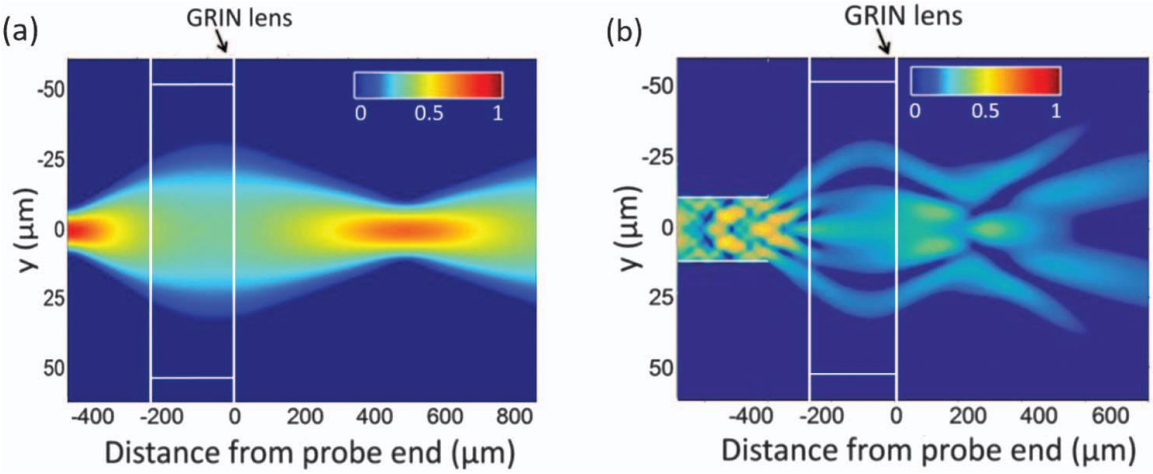

Figure 2.1 Simulation results of GRIN focusing

(a) a Gaussian beam and (b) an output beam from the step-index multimode fiber.

To our knowledge, none of the current intravascular photoacoustic endoscopes have achieved high energy pulse delivery and high resolution at the same time. For in vivo intravascular photoacoustic imaging of lipids at 1.2 or 1.7 μm[36], the signal to noise is a primary concern, where the absorption of water and the scattering of the blood significantly compromises the photoacoustic signal. By increasing the pulse energy from ~500 nJ to 20 μJ, one can effectively enhance the signal strength and thus improve the image quality.

Method

encapsulated photoacoustic endoscope based on a GRIN MMF

In this Letter, we demonstrate a fully encapsulated photoacoustic endoscope based on a GRIN MMF. Our endoscope utilizes spatial beam self-cleaning to achieve high-resolution photoacoustic imaging. Compared with previous MMF photoacoustic endoscope without light converging, this design significantly improves the imaging resolution in the lateral direction. Also, taking advantage of a much larger core size (100 μm) of the GRIN MMF, we achieved delivering pulse energy around 20 μJ, with 1000 Hz repetition rate.

The quality of the beam delivered by the GRIN MMF is crucial for the imaging system. Figure 2.1(a) shows the setup for GRIN fiber optical coupling and beam output measurement. In the setup, a 2-ns pulsed laser at 1030 nm is first cleaned by a pinhole, then launched into a 1-m GRIN fiber with 0.29 NA and a 100/140 μm core diameter (F-MLD from Newport Co.) where a lens, an ND filter (ND10A from Thorlabs), and a three-axis translation stage are used. The beam diameter is 30 μm at the fiber-tip surface, and the incident angle is less than one degree to ensure high coupling efficiency and low high-order modes (HOMs) excitation. The fiber is laid loosely on an optical table, without any stress to mitigate intermode coupling and losses through the HOMs. The near field profile and the output beam quality were measured by a CCD camera, and as a comparison, we also measured the output from a step index MMF (FG105LCA, Thorlabs, Inc.) with 105 μm core diameter on the same setup.

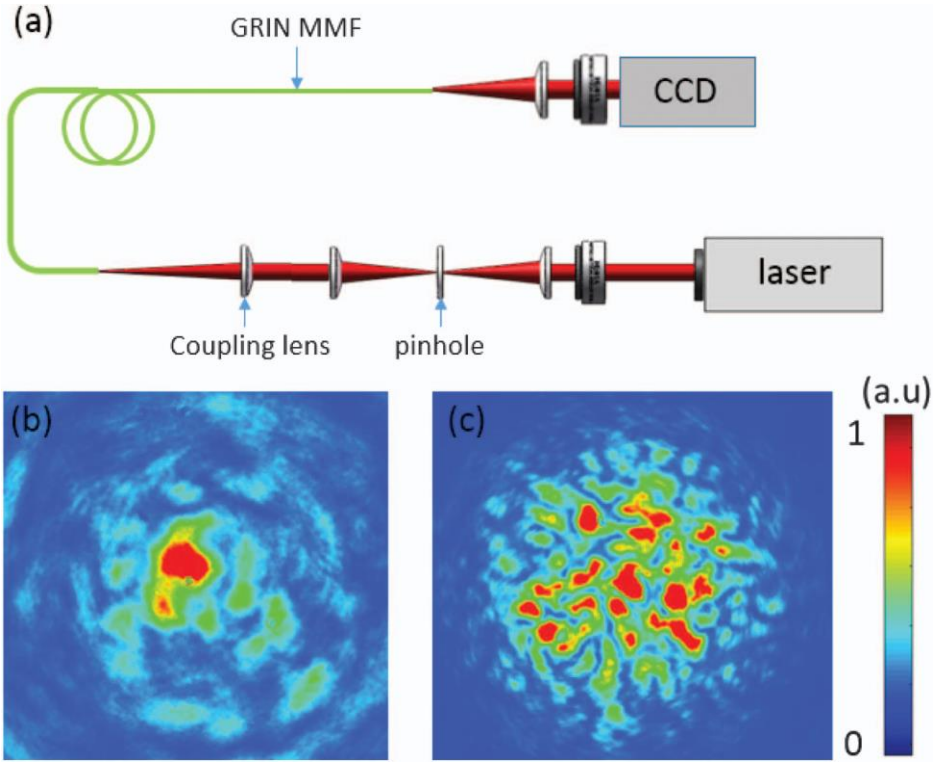

Figure 2.2 Near-field beam profiles for different input pulse energies

(a) The system setup of the fiber coupling and near field beam profile measurement. (b) Near field beam profile from a GRIN MMF. (c) Near field beam profile from a step index MMF fiber.

When we increased the input laser pulse energy above a certain level (about 1 μJ per pulse), the beam profile coalesced from a highly speckled profile to a bell-shaped structure with the majority of laser power in the center, surrounded by a low power speckled pedestal. Figure 2.2(b) shows the near field spatial beam intensity profile after coalescence at an incident pulse energy of 20 μJ. With the same setup and laser energy, we substituted the GRIN MMF with a step-index MMF, and the selfcleaning effect does not appear. As shown in Fig. 2.2(c), the smooth input Gaussian beam from the laser source degraded into the irregular transverse profile. Thus, compared with step MMF, the much-

improved spatial beam quality by the GRIN MMF paves the way toward a high - resolution photoacoustic endoscope.

Harnessing the beam self-cleaning effect, we designed a GRIN MMF based high-resolution photoacoustic endoscope illustrated in Fig. 2.3(a). A diode laser at 1030 nm wavelength is utilized as the photoacoustic excitation light source. This high pulse reputation rate (1 KHz) laser with two ns pulse width enables real-time imaging. After coupling the laser to the GRIN MMF and fine tuning it until the beam self-cleaning was achieved; the GRIN MMF is then connected to the endoscope for photoacoustic imaging. The photoacoustic signal, collected by an ultrasound transducer, transfers through the signal wire and slip ring and is amplified with a 39-dB low noise amplifier. A photodiode is used to measure the pulse energy and trigger the data acquisition card (DAQ) through the pulse generator. The photoacoustic signal collected by DAQ is saved in a PC for further data processing.

Figure 2.3(b) presents a more detailed structure of the rigid distal section and photos of several key components, respectively. The GRIN lens, fiber spacer, and the distal end of the GRIN MMF are enclosed in the 3D printed housing and completely fixed to the tube wall with epoxy. The focused laser output from the GRIN lens (GT-IFRL-085-inf-50-CC from GRINTECH) is reflected by a 0.8 mm microprism to realize side firing. Then a 42 MHz transducer (from Blatek) is installed into the reserved space, which is tilted by 10 deg. The relative position of the transducer and the prism is optimized to achieve the maximum overlap of the ultrasound focus and the laser focus, ensuring the sensitivity of the photoacoustic signal collection efficiency.

In this probe design, the converging beam from the GRIN MMF is achieved by a GRIN lens, taking advantage of its small size and easy alignment. A commercially available numerical optical modeling software ZEMAX (ZEMAX Development Corporation, Washington, USA) is used to assist the optical alignment design. With comprehensive consideration of the working distance, beam spot size, and penetration depth, the 0.25 pitch grin lens with 0.85 mm diameter and 0.8 mm homogeneous refraction index fiber spacer are chosen. According to the simulation, 2.5 mm working distance and 28 μm focusspot size can be achieved with this probe.

Volumetric photoacoustic imaging is realized by proximal rotation and pulling back of the endoscope. A fiber-optical rotary joint and slip-ring assembly, which provide optical coupling and RF signal transmission, are the key element. Figure 2.3(c) depicts the fully assembled device and the design of the fiber-optical rotary joint. The rotary part is driven by a motor via a belt. The laser transmission is realized by the direct coupling between fibers. Precise matching is required to minimize the axial misalignment.

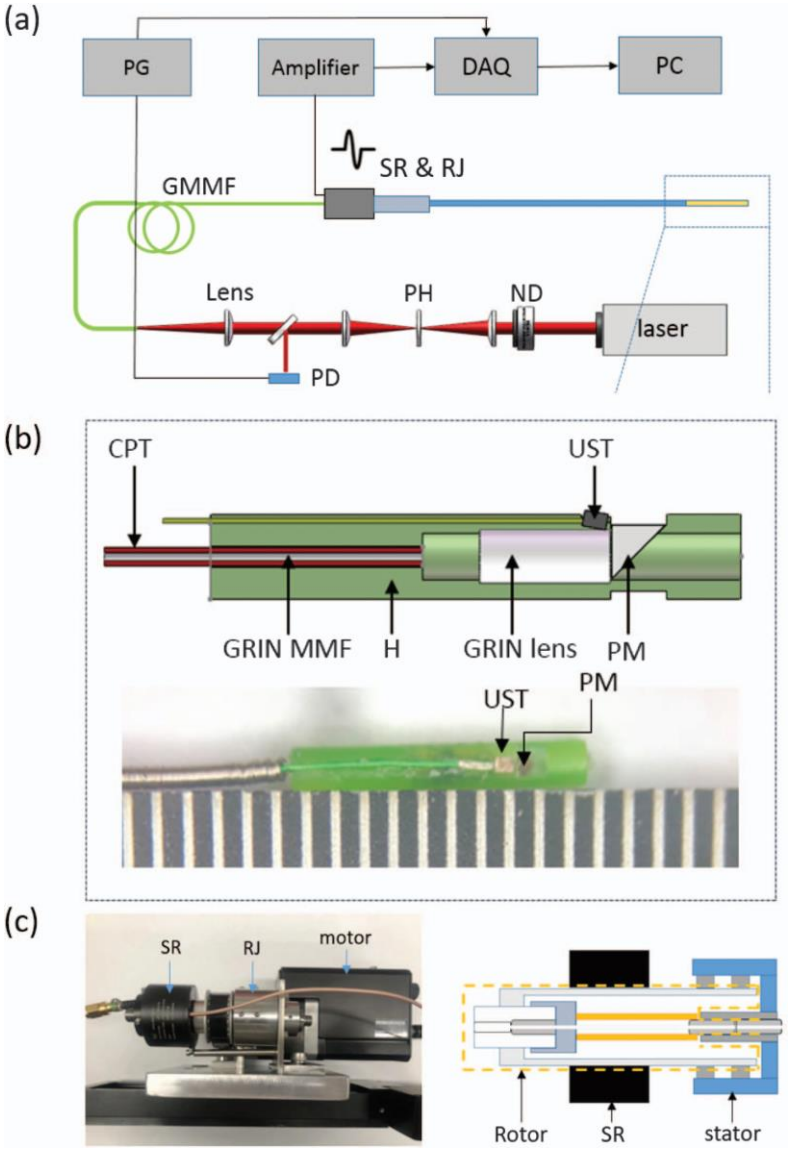

Figure 2.3 Schematic of the PA endoscope.

(a) Schematic illustration of the imaging setup with the alignment of various modules. Abbreviations: PG, a pulse generator; DAQ, data acquisition system; PD, photodiode; SR and RJ, slip ring and rotary joint; PH, pinhole. GMMF, GRIN MMF; ND, neutral density filter. (b) Architecture and photography of the endoscope. PM, prism; UST, ultrasound transducer. (c) The fiber optical rotary joint and slip-ring assembly and the schematic design of the fiber-optical rotary joint.

Results

Photoacoustic imaging of an iliac/common femoral artery stent.

The feasibility and resolution of the high-resolution photoacoustic system with GRIN MMF are first validated by a 7-μm carbon fiber phantom. The endoscope is driven by the linear stage and moves perpendicular to the carbon fiber. Photoacoustic data collected by the DAQ card are first bandpass filtered followed by Hilbert transformation. Figure 2.(a) shows the photoacoustic amplitude along the scanning direction. Furthermore, the data are fitted with the Gaussian function to estimate the spatial resolution. From the Gaussian fitting shown in Fig. 2.(c), the photoacoustic endoscope offers a lateral spatial resolution of 29.6 μm, which is ~10 times better than the previous multimode fiber-based intravascular photoacoustic endoscope [10]. The resolution along the axial direction is measured to be 96 μm, which is decided by the photoacoustic ultrasound frequency. We then substituted the GRIN fiber with a 105 μm diameter MMFand performed the same measurement. Figure 2.(b) is an image measured with step index MMF. The fitted profile is shown in Fig. 2.(d) indicates a resolution of 102 μm. These data collectively confirm the superiority of the GRIN MMF with spatial mode self-cleaning over the step index MMF.

To demonstrate 3D intravascular imaging capability of our endoscope, we used an iliac/common femoral artery stent (Boston Scientific Corporation) shown in Fig. 2.4(a), which is made up of 14 individual metallic struts (each of a diameter of 100 μm). The stent was expanded to 3.5 mm diameter, and the imaging catheter was inserted into the center of the stent. A 3D image is taken by rotating the catheter [Fig. 2.4(b)]. The

photoacoustic image in Fig. 2.4(c) and 3D reconstruction of the metabolic stent in Fig. 2.4(d) exhibit high contrast. The photoacoustic image is able to visualize fine features of the stent, such as the crossing of the struts at a high resolution.

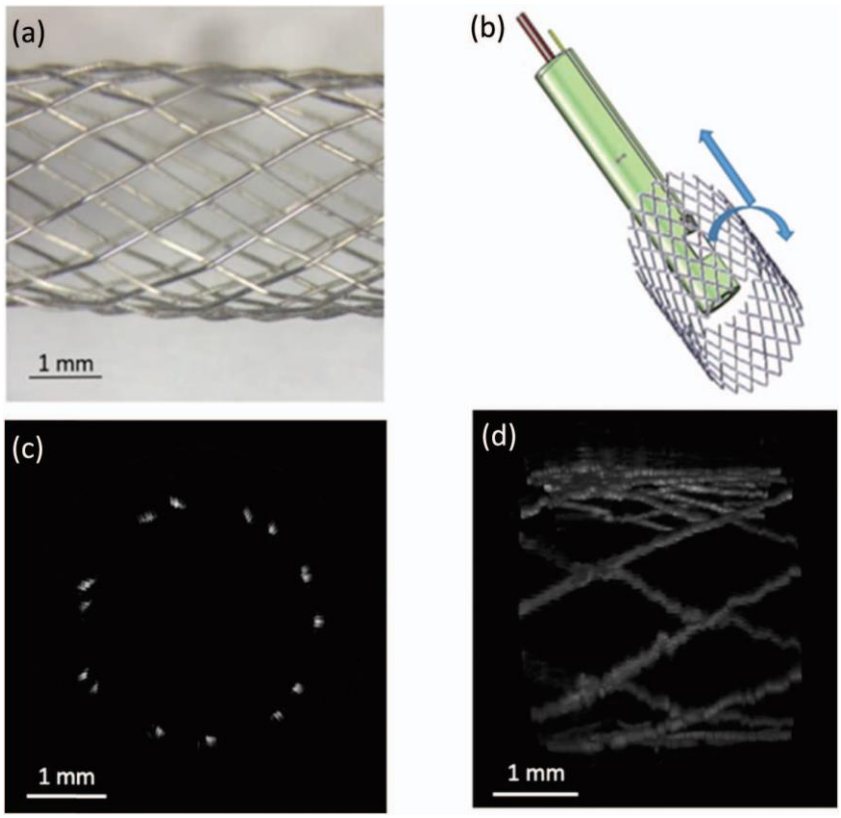

Figure 2.4 Photoacoustic imaging of an iliac/common femoral artery stent.

(a) Optical microscopic image of the imaged sent segment. (b) The schematic of the image acquisition method. (c) Photoacoustic image of a cross section of the stent. (d) Representative 3D photoacoustic image.

The improvement of the resolution with the GRIN MMF is further illustrated with a cross-sectional image of the iliac/common femoral artery stent. Figure 6 shows the photoacoustic image taken by the catheter with GRIN MMF and step index MMF. Figures 2.5(a) and 2.5(b) show the photoacoustic image of the stent with GRIN MMF.

Because of the high resolution achieved by the GRIN MMF, it shows strict edges with a width of 93 μm. Figures 2.5(c) and (d) show the photoacoustic image with step index MMF. The focus for the step MMF is not optimal, and the edges are blurred, with a width of 210 μm. These data show the improvement achieved by the GRIN MMF photoacoustic endoscope. The scale bar is 1 mm.

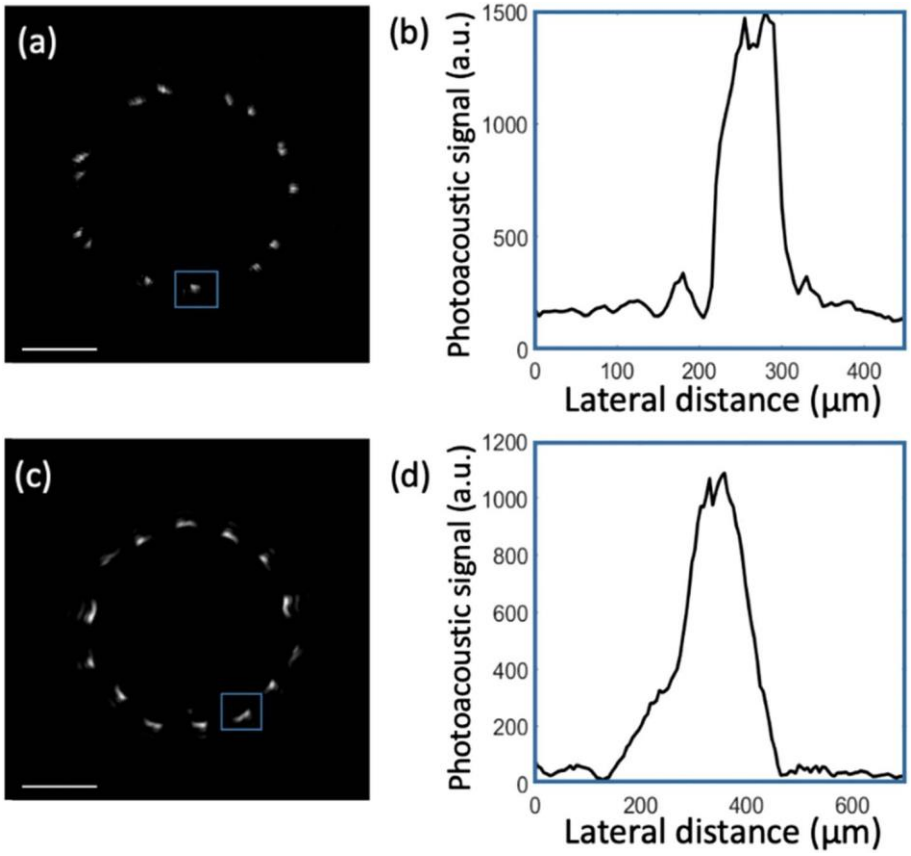

Figure 2.5 Photoacoustic and ultrasound images of the stent recorded with the catheter.

(a), (b) Photoacoustic image with the GRIN MMF and lateral resolution, (c), (d) photoacoustic image with the step index MMF and lateral resolution.

In summary, we have developed a GRIN MMF-based PA endoscope that provides a high-resolution photoacoustic image with high laser energy. The PA endoscope offers a lateral resolution of 30 μm. Unlike the previously reported highresolution PA endoscope

using SMF for light delivery, our GRIN MMF PA endoscope utilizes the spatial beam self-cleaning to keep the clean mode for a high-energy pulse. This photoacoustic endoscope design based on a GRIN MMF is also relevant for applications of self-cleaning in multimode fibers in different fields, such as three-photon imaging in fluorescence endoscopy and space division multiplexed transmission with GRIN fibers.

For future studies, to enable broad potential applications, this endoscope needs to be further downsized to a diameter smaller than 1 mm. Also, the rotary joint for the GRIN MMF should be improved to enable its ability of 3D imaging in vivo. The current design has an issue of high abrasion and cannot support high-speed rotation. GRIN MMF with a different diameter can be applied to meet the need. It is noted that due to the laser safety consideration, moderate focus with large depth of focus is preferred.

CHAPTER THREE – LONGITUDINAL INTRAVASCULAR PHOTOACOUSTIC IMAGING OF INFLAMMATORY ATHEROSCLEROTIC PLAQUE IN CHOLESTEROL FED RABBIT

The work in this chapter will be published on Biomedical express.

Intravascular photoacoustic (IVPA) imaging is a promising modality for quantitative assessment of lipid-laden atherosclerotic plaques. Yet, longitudinal IVPA imaging of plaque in the same animal is not yet demonstrated. Here, using a IVUS/PA catheter of 0.9 mm in diameter, we performed IVPA imaging in the aorta of a well-established rabbit model mimicking atherosclerosis in human patients. Previous lipid studies that aimed to detect lipids in plaques in animals have lacked models with advanced atherosclerosis and IVPA devices that could damage the vessel and survival, limiting the chance for to be imaged ex vivo for comparison with the in vivo imaging results Herein, we present an advanced IVUS/IVPA imaging system and method, applied imaged with the in-vivo IVPA imaging and the result were compared and confirmed by the MRI in-vivo experiments and histology. These achievements provide us with a way to understand the new details of atherosclerotic plaques at high resolution and demonstrates the potential of IVPA translation to clinical imaging to detect vulnerable plaques at high risk for thrombosis.

Introduction

Atherosclerotic cardiovascular disease is the leading cause of mortality in the United States, causing nearly one million deaths every year[2, 37]. Cardiovascular disease deaths are most often triggered by the rupture of vulnerable atherosclerosis plaques and subsequent thrombosis[38]. Early identification of vulnerable plaques in vivo, by characterization of morphological and compositional features of the plaque, can have a positive impact on guiding the treatment[4, 39]. In human, atherosclerosis is initiated by the sub-endothelial infiltration of plasma LDL cholesterol and cholesteryl ester, which is enhanced by endothelial damage and further promotes inflammation over decades, together leading to the plaque instability[3, 40-41]. The size and location(s) of the lipid pool and the thickness of the fibrous cap are two features that can be used to determine the plaque stability[42-43].

To reliably and accurately diagnose the pathological stage of atherosclerosis, both the morphological and chemical information of the plaque are required. MRI is a widely used imaging method which can characterize major components of plaque, including the fibrous cap, the lipid core hemorrhage and inflammation[44-45]. Although non-invasive, MRI is limited by the centimeter-scale spatial resolution. Several catheter-based invasive methods including Intravascular ultrasound (IVUS)[46-47] and optical coherent tomography (OCT)[48] were developed to obtain high resolution morphological information and locations of the plaques, yet lacking information about the plaque chemical composition. IVUS was recently combined with near-infrared spectroscopy (NIRS), which provides

information about the lipid content in a plaque[49]. However, NIRS cannot precisely locate the plaque and determine the volume of the lipid core.

Catheter-based intravascular photoacoustic (IVPA) imaging is a promising technology for localization, characterization, and quantification of coronary atherosclerotic plaque lipids. IVPA imaging is based on molecular absorption of a nanosecond laser pulse in the tissue and subsequent generation of an ultrasound signal detected by a transducer; the method is capable of mapping the composition of the artery wall with an adequate imaging depth. Catheter-based IVPA imaging is minimally invasive, provides high resolution imaging of the arterial wall, and offers several advantages for imaging atherosclerosis plaques[21, 50-51]. Co-registered with IVUS, the IVPA/US imaging system can achieve real time display of lipid-rich plaques with high sensitivity and sufficient depth, providing size, location, and composition information to identify plaques having high risk of rupture[21, 52].

Photoacoustic imaging of vascular lipids was first demonstrated by the Cheng, Emelianov and Beard groups using a laser wavelength around 1200 nm[52-54]. Since then, there has been a lot of advances in development an IVPA catheter toward intravital imaging of vascular lipids. Specifically, The Ji-Xin Cheng group demonstrated high-sensitivity IVPA imaging through a collinear catheter design[55] and a portable IVPA-US system capable of imaging at up to 25 frames per second in real-time display mode[29]. The Cheng group also demonstrated in vivo IVPA imaging of lipid distribution in rabbit aorta under clinically relevant conditions[27], and more recently, a dual-transducer catheter for high-resolution IVUS and high-sensitivity IVPA imaging[56]. The Gijs Van Soest group

demonstrated intravascular photoacoustic imaging of human coronary atherosclerotic plaque ex-vivo[57], real-time volumetric lipid imaging in vivo at speed of 20 frames per second[26], and Lipid detection in a human atherosclerotic lesion at 1.7 μm with a lower pulse energy than that at 1.2 μm[58]. The Qifa Zhou and Zhongping Chen groups demonstrated high resolution IVPA by using transducer working frequency as high as 80 MHz[59]. The Stanislav Emelianov group demonstrated intravascular photoacoustic imaging of lipid in atherosclerotic plaques in the presence of luminal blood[53]. The same group also built a complete IVUS/IVPA imaging system capable of real-time IVUS/IVPA imaging, with online data acquisition, image processing, and display of both IVUS and IVPA images[60]. The Liang Song group demonstrated optical-resolution IVPA imaging offering optical-diffraction limited transverse resolution as fine as 19.6 μm[30]. The Song group also improved an IVPA/IVUS system with the imaging speed as high as 100 f/s based on a miniature catheter of 0.9 mm [61]. The Shihe Yang group developed a tapered fiber-based IVPA catheter for high-resolution imaging of lipid-rich plaque. Despite these advances, to our knowledge, longitudinal IVPA imaging on the same plaque in the same animal with atherosclerosis has not been conducted. Without such capability, the potential of using IVPA imaging to monitor plaque progression under different diets or drug treatment cannot be fully appreciated.

Here, we demonstrate longitudinal IVPA imaging of atherosclerotic plaques using a rabbit model. The lipid-fed New Zealand White (NZW) rabbits is an animal model to study atherosclerosis and sudden thrombosis in a controlled manner[62]. These rabbits develop foam-cell-rich (fatty steaks) plaques when short term high-fat diets were the only

stimulus used to induce atherosclerosis. Intermittent cycles of fat feeding with periods of normal diet induces plaques at more advanced stages that resembles human atheroma. Moreover, with the combination of arterial wall balloon injury and hyperlipidemia, advanced lesions formed in shorter periods compared to the cholesterol-fed swine models.

There are a few challenges facing the study of thrombotic events and plaque vulnerability in live animals., including controlled induction and timed of the thrombosis. The rabbit model of controlled atherothrombosis combine cholesterol feeding with early arterial wall injury, produces aortic plaques that mimic 4 of the 6 American Heart Association stages found in humans, including advanced highly inflammatory rupture-prone lesions in a short term (2-3 months). The most unique and valuable contribution to atherosclerosis research is that vulnerable and stable plaques can be differentiated by a timed pharmacological injection ("triggering") that is coordinated with vascular imaging to detect thrombus formation, which is non-fatal.

Using this rabbit model, a recent MRI study atherosclerosis monitor plaque progression preceding stimulated plaque rupture with serial analysis in the same animal[63]. Each aorta typically has several plaques, each of which can be monitored over time, and the stable and vulnerable plaques differentiated at the end of the 3-month protocol by triggering. These unique features render this rabbit model an ideal testbed for survival in-vivo IVPA imaging.

Technically our team made a few advances that enabled in vivo longitudinal IVPA imaging on the same artery in the same animal. First, we identified a proper protective

sheath material that is transparent to both PA and US signals is essential for in vivo application[27]. Second, we minimized the catheter diameter to 0.9 mm. Third, we established a professional surgical procedure that minimized the damage to animal. Fourth, we applied MRI to accurately locate the plaque in the aorta. With these efforts, we successfully conducted longitudinal in vivo IVPA imaging on same rabbits with survival surgeries. This advancement provides us with a new platform towards a deeper understanding of the atherosclerosis and an accurate way of evaluating the effectiveness of a treatment.

Methods

Rabbits Model

Rabbits have served as models of atherosclerosis for more than a century[1]. The New Zealand White (NZW) rabbit presents a highly valuable model for atherosclerosis which does not require any genetic modification. And the size of its aorta is similar to human coronary artery. In our experiment, two 1-month male NZW was chosen as the test group and one 1-month male NZW was chosen as control group.

A 3-month protocol was developed by the Hamilton lab. The NZW was fed with 1% cholesterol diet for 2 weeks followed by balloon injury and then 6 weeks of cholesterol diet and 4 weeks of normal chow[2]. The balloon injury of the abdominal aortic wall was performed using a 3F Fogarty catheter introduced through a right femoral artery cut down under general anesthesia. After the catheter was advanced to the diaphragm, the balloon was inflated and the catheter was gently retracted toward the iliofemoral artery.

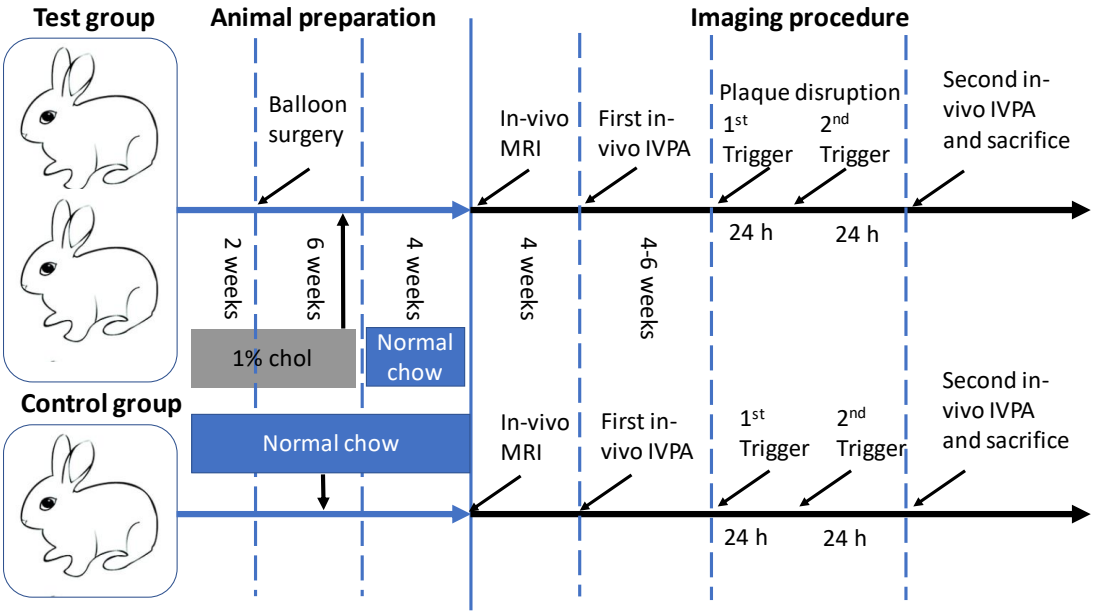

Figure 3.1 Timelines for the CHOL-fed rabbits with or without injury.

The frst timeline shown includes 2 months of 1% CHOL feeding followed by 1 month of normal diet. The second timeline adds endothelial injury carried out in the 1% CHOL+injury rabbit groups at 2 weeks. MRI in vivo was carried out at 2 months, followed by two repeat MRI sessions at 3 months to assess plaque rupture by pharmacologic triggering

In vivo MRI

The In-vivo MRI imaging was done after 10 weeks of the balloon surgery. The in vivo MRI experiments were performed on NZW under deep sedation using a 3.0-T Philips Intera Scanner (Philips Medical Systems, Ohio). Ungated coronal 3D phase contrast MR angiograms (PC-MRA) acquired with a T1-weighted, fast-filed echo sequence were used as scout images. Two-dimensional, T1-weighted, black-blood (T1BB) axial images were then acquired with a double-inversion recovery turbo-spin echo sequence and cardiac gating. Subsequently, ungated axial 3D PC-MRA images were

acquired immediately after a bolus injection of Gd-DTPA (0.1 mmol/kg IV) (Magnevist, Germany). Finally, post-contrast-enhanced (post-CE) T1BB images were acquired 10 to 15 minutes after Gd-DTPA injection with parameters identical to those used for the non-contrast-enhanced T1BB images.

Plaque disruption was pharmacologically triggered with intraperitoneal injection of Russell's viper venom (0.15 mg/kg; Enzyme Research, South Bend, IN) followed 30 later by intravenous injection of histamine (0.02 mg/kg; Sigma-Aldrich, St. Louis, MO). This procedure was performed twice within 48 h on two consecutive days. Russell's viper venom is a procoagulant factor and endothelial toxin, and histamine acts as a vasopressor in rabbits. Heparin (1000 USP units; Sigma-Aldrich) was administered intravenously prior to euthanasia to prevent postmortem blood clotting.

In-vivo IVPA

The first in-vivo IVPA imaging was conducted after 10 weeks and the second 18-20 weeks after the balloon surgery. The sedation will be achieved by Ketamine/Xylazine/Acepromazine: 35 mg/kg / 5mg/kg /0.75 mg/kg IM. Induction of anesthesia will be accomplished by injection of of Acepromazine 0.75 mg/kg IM followed in at least 5 minutes by ketamine 35 mg/kg IM and Xylazine 5 mg/kg IM. A laryngeal mask (LMA) for the rabbit is used gives oxygen.

Following induction of anesthesia, the fur on the right leg and right abdominal region connected to the leg will be cleaned by a clipper. Following shaving of the site, betadine will be applied, followed by alcohol, and this procedure will be repeated for 3 times. A femoral artery cut down will be performed under sterile conditions. Then, a 4F

introducer sheath placement in femoral artery will be carried out before imaging. Through the introducer sheath, the IVPA catheter covered by catheter sheath was advanced to the thoracic aorta. The advance distance is decided by the balloon surgery area and the MRI imaging. 2 fps and 0.2 mm/s were used to do IVPA imaging of the aorta. A total length of 50 mm was recorded by pullback of the catheter. During the surgery, the animal surgeon will place the looser sutures spaced further apart to lessen the number of sutures used and prevent skin irritation.

After the first imaging procedure, the catheter and sheath will then be removed. Hemostasis will be accomplished by direct pressure to the artery following sheath removal and suture closure. The surgical wound will then be sutured closed. During the surgery, respiration, heart rate and SpO2 of the rabbits will be monitored. PDS monofilament sutures will be used to lessen the chance of post-operation irritation. Immediately after the surgery when the animals become conscious a plastic e-collars, will be placed around the neck to prevent chewing of the sutures at the incision site. All these ensure the NZW survival after the imaging procedure.

After final imaging has been recorded, while the rabbit is under anesthesia, the animal will be euthanized by pentobarbital overdose: Pentobarbital overdose (>120 mg/kg IV) Euthanasia will be accomplished by first administering Acepromazine 1 mg/kg IM once. After 15-20 minutes, a small IV will be placed in an ear vein, after which a lethal bolus dose of sodium pentobarbital 120 mg/kg IV will be administered. Cardiac arrest will be confirmed with auscultation using a stethoscope.

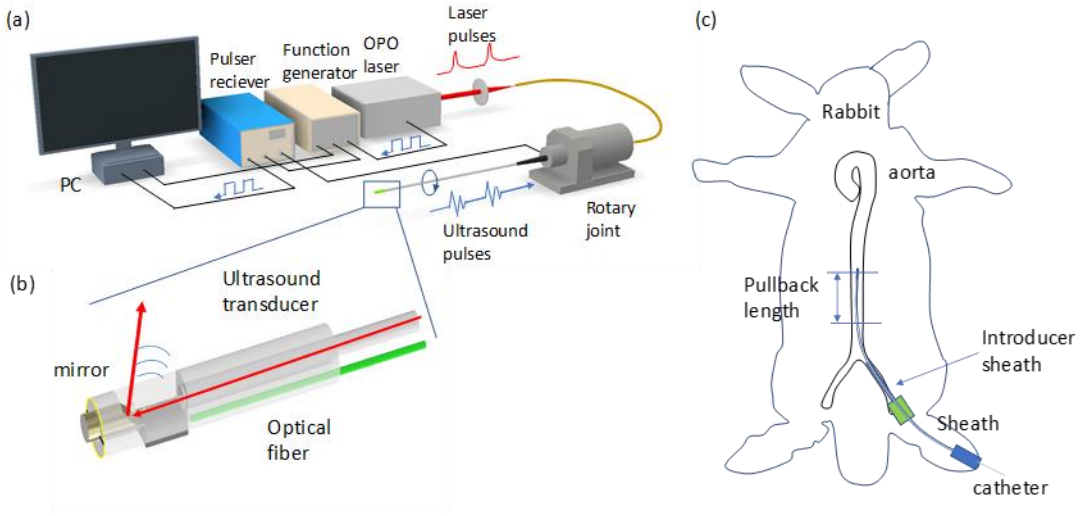

Figure 3.2 IVPA imaging system and the in-vivo surgery.

(a) The IVPA imaging system. Nano second laser pulses are couple to a multimode fiber and directed to the catheter through rotary joint. At the catheter tip, the laser pulse are reflected by a gold coated mirror and shine on the artery. A the same time, the laser will generate an electric trigger signal, send to the function generator. The function generator will produce two triggers, one to the data acquisition card and one to the Pulser reciever, which will generate a delayed ultrasound pulse at the ultrasound transducer. (c) shows the in-vivo rabbit IVPA imaging surgery. A introducer catheter is inserted at the iliac artery and the catheter in sheath is inserted to the aorta.

IVPA System

An IVPA system developed by our group provided dual-modality intravascular photoacoustic and ultrasound imaging at speed up to 16 fps with real-time display[29]. A home built Nd:YAG pumped OPO emitting ~5 ns pulse with 500 Hz repetition rate at a wavelength of 1732 nm served as the excitation laser source. The laser output was coupled to a multimode fiber (FG200LEA). The laser passes through the fiber rotary joint and coupled to the IVPA-US catheter. At the distal end of the fiber in catheter Fig 3.2.b, the laser reflected by a 45° gold coated rod mirror. The generated photoacoustic signal was collected by the ultrasound transducer where ultrasound signal was converted into

electronic signal. Then signal was amplified by the pulse reciever and digitalized by the data acquisition card (ATS9350 PCI express digitizer, AlazarTech). After 4 μs delay, the transducer was excited by an electronic pulse and the reflected ultrasound signal was also collected by the same ultrasound transducer, amplified and digitalized. The synchronization and delay was controlled by the function generator (9512+, Quantum Composer). All these recorded data were then processed by a LabVIEW program and display in real time.

Results

In vivo MRI measurements

From in vivo MRI measurements, we assessed vessel wall area (VWA) and plaque gadolinium (Gd) contrast enhancement. Selected segments representing regions with and without plaque and normal vessel areas were compared. Atherosclerosis was observed in the test group rabbits and no atherosclerosis was observed in control rabbit. Figure 3.3 shows representative MRI images of the aorta with plaque and the control group aorta. From the in-vivo MRI image, the test group's plaque area, vessel area, and remodeling ratio were significantly larger than the control group.

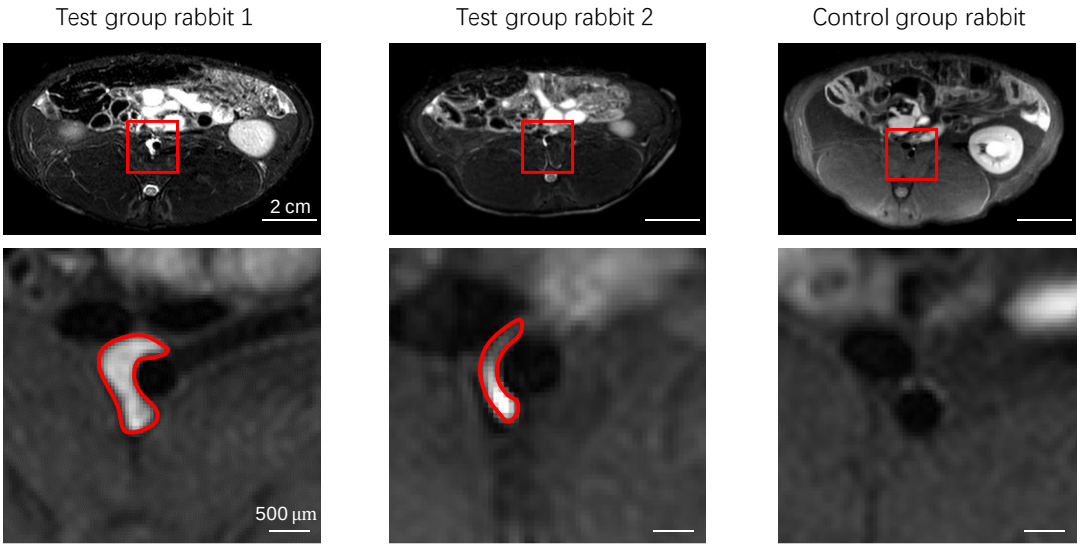

Figure 3.3 In-vivo MRI image of the rabbit aorta.

T1W MRI images of atherosclerosis plaque withd Gd contrast enhancement in rabbit abdominal aorta taken at 10 weeks after the balloon surgery and the control group. The d,e,f are the corresponding enlarged view of the aorta.

In vivo IVPA Imaging

The serial in-vivo IVPA imaging of the NZW was conducted and we recorded in vivo IVPA/US images of the aorta with 50 mm. Figure 3.4 a-f shows representative cross-sectional PA images, q-l shows merged PA/US images. The PA images show the presence of lipid within the aorta wall which indicate the presence of the plaque. The US images provide important morphological information about the artery. From the figure we can see that the test group rabbit has PA signal and the thickness of the artery wall is much larger than the control group. In the control group, no obvious PA signal has been found.

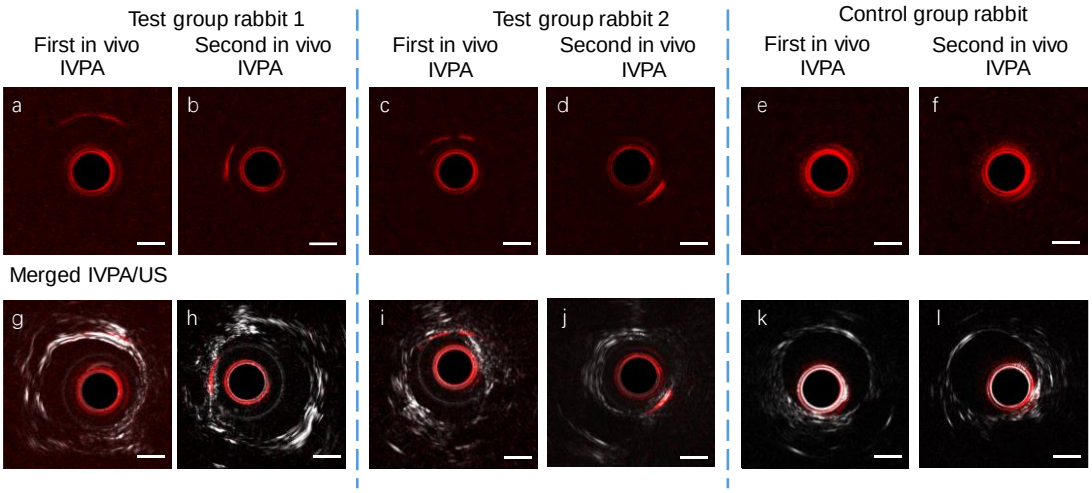

Figure 3.4. In vivo IVPA imaging of the rabbit aorta.

(a-f) Intravascular PA images. a,c,e are the IVPA image of the first imaging procedure and b,d,f belongs to the second in-vivo imaging. (q-l) Combined PA and US images corresponding to the upper row. The scale bar is 1 mm.

Histology of the Rabbit Aorta

After the euthanasia, the aorta was harvested. All the aortas were fixed in 10% formalin for approximately 30 minutes to maintain lumen as close to in vivo morphology as possible. The aorta section that were shown to have plaque were selected and cut in 3 mm segment. Then it was paraffin embedded, sectioned and stained with Oil Red O and H&E. The Oil Red O is a fat soluble dye that stains neutral triglycerides and lipids while the H&E stain provides a comprehensive picture of the microanatomy of organs and tissues. With the histology, the existence of the plaque and the thicken of the aorta is further confirmed (see Figure 3.5).

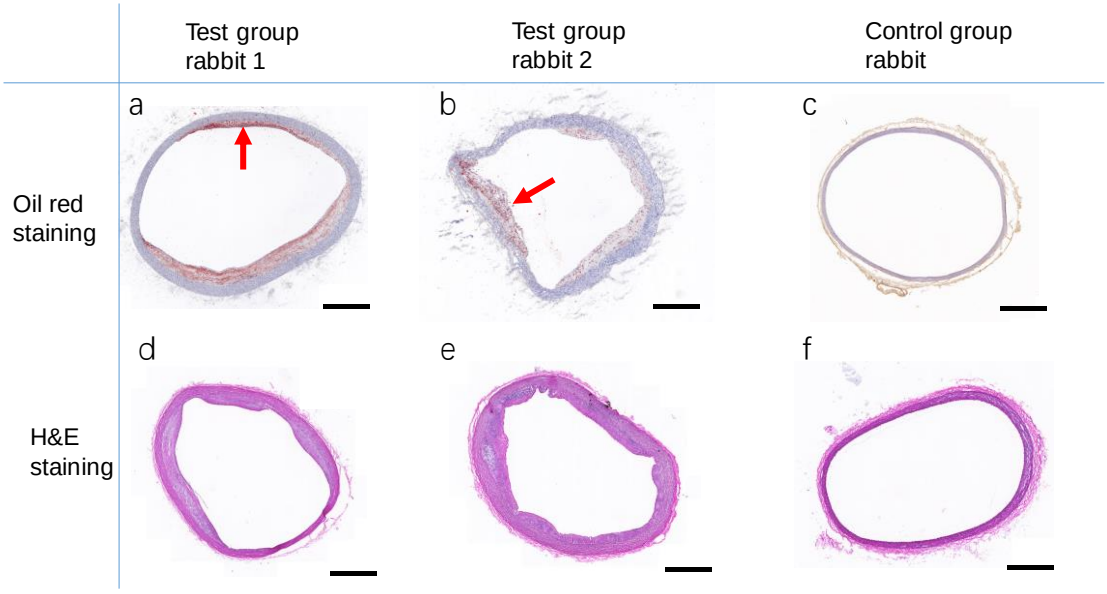

Figure 3.5 The histology of the rabbit aorta.

The rabbit aorta was cut to slices and stained with Oil red and H&E staining. Scale bar 1 mm.

CHAPTER FOUR – VIBRATIONAL SPECTROSCOPIC DETECTION OF A SINGLE VIRUS BY MID-INFARED PHOTOTHERMAL MICROSCOPY

The work in this chapter was published in analytical chemistry. Reprinted with permission form the American Chemical Society publishing group. (Copyright 2021 Optical Society Publishing Group)

We report a confocal interferometric mid-infrared photothermal (MIP) microscope for ultra-sensitive and spatially resolved chemical imaging of individual viruses. The interferometric scattering principle is applied to detect the very weak photothermal signal induced by infrared absorption of chemical bonds. Spectroscopic MIP detection of single vesicular stomatitis viruses (VSVs) and poxviruses is demonstrated. The single virus spectra show high consistency within the same virus type. The dominant spectral peaks are contributed by the amide I and amide II vibrations attributed to the viral proteins. The ratio of these two peaks is significantly different between VSVs and poxviruses, highlighting the potential of using interferometric MIP microscopy for label-free differentiation of viral particles. This all-optical chemical imaging method opens a new way for spectroscopic detection of biological nanoparticles in a label-free manner and may facilitate in predicting and controlling the outbreaks of emerging virus strains.

Introduction

Viruses represent both a vexing public health problem and an increasingly common source of therapeutics and vaccines. Viruses are responsible for numerous epidemic outbreaks, including the 1918 influenza pandemic[64], Zika[65], Ebola[66], and the ongoing COVID-19[66]. Attenuated viruses are the basis for more than a dozen vaccines[67]. Genetically engineered viruses are approved for gene therapy[68], direct oncolytic cancer therapy[69], and CAR-T cell treatments[70]. The critical unit in both harmful and helpful virus functions is the virion, an extensively loaded nanoscale particle that shields and then delivers the infectious viral unit into susceptible cells. The make-up and function of individual virions is an evolving area of study, benefitting from powerful techniques such as electron microscopy, atomic force microscopy[71], reflectance imaging microscopy[72], and structured illumination microscopy using fluorescently tagged virions[73]. Each of these approaches has advantages, but none to date have shown the ability to directly probe the chemical content or signature of an individual virion on a single particle scale

Interferometric biosensing and microscopy have been extensively studied for sensitive, high-resolution, and ultrafast nanoscale specimen studies[74-77]. The interferometric imaging enhances the weakly scattered light from a nanoparticle of interest via interference with a stronger reference field that brings the scattered signal into the shot-noise limit of the imaging system, which otherwise falls short of the detector noise in dark-field detection as a consequence of a drastic signal drop[78-80]. In wide-field modality using a layered substrate, an interferometric reflectance imaging sensor has

been demonstrated to detect viruses[81] and exosomes[82] without labels as well as single protein[83] and nucleic acid[84] molecules by labeling with plasmonic nanoparticles. Interferometric microscopy pushes the sensitivity beyond the bright-field optical microscopy down to a single protein in both widefield[85-86] and confocal scanning modes[87-88] using a glass substrate. To date, interferometric studies of biological nanoparticles have been limited to affinity-specific molecular information, whereas the chemical composition of particles has remained inaccessible.

To obtain molecular information beyond the surface affinity, vibrational spectroscopy based on either Raman scattering or infrared absorption is commonly employed in biological studies. These methods identify the chemical content of a substance based on molecular vibrational fingerprints. For Raman scattering, the cross section is extremely small approximately 1 out of 10^{10} incident photons are emitted through Raman scattering. Surface-enhanced Raman scattering (SERS) has shown great potential for single molecule detection at a plasmatic hot spot[89-92]. The detection reliability of SERS, however, relies on the quality of the substrate. Besides, because the hot spot (<10 nm) is smaller than a virus (~100 nm), SERS is not able to probe the entire content of a virus. Tip-enhanced Raman spectroscopy detection of the virus is reported[93], where the reliability strongly depends on the tip quality. Recently developed coherent Raman scattering microscopy allowed high-speed vibrational imaging of cells and tissues[94-95]. However, coherent Raman scattering imaging of a single virus has not been demonstrated partly due to the small cross section of Raman scattering from a nanoscale viral particle.

In comparison to inelastic Raman scattering, infrared absorption has 6−8 orders of magnitude larger cross section[96]. The infrared spectra deliver information on proteins as well as on interactions between protein subunits and nucleic acids[97]. However, spectroscopic detection of a single virus by conventional FTIR is hampered by the intrinsically low spatial resolution on the micron scale[98]. AFM-IR, which offers nanoscale spatial resolution and high detection sensitivity, is capable of providing a single virus infrared spectrum[99]. However, AFM-IR requires sample contact, thus suffering sample damage risk. Thus, a contact-free, easy to operate, and highly sensitive method for single virus detection is desired. Mid-infrared photothermal (MIP) imaging is an emerging technique[7, 13, 100] meeting these requirements. In MIP microscopy, a visible beam is deployed to sense the photothermal effect induced by infrared absorption of molecules, providing sub-micron spatial resolution defined by the visible probe beam. MIP signals can be detected in either scanning mod or wide-field mode. On the excitation side, MIP can be implemented with an IR/visible co-propagating or counter-propagating geometry. In the latter, an objective lens (OL) of a high numerical aperture can be used to focus the visible beam and a spatial resolution of 300 nm has been reached. More recently, researchers at the University of Notre Dame pushed the detection limit to 60 nm polymer particles with a balanced detection scheme[13].

Here, we harness the interferometric scattering principle in confocal configuration to push the sensitivity limit of MIP microscopy to an unprecedented level toward single virus detection. We report, for the first time, vibrational fingerprint spectra

of a single poxvirus and a vesicular stomatitis virus (VSV) recorded with a counter-propagating interferometric MIP microscope.

Methods

Experimental Setup

A schematic is shown in Figure 1. A pulsed mid-IR pump beam, generated by a tunable (from 1000 to 1886 cm−1) quantum cascade laser (QCL, Daylight Solutions, MIRcat-2400) operating at a 100 kHz repetition rate, passes through a calcium fluoride (CaF2) cover glass and then is focused onto the sample through a gold-coating reflective objective (RO) lens (52×; NA, 0.65; Edmund Optics, #66589). A continuous-wave probe laser (Cobolt, Samba 532 nm) beam is focused onto the same spot from the opposite side by a high NA refractive objective (60×; NA, 1.2; water immersion; Olympus, UPlanSApo). The probe beam is aligned to be collinear to the mid-IR pump beam to ensure the overlap of the two foci to achieve a good signal level. A scanning piezo stage (Mad City Labs, Nano-Bio 2200) with a maximum scanning speed of 200 μs/pixel is used to scan the sample. Before the photodiode, a confocal pinhole is placed to pass only the scattered photons from the nanoparticles and the reflected photons from the top surface of the CaF2 glass while blocking the photons reflected from other surfaces. Therefore, the pinhole reduces the unwanted reflections from the optical surfaces in the collection path. We empirically observe a slight improvement in signal to noise ratio (SNR). In the imaging procedure, the nanoparticles spotted on a CaF2 cover glass are

first localized by the backward interferometric signal. The sample stage is adjusted axially to maximize the interferometric contrast. Then, the pulsed infrared pump beam illuminates the sample. The modulated scattering is collected by a photodiode and the MIP signal is extracted by a lock-in amplifier (LIA). Before the RO, the infrared laser passes through a CaF2 coverslip and the reflection of the infrared laser is measured by a mercury cadmium telluride (MCT) detector for normalization of IR power at each wavelength. A laboratorybuilt resonant circuit, with its resonant frequency (103.8 kHz, gain 100) tuned to the repetition rate of the QCL, is used to amplify the photocurrent from the photodiode before it is sent to the LIA (Zurich Instruments, HF2LI) for phase-sensitive detection of the MIP signal.

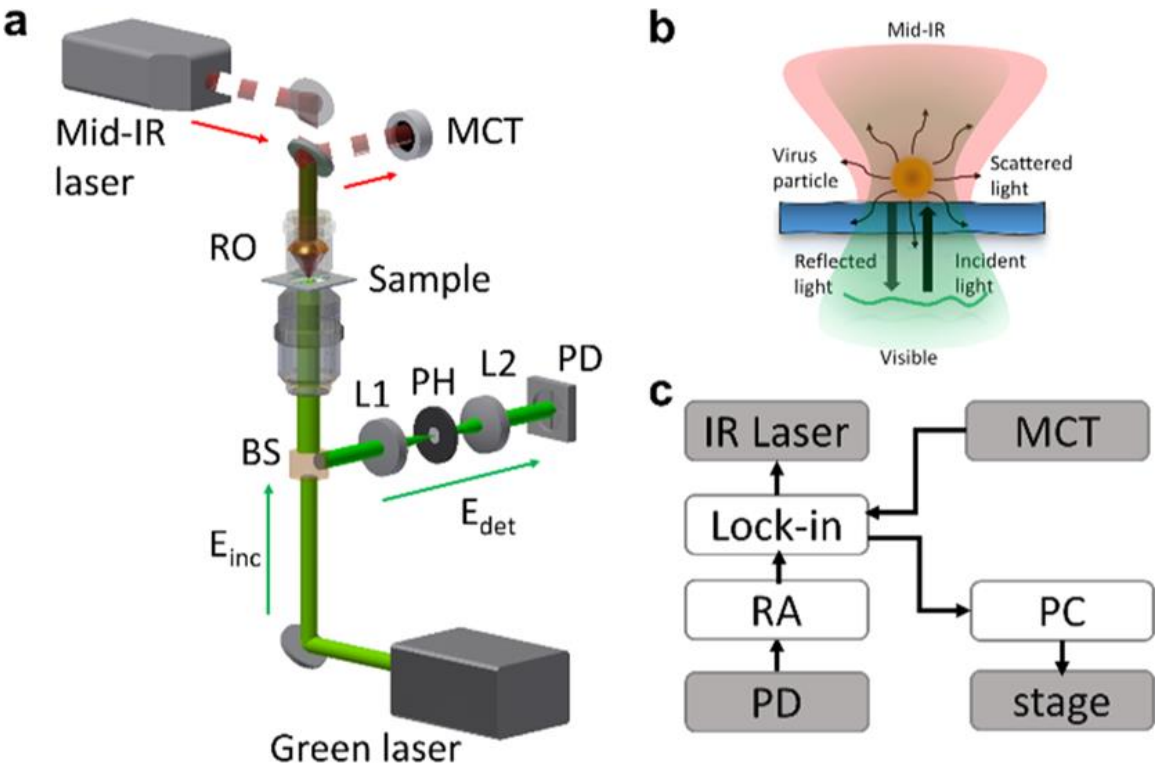

Figure 4.1 Illustration and principles of interferometric MIP microscopy.

(a) Schematic. A pulsed mid-infrared pump beam is provided by a QCL and focused into a sample by a RO. A continuous visible (green) probe beam is focused on the sample by a water immersion OL. To measure the IR power, a small fraction of the IR beam is reflected by a CaF2 glass onto an MCT detector. The interferometric signal (Edet) is collected in an epi-illumination configuration using a beam splitter. A silicon photodiode (PD) detects Edet after filtering by a pinhole (PH) in a confocal configuration. The 4f system consisting of two achromatic doublets L1 and L2 provides access to the confocal conjugate plane for the filtering. (b) Illustration of the counter propagation interferometric scattering detection principle. (c) Electronic connections for system control and signal detection. PD is connected to a resonant amplifier to amplify the detected probe beam. LIA demodulates the PD signal to isolate the photothermal signal. PC controls the motorized scanning stage and data acquisition. The IR intensity detected by the MCT is also received by the LIA for normalization of the photothermal signal by IR power at each wavenumber. The lock-in sends a reference signal to trigger the laser at a 100 kHz frequency.

To normalize the MIP signal by the IR power at each wavenumber, the mid-IR intensity detected at the MCT is sent to another lock-in input channel. A computer is used to synchronize the QCL wavelength tuning, stage scanning, and data acquisition. The photothermal spectra are processed using in-house scripts written on MATLAB. The raw photothermal signal is normalized by the mid-infrared laser power spectrum collected by the MCT detector at a step size of 5 cm^{-1}. For detection of the virus, the photothermal spectra are averaged 5 times to achieve a high SNR.

Principle of Interferometric Photothermal Signal Detection.

Our system's detection mechanism relies on the ultra-sensitive interferometric scattering imaging principle[101] which employs a common-path interferometry. This configuration enables highly sensitive and stable interferometric imaging of nanoparticles captured on the substrate surface. The light impinging on particle scatters and reflects off

the glass/air interface. The complex valued reflected field $\boldsymbol{E_r} = E_r e^{j\phi_r}$ and scattered field $\boldsymbol{E_s} = E_s e^{j\phi_s}$ interfere at the detector: $I_{det} = |\boldsymbol{E_r} + \boldsymbol{E_s}|^2$. This recorded interference signal can be formulated as follows:

$$I_{det} = E_r^2 + E_s^2 + 2E_r E_s \cos(\theta)$$

The first term denotes the reference field intensity $I_r = |E_r|^2$, the second term denotes the scattering intensity $I_s = |E_s|^2$, and the third term denotes the real valued interferometric cross term $2Re\ (\boldsymbol{E_r}\boldsymbol{E_s^*})$. The phase term $\theta = \phi_r - \phi_s$ is the phase difference between the reference and scattered fields. The strength of the scattered field amplitude scales with the sample's polarizability α. In the dipole limit where particle radius *r* is much smaller than illumination wavelength $r \ll \lambda$, the polarizability for a nanosphere[102] is given by:

$$E_s \propto \alpha \ = \ 4\pi\epsilon_m\, r^3 \frac{\epsilon_p - \epsilon_m}{\epsilon_p + 2\epsilon_m}$$

where ϵ_p and ϵ_m respectively denote the dielectric permittivity of particle and the surrounding medium. Considering small nanoparticles, the scattering intensity term which has r6 dependence generates signal levels well below the shot-noise limited detection and quickly vanishes against the reference field intensity. Therefore, the scattering intensity term in eq. 1 becomes negligible due to the sample's weakly scattering nature. The resulting signal constitutes the background signal (Ir) and the interferometric cross term. The interferometric term realizes the linear detection of the weak scattered field with a strong reference field enhancement. Moreover, such detection

allows for the detector to operate at the shot-noise limited performance. After background subtraction, the interferometric signal can be expressed as follows:

$$S = I_{det} - I_r = 2E_s E_r \cos(\theta)$$

The phase difference contains the accumulated Gouy phase, field propagation phase, and the sample's internal field phase. The sinusoidal term modulates the signal contrast depending on the axial position with respect to the objective focus. This term can be optimized to maximize the contrast by defocusing[103].

Based on the interferometric detection of scattered field, the photothermal signal is observed as a result of the molecular absorption by the sample[104-106]. The IR pulse vibrationally excites the molecules inside a sample. This heats the sample depending on the optical absorption cross-section and IR-pulse intensity. The absorption then causes a local temperature rise of ΔT at the particle's vicinity. This photothermal effect induces a subtle change in the particle's refractive index and size due to thermal expansion. As seen from eq. 2, this effect modifies the nanoparticle's polarizability and thus the scattered field amplitude. The induced signal change can be written as:

$$\Delta S = 2E_r \Delta E_s$$

where $\Delta E_s = E_s(T_0 + \Delta T) - E_S(T_0)$ is the difference of the scattered field amplitudes with a pre-IR pulse temperature T_0. We assume here the particle as a uniform heat source which is a valid assumption for very small nanoparticles compared with the micron-scale IR wavelength. Similar to the DC case, the interferometric photothermal imaging realizes linear detection of the change in the scattering amplitude. The photothermal signal can be

measured as the intensity modulation at the detector. One can approximate the modulation depth $\Delta S/S$ by the means of the particle's polarizability change as follows:

$$\frac{\Delta S}{S} \approx \frac{\Delta \alpha}{\alpha} \approx 3\Delta T\left(\alpha_r + \frac{2\,\epsilon_p}{(\epsilon_p + 2\epsilon_m)(\epsilon_p - \epsilon_m)}\alpha_n\right)$$

where $\alpha_r = \frac{1}{r}dr/dT$ and $\alpha_n = \frac{1}{n}dn/dT$ are the thermal expansion and thermo-optic coefficients, respectively. This approximation holds for $\Delta r \ll r$ and $\Delta n \ll n$. The modulation fraction becomes in the orders of 0.01% per 1 K for PMMA beads for given dr/dT = 90×10^{-6} mK^{-1} and dn/dT = –1.1×10^{-4} K^{-1} [107]**.** The lock-in amplifier is utilized to extract this very minute signal.

Virus sample preparation. The recombinant vesicular stomatitis virus expressing green fluorescent protein envelope (rVSV-G-eGFP) was generated as described earlier [108] and the recombinant vaccinia virus expressing Venus fluorescent protein (rVACV-A4L-Venus) was generated as described earlier [109]. To load viruses onto the substrate surface, 100 µL of either VSV or poxvirus stock was incubated on a CaF2 coverslip for 1 hour at room temperature. The rVSV and rVACV concentrations were ~3×10^8 PFU/mL and ~2×10^8 PFU/mL, respectively. Following incubation, coverslips were examined with fluorescence microscopy to ensure that virus was present. All virions were crosslinked and inactivated using 1.0 mL 4% formaldehyde for 1 hour and then dried.

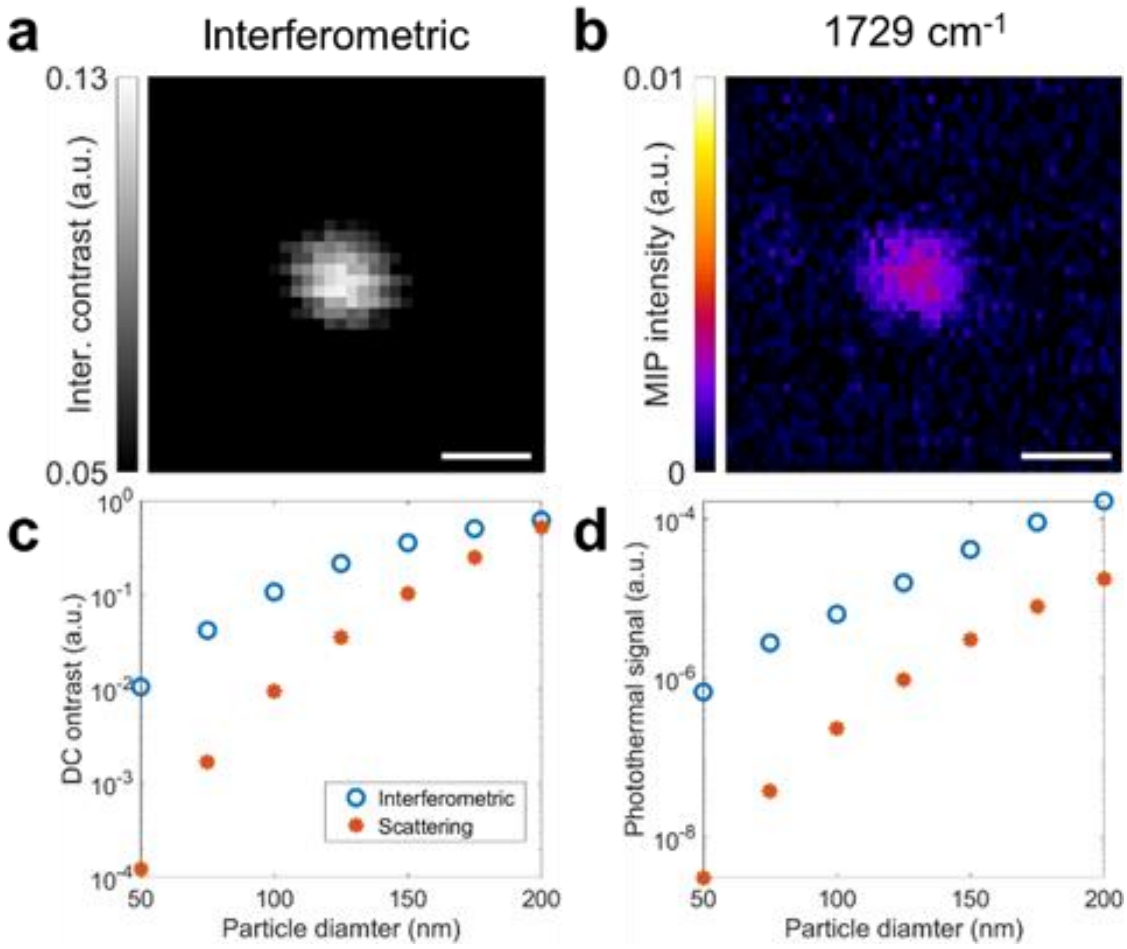

Figure 4.2. Experimental demonstration and theoreti-cal calculations of interferometric detection.

(a) Interferometric scattering image of 100 nm PMMA bead, (b) Interferometric MIP image of the 100 nm PMMA bead at 1729 cm^{-1}. Probe power on the sample: 40 mW; IR pump power on the sample: 8.5 mW. Scale bars: 500 nm; pixel dwell time: 20 ms; image acquisition time: 19.6 s. (c-d) Simulated contrast comparison between interferometric cross term and scattering intensity term for PMMA bead with particle size range from 50 nm to 200 nm in diameter. (d) Photothermal signal calculations corresponds to the signals in c.

Results and Discussion

Experimental detection of 100 nm particles and theoretical calculations

To demonstrate the capability of interferometric photothermal detection, we first image 100 nm poly (methyl methacrylate) (PMMA) beads. These PMMA beads present a suitable model for system characterizations since their size resembles the viral particles in our experiments and importantly PMMA has a dielectric constant (n≈1.5) similar to that of viruses. Figure 4.2a shows a high SNR interferometric scattering image with 0.13 particle contrast. The interferometric contrast is defined as normalized, background-subtracted signal [101]. This indicates that scattering intensity is approximately 400 times smaller than the background (reflected field) intensity. The interferometric detection reveals highly sensitive detection of very weak signals from small particles which may be indistinguishable from the background in the conventional light microscopy. This comes from the fact that residual reflection (~ 4%) from the substrate and particle medium interface. Compared to forward detection schemes where most of the incident light reaches the detector, the reflection geometry in interferometric detection of small particles can improve the contrast by approximately 25 times. We note this is valid in the dipole approximation. Since large particles scatter mostly in the forward direction, we expect to achieve similar contrast levels in both reflection and forward systems.

The nanoscale particles can be modeled in the dipole limit as discussed in the theory section. We perform the theoretical simulations on a custom-developed electromagnetic simulation software on Matlab [110]. This dipole model shows a great agreement with experiments and a more comprehensive electromagnetic model for

particles up to 200 nm [111]**.** We extend this simulation to interferometric imaging configuration. Our simulation can be compartmentalized into two main parts: (1) substrate and particle geometry and dielectric coefficients to define the dipole moment and (2) optical system parameters including objective numerical aperture and illumination function to calculate the point spread functions. Accordingly, we assume the particles are placed on top of a CaF_2 substrate with a height of particle's radius (r). The dipole moment is calculated using polarizability tensor and total driving electric field (E_{inc}). The scattered fields are then calculated using far-field Green's functions. The reflected field is calculated using Fresnel's coefficients considering incidence angle and polarization. Both reflected fields and scattered far fields are mapped into the image space using angular spectrum representation integral. Then, we coherently sum the fields using Eq. 1. Accordingly, we calculate the field contributions in the detected signals for a size range from 50 to 200 nm. Figure 4.2c compares the magnitude of interferometric cross term and scattering intensity terms defined in Eq. 1. The theoretical interferometric contrast for 100 nm PMMA bead is 0.11 which shows an agreement with the experimental value. The incident field amplitude remains constant in all cases. As shown in Figure 4.2c, the interferometric signal becomes more dominant compared to scattering intensity as the particle size decreases. This comes from the fact that the interferometric detection has r^3 dependency compared with the r^6 dependency of the scattering intensity. Therefore, the scattering intensity only detection schemes for nanoscale particles drastically drops below the detector's shot noise limit.

We next characterize the MIP image of the 100 nm PMMA bead as shown in Figure 4.2b. The MIP signal has ~13 SNR which is close to the sensitivity limit of our system. The modulation depth is 0.012 %, indicating that photothermal induced temperature increase in the bead is around 1 to 2 K. Such temperature change is significantly lower than the previously reported studies using optical parametric oscillator laser[112] which has shorter pulse width and relatively larger pulse energy. The temperature rise and decay time for sub-200 nm particles are on the order of the tens of nanoseconds which is much shorter than the QCL laser pulse width (1 μs). Therefore, a lower temperature change is expected in our experiments. To improve sensitivity, one can employ short pulse laser sources with high pulse energy. We further simulate the photothermal signal corresponding to the interferometric scattering contrasts in Figure 4.2c. In the calculations, we update the particle size and refractive index by assuming a 1 K temperature rise. Figure 4.2d shows the absolute value of the signal change induced by the photothermal effect. The results indicate that interferometric detection generates ~25 times more signal for a 100 nm PMMA bead. Thus, interferometric detection of the photothermal effect has a significant advantage over the scattered intensity only detection.

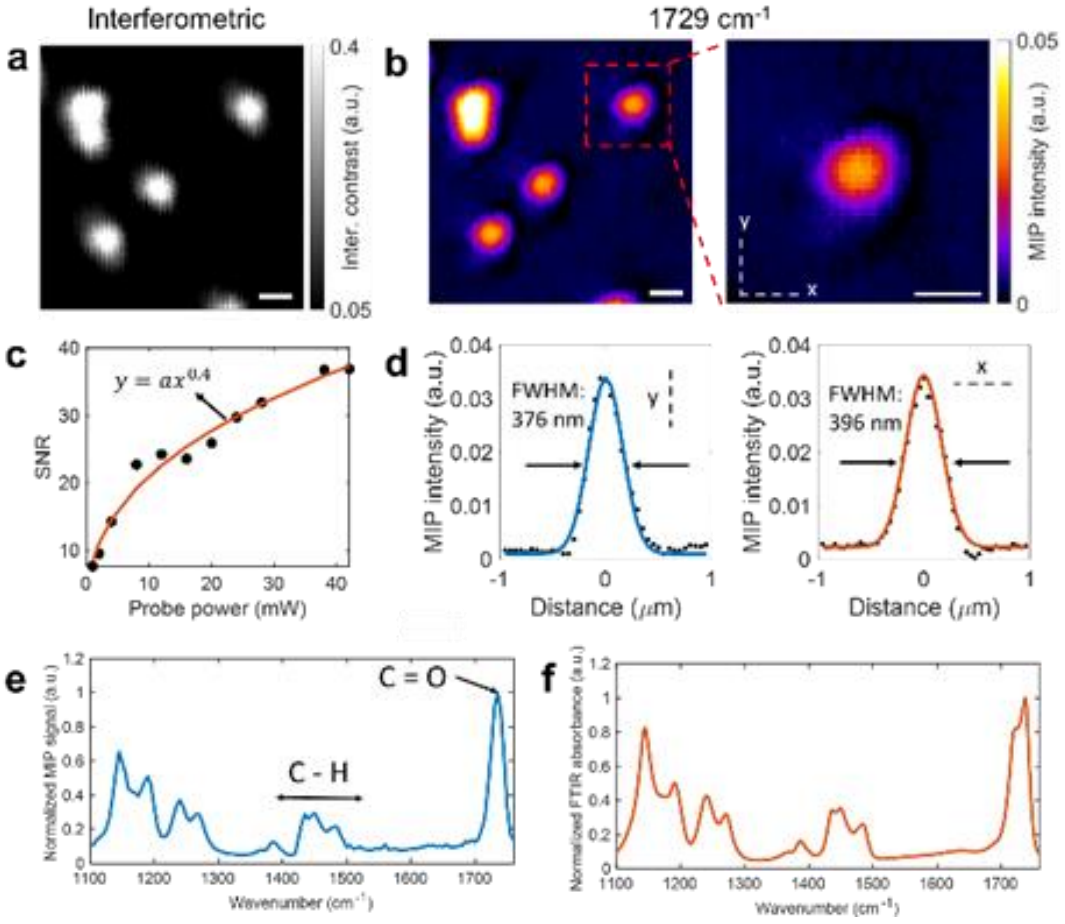

Figure 4.3 Performance of interferometric MIP microscopy.

(a) Interferometric scattering image of 200 nm PMMA beads, (b) (Left) MIP image in **a** and (Right) zoom-in region of a single PMMA bead. Probe power on the sample: 30 mW; IR pump power on the sample: 5 mW at 1729 cm^{-1}. Scale bars: 500 nm; pixel dwell time: 20 ms; image acquisition time: 127 s. (c) SNR characterization of MIP signal showing that shot-noise limit is reached. (d) (Left) Vertical and (Right) horizontal cross-section profiles across the enlarged single bead in **b.** The Gaussian fitted full width at half maximums (FWHM) are respectively 376 nm and 396 nm. (e) MIP spectrum obtained from a single PMMA bead and (f) FTIR acquired from a PMMA film. MIP acquisition time: 10 ms per wavenumber.

Sensitivity, resolution, and spectral fidelity

We then evaluate the sensitivity and resolution of the MIP system by measuring 200 nm diameter since they generate a higher SNR signal compared to 100 nm beads. This is particularly important for spectral characterization to capture low absorption bonds with high data fidelity. Figure 3a shows an interferometric scattering image of PMMA beads. We employ confocal detection to minimize the unwanted reflection from the other surfaces in the optical path. This improves the SNR by suppressing the noise from other sources contributing to the shot-noise. To obtain high quality images, we extended the dwell time of each pixel to 20 ms and applied a small pixel step size of 50 nm. With these improvements, we obtain an SNR of 96 in Figure 3b. The MIP images are taken by tuning the IR laser to 1730 cm^{-1} which is the resonance peak corresponds to acrylate carboxyl (C=O stretching) group absorption in PMMA. To evaluate the spatial resolution of the MIP signal, we measured the intensity profile across the single bead in Figure 4.3b. The measured full width at half maximum (FWHM) along the vertical and horizontal axes are 376 nm and 396 nm, respectively. The slight deviation along the x and y axes could be attributed to the scanning stage's mechanical stability. After deconvolution by particle diameter, we obtain a spatial resolution of 319 nm. This value is consistent with the previous studies using the same counter-beam geometry[113]. Furthermore, we characterize the system's shot noise performance by acquiring MIP images at varying probe powers. The exponential fit coefficient is 0.4 which is close to the theoretical value of 0.5. We then measure single particle spectra spanning from 1100 cm^{-1} to 1750 cm^{-1} (Figure 4.3e). Both resonance peaks of C=O and C-H stretching bonds show the

distinguished spectral signature in the MIP system. The spectral fidelity is confirmed by comparing the MIP spectral profile to the reference spectrum of PMMA collected by an FTIR spectrometer (Figure 4.3f).

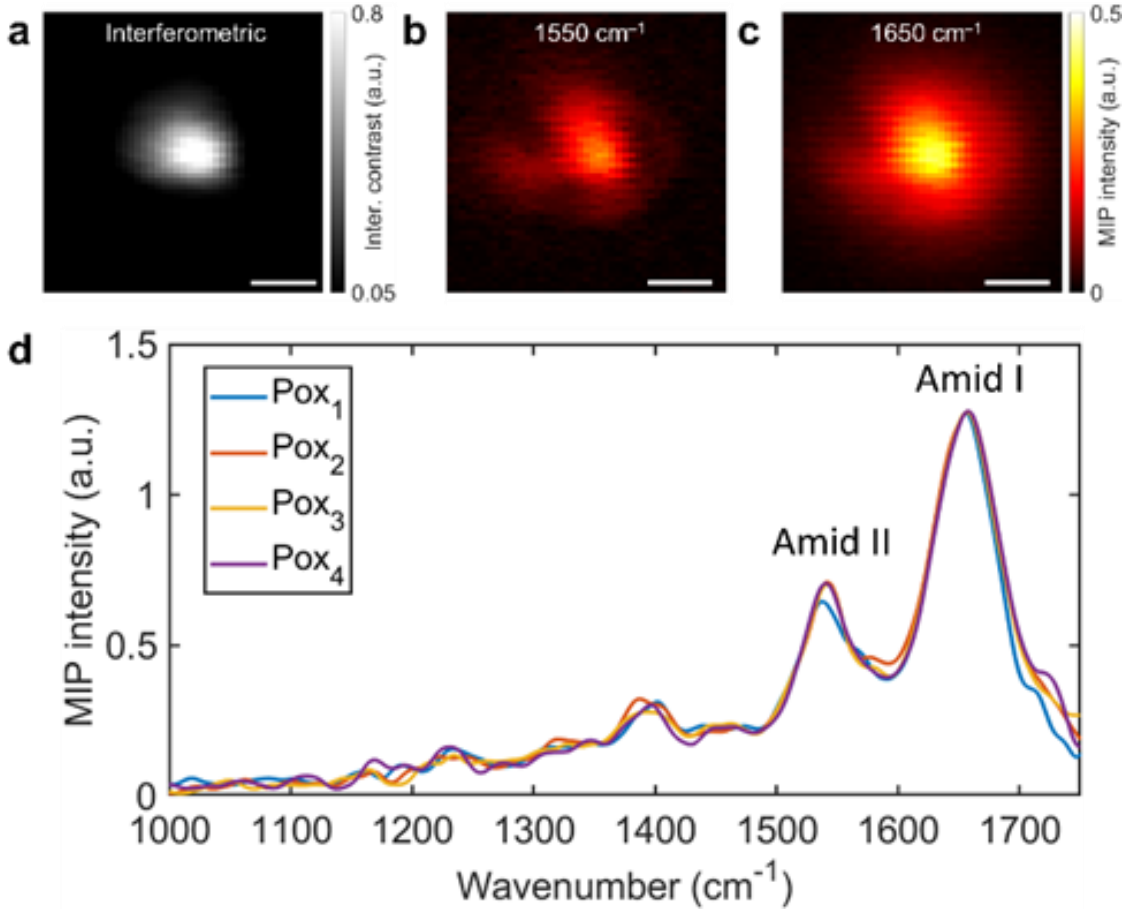

Figure 4.4 Interferometric MIP imaging and spectroscopy of single poxviruses.

(a) Interferometric scattering image of a poxvirus. Probe power on the sample: 30 mW. (b) MIP image of the same poxvirus at the 1550 cm^{-1}. IR pump power on the sample: 18 mW. (c) MIP image of the same virus at the 1650 cm^{-1}. IR power: 20 mW; Scale bars: 500 nm; pixel dwell time: 20 ms; image acquisition time: 46.4 s. (d) MIP spectra of four randomly chosen poxviruses.

Fingerprinting individual viruses

Based on the above characterization, we explore the potential of MIP microscopy for single virus detection. We first demonstrate our system's capability on poxviruses. Poxvirus belongs to a family of double stranded DNA viruses[114]. They are brick-shaped (240 nm by 300 nm) with a well-packed internal structure. Since the lateral resolution of the imaging system is insufficient to resolve the shape and morphology of the virus, the viruses appear as diffraction-limited spots. Figure 4.4a shows the interferometric scattering image of a poxvirus, where the scattering from the poxvirus is accompanied by a large background contributed by reflected photons. Importantly, the interference between the reflected and scattered light enhances virus contrast which becomes detectable in the shot-noise-limited regime. Figure 4.4b and Figure 4.4c shows the MIP image of the same virus in Figure 4.4a, with the IR laser tuned to 1650 cm^{-1} for the amide I band and 1550 cm^{-1} for the amide II band of viral proteins. Both images show high contrast because the background is removed through lock-in detection. In the interferometric scattering image of the poxvirus, the scattered photons after interference with the reflected photons generated a 0.47 V signal on the photodiode and the background gave around a 0.87 V signal. Thus, we achieved around 80 % contrast in the interferometric image, which allowed us to detect the virus particle. For the MIP signal, according to the input range, output signal level, and internal amplification factor from the lock-in amplifier, the modulation depth is calculated to be around 0.1 %. Such changes can be readily extracted by a lock-in amplifier, which allows background-free chemical imaging of the virus. We then took MIP spectra in the fingerprint window (1000 to 1750 cm^{-1}). This procedure is

repeated on four randomly chosen poxvirus. The spectra demonstrate high consistency, as shown in Figure 4.4d. We observe two dominated bands contributed by amide I and amide II vibrations, but a negligible signal from the phosphate vibration at 1080 cm^{-1}. The virus has a well-organized structure in which a protein shell covers the DNA inside. It is possible that vibrational absorption of DNA might not cause sufficient change in size or refractive index for MIP detection.

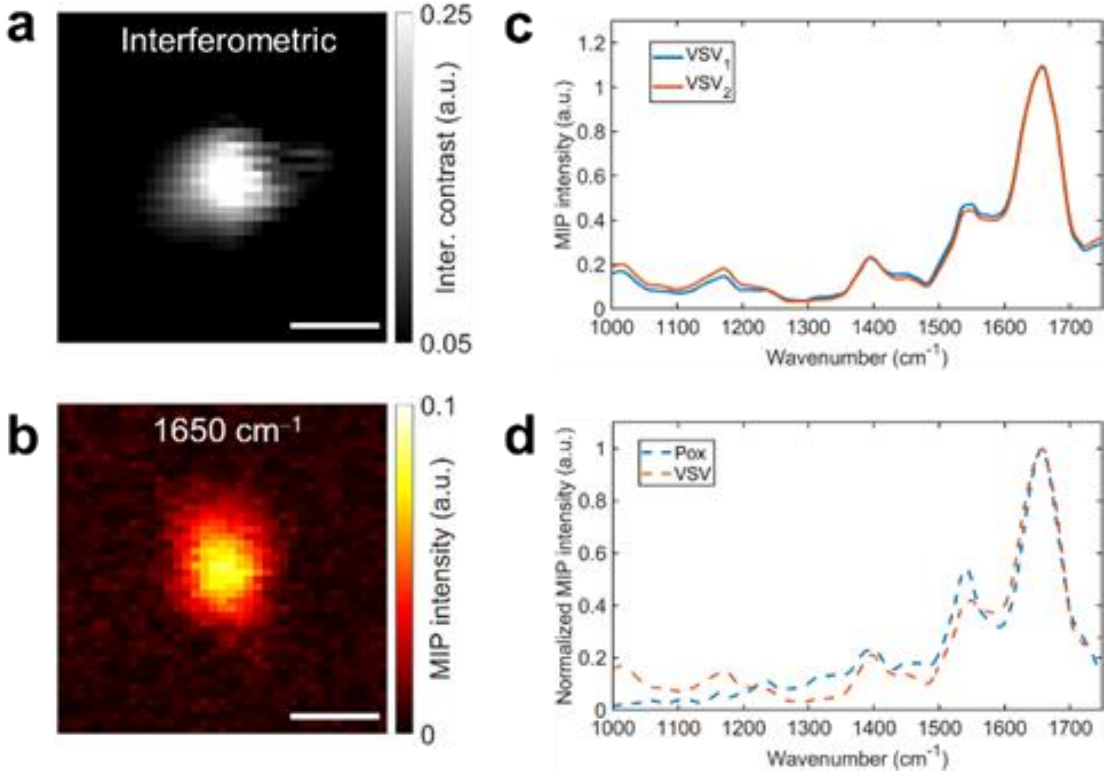

Figure 4.5 Interferometric MIP imaging and spectroscopy of a single VSV.

(a) Interferometric scattering image of a single VSV and MIP signal with the IR laser tuned to 1650 cm^{-1} (Amide I bond). Probe power on the sample: 30 mW; IR pump power on the sample: 20 mW. Scale bars: 500 nm; pixel dwell time: 20 ms; image acquisition time: 34 s. (c) MIP spectra of two VSV particles. (d) Each plot represents the averaged spectra of individual viruses in Figures 4d and 5c. To emphasize the spectral differences, each spectrum is normalized by the maximum MIP intensity at the amid I band.

Next, to test whether our technology can distinguish different virus types, we perform MIP detection of VSV. Figure 4.5a shows the interferometric scattering image of VSV. To obtain the MIP signal shown in Figure 4.5b, the IR laser is tuned to 1650 cm^{-1} (Amide I band). A high SNR of 35 is obtained in the MIP image. Then, we acquire MIP spectra from the two randomly chosen individual viruses. As shown in Figure 4.5c, the spectral profiles are highly consistent in both viruses. More importantly, we observe significant spectrum differences between poxvirus and VSV. The amide I and amide II peaks are the major feature of the virus MIP spectrum. The amide I to amide II intensity ratio for poxvirus is found to be 0.51 and the ratio for the VSV is 0.42. Also, the gap between the amide I and amide II peaks are less obvious for VSV. Figure 4.5d further emphasizes the spectrum differences by comparing them side by side. These spectroscopic features are likely a reflection of the unit structure and molecular content of each virus and can be used to differentiate various types of viruses. As an indirect spectroscopic technique, SERS reporters have been successfully demonstrated in triplex assays for Ebola, malaria, and Lassa in which each specific reporter has distinguished Raman spectrum[115]. Here, our findings suggest that a direct multiplex virus detection is possible towards translational diagnostics. These spectroscopic features are likely a reflection of the unit structure and molecular content of each virus and can be used to differentiate various types of viruses.

To verify our observation of single VSV particles, we performed topography imaging with an atomic force microscope (Multimode AFM with a NanoScope V controller, Bruker Nano). The images were collected in PeakForce Tapping mode. As

shown in Figure 4.6a, rod-like VSV particles shows monodisperse distribution over the substrate surface. From a zoom-in image of a single VSV (Figure 4.6b), we can estimate its size to be 180 × 80 nm, which is consistent with reported VSV sizes[116]. Furthermore, we note the interferometric contrast levels for both VSV and poxvirus show agreement with those observed in the earlier interferometric virus detection study by Connor and Unlu's group[117]

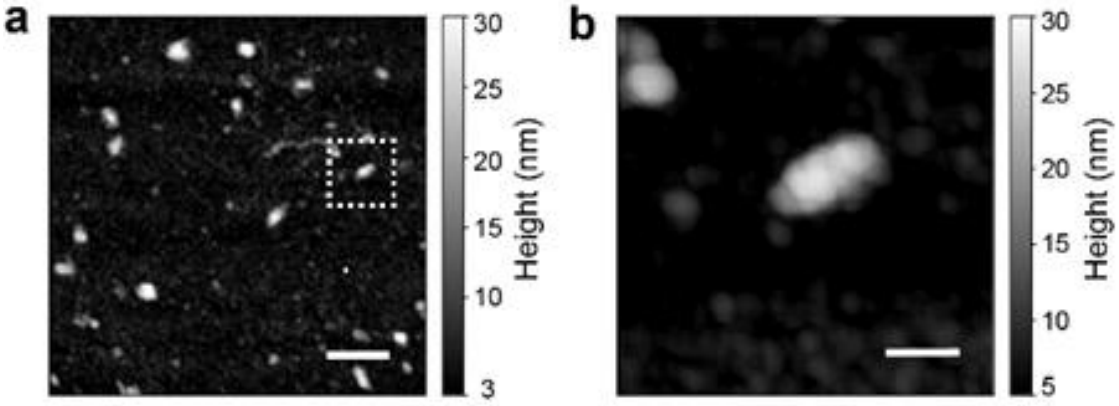

Figure 4.6. AFM topography images of VSV particles.

(a) AFM topography of VSV particles in a 3×3 μm are on a silicon chip. Scale bar is 500 nm. (b) AFM topography of a single VSV. The image is a zoomed-in view of the area marked by a white-dashed-line box in (a). Scale bar is 100 nm.

Conclusion

We have reported a counter-propagating interferometric mid-infrared photothermal imaging system and its application to label-free spectroscopic imaging of a single virus. We harnessed the principle of interferometric scattering to probe the weak signal from a viral particle. Using this approach, we have recorded the fingerprint IR spectra from single poxvirus and vesicular stomatitis virus. The dominant peaks are contributed by the

amide I and amide II groups and the peak ratio allows differentiation of the two groups of viruses. Unlike SERS, our approach does not need plasmonic enhancement on a nanostructure substrate. Collectively, interferometric mid-infrared photothermal microscopy as a pump-probe technique opens opportunities for label-free spectroscopic detection of a broad size range of individual viruses and biological nanoparticles.

CHAPTER FIVE – FLUORESCENCE DETECTED MID-INFRARED PHOTOTHERMAL MICROSCOPE

The work in this chapter was published in analytical chemistry[118]. Reprinted with permission form the American Chemical Society publishing group. (Copyright 2021 Optical Society Publishing Group)

Mid-infrared photothermal microscopy is a new chemical imaging technology in which a visible beam senses the photothermal effect induced by a pulsed infrared laser. This technology provides infrared spectroscopic information at sub-micron spatial resolution and enables infrared spectroscopy and imaging of living cells and organisms. Yet, current mid-infrared photothermal imaging sensitivity suffers from a weak dependance of scattering on temperature and the image quality is vulnerable to the speckles caused by scattering. Here, we present a novel version of mid-infrared photothermal microscopy in which thermo-sensitive fluorescent probes are harnessed to sense the mid-infrared photothermal effect. The fluorescence intensity can be modulated at the level of 1% per Kelvin, which is 100 times larger than the modulation of scattering intensity. In addition, fluorescence emission is free of interference, thus much improving the image quality. Moreover, fluorophores can target specific organelles or biomolecules, thus augmenting the specificity of photothermal imaging. Spectral fidelity is confirmed through fingerprinting a single bacterium. Finally, the photobleaching issue is successfully addressed through the development of a wide-field fluorescence-detected mid-infrared photothermal microscope which allows video rate bond-selective imaging of biological specimens.

Introduction

Visualizing the molecular composition and monitoring the molecular dynamics in a complex living system is a central theme of life science. Fluorescence microscopy has been widely adopted in biomedical research as it provides high speed background free imaging with exquisite molecular specificity[119-120] and superior resolution reaching the nanometer scale[121-123]. While fluorescence microscopy excels at mapping the distribution and dynamics of tagged organelles such as mitochondria and biomolecules such as glucose[124] and cholesterol[125], it does not provide chemical information of the tagged cells or organelles. Lacking such information hinders functional analysis, such as assessment of cell metabolic activity.

Providing chemical specificity, high speed and high sensitivity vibrational spectroscopic imaging is an emerging platform[126]. Recently developed coherent Raman scattering microscopy, based on coherent anti-Stokes Raman scattering (CARS) or stimulated Raman scattering (SRS), has allowed real-time vibrational imaging of biomolecules in living cells and tissues[127-128]. Advanced instrumentation has pushed the stimulated Raman spectral acquisition speed to microsecond scale[129]. Adoption of stable isotope probes and alkyne-based Raman tags greatly enhanced the detection sensitivity, specificity and functionality in SRS microscopy[128]. Being highly sensitive to C-H vibrations, CARS and SRS imaging have unveiled new signatures of lipid metabolism in a variety of biological systems[130-132]. In comparison, high-speed CARS or SRS imaging of fingerprint Raman bands remains difficult.

Mid-infrared spectroscopy is complementary to Raman spectroscopy. Unlike Raman scattering, the infrared absorption cross section in the fingerprint region is larger than in the high-wavenumber C-H vibrational region. Fourier transform infrared (FTIR) spectroscopy is one of the most extensively used techniques for chemical characterization and analysis of biological cells and tissues[133-136]. The inherent vibration absorption of mid-infrared photons by biological macromolecules including proteins, lipids, carbohydrates, and nucleic acids shows distinctive absorption bands. Shifts in relative heights of absorption bands, peak positions, and peak shape provide rich biomolecular information, including concentration, conformation, and orientation. FTIR spectroscopy has provided new insights in tissue classification[137], drug and tissue interaction[138], neurodegenerative diseases[139], cancer progression[140], and so on. However, the spatial resolution of infrared spectroscopic imaging is limited by the long mid-infrared illumination wavelength, ranging from 5 to 20 μm. Strong water absorption further hinders its application to living cells.

To overcome these limitations in infrared spectroscopy, a new platform, termed mid-infrared photothermal (MIP) microscopy, has been developed recently[13, 107, 112-113, 141-144] to reach sub-micron spatial resolution[145]. The MIP effect relies on a photothermal process in which infrared absorption corresponds to a specific molecular vibrational bond causes a localized temperature rise at the vicinity of target molecules. This photothermal effect consequently induces a change of refractive index and a thermal expansion. The MIP signal is then obtained by probing these changes using a visible beam which provides a much smaller diffraction limit than the mid-infrared illumination, enabling a

spatial resolution down to 300 nm[112] . Following the first demonstration of MIP imaging of living cells [141], technical innovations have been made to enable MIP detection in wide-field, using scattering or phase signals[146-149]. Meanwhile, MIP microscopy and its commercial product have found various applications in studying living cell, pharmaceuticals, viruses, and bacteria[113, 143, 150-155]. Yet, the photothermal effect induces only a tiny change in intensity and angular distribution of the scattered probe light, due to the weak thermal dependence of particle size and refractive index. Typical fractional change is on the order of $10^{-4}/K$, set by the intrinsic thermal properties of most materials. Such small modulation depth limits the signal to noise ratio (SNR), especially in the wide-field mode where the probe beam intensity at each pixel is limited by the well depth of a CMOS camera[147].

Here, we report a fluorescence detected MIP (F-MIP) microscope that utilizes thermo-sensitive fluorescent dyes as probes of the photothermal effect. The F-MIP principle is illustrated in **Figure 5.1a**. A sample stained with a thermo-sensitive dye is heated upon IR absorption by targeted molecules. The infrared pulse train heats the surrounding of the fluorescent probe and causes a temperature rise, which subsequently modulates the fluorescence emission efficiency. Such modulation is then measured by a lock-in amplifier. Using fluorescent dye to measure the temperature has been known[156-159]. Yet, it has not been used as a probe for infrared spectroscopic imaging. Our method offers a few key advantages over scattering-based MIP microscopy. The first is the utilization of much larger photothermal response of fluorescent dyes compared to scattering. Common fluorophores including FITC, Cy2, Cy3, Rhodamine, and green

fluorescent protein have temperature-dependent emission efficiency on the order of $1\%/K$, which is nearly 100 times larger than scattering dependence on temperature. Thus, one can in principle boost the mid-infrared photothermal imaging speed by two orders of magnitude. Second, as fluorescence appears at a new wavelength from the incident beam, it is insensitive to the laser relative intensity noise. Third, unlike scattering, fluorescence is incoherent and thus does not generate interference patterns. Finally, fluorescent probes can target specific cells, intracellular organelles, or specific molecules, thus offering an enhanced specificity beyond the reach by scattering-based MIP microscopy. In this study, we report two F-MIP systems, one in point-scanning mode and one in wide-field mode, as detailed below.

Methods

Scanning F-MIP Microscope

A pulsed mid-IR pump beam is generated by a tunable (from 1000 to 1886 cm^{-1}) quantum cascade laser (QCL, Daylight Solutions, MIRcat-2400) operating at 100 kHz repetition rate and 900 ns pulse duration. The IR beam passes through a calcium fluoride (CaF_2) cover glass and is then focused onto a sample through a gold-coating reflective objective lens (52×; numerical aperture (NA), 0.65; Edmund Optics, #66589). A continuous-wave probe laser (Cobolt, Samba) at 532 nm is focused onto the same spot from the opposite side by a refractive objective (60×; NA, 1.2; water immersion; Olympus, UPlanSApo). The probe beam is aligned to be collinear to the mid-IR pump beam. The reflective objective is fine tuned in 3D to ensure overlap of the two foci. A

scanning piezo stage (Mad City Labs, Nano-Bio 2200) with a maximum scanning speed of 200 μs/pixel is used to scan the sample. The fluorescence is collected by the same refractive objective, reflected by a dichroic mirror (Thorlabs, DMSP550R, 550 nm cutoff), filtered by a long-pass filter (Thorlabs, FEL0550, 550 nm cut-off), and then collected by a PMT (Hamamatsu, H10721-110). Specimens on a CaF_2 coverglass are first imaged by fluorescence. Then, the pulsed IR laser is turned on and the modulated fluorescence signal is collected by the same PMT. The F-MIP signal is extracted by a lock-in amplifier (Zurich Instruments, HF2LI). A laboratory-built resonant circuit is used to amplify the photocurrent from the PMT before it is sent to the lock-in. Before the reflective objective, the infrared laser passes through the CaF_2 slip and the reflected infrared laser intensity is measured by a mercury cadmium telluride (MCT) detector for normalization of IR power at each wavelength.

Wide-field F-MIP microscope

The IR pulses are generated by the same QCL used in scanning F-MIP. The visible probe beam for fluorescence excitation (wavelength at 488 nm or 520 nm) is obtained by second-harmonic generation of a quasi-continuous femtosecond laser tuned to 976 nm or 1040 nm (Coherent Inc, Chameleon, 140 fs, 80 MHz). Prior to second-harmonic generation, the femtosecond beam is chopped into a 200-kHz pulse train (300 ns pulse width) by an acousto-optical modulator (AOM, Gooch and Housego). The IR beam passes through the substrate and is weakly focused onto a sample by a parabolic mirror (f = 15 mm, Thorlabs, MPD00M9-M01). Using a Kohler illumination configuration, the probe beam is focused on the back focal plane of the objective lens (50×, 0.8 NA, Nikon)

by a condenser (f = 75 mm, AC254-075-A, Thorlabs). The fluorescence emission is collected by the same objective lens, and after a long pass filter, collected by a CMOS camera (FLIR, Grasshopper3 GS3-U3-51S5M). The F-MIP images are acquired by a virtual lock-in camera approach [147]. Briefly, a pulse generator (Emerald Pulse Generator, 9254-TZ50-US, Quantum Composers) generates a master clock signal at 200 kHz and externally triggers the QCL, the AOM and the CMOS camera to synchronize the IR pump pulses, the probe pulses, and camera exposure. The schematic is shown in **Fig. 5.4a** in the results section.

Cancer cell culture and staining

Mia Paca2 cells were purchased from the American Type Culture Collection (ATCC). The cells were cultured in RPMI 1640 medium supplemented with 10% FBS and 1% P/S. All cells were maintained at 37^{o}C in a humidified incubator with 5% CO_2 supply. For Nile red staining, cells were incubated with 10 μM Nile Red (Invitrogen) for 30 minutes at room temperature followed with 15 minutes fixation in 10% neutral buffered formalin. For rhodamine 123 (Invitrogen) staining, cells were incubated with 10 μg/ml rhodamine 123 for 30 minutes at 37^{o}C.

Bacterial culture and staining: Staphylococcus aureus (S. aureus) was incubated in a MHB medium for 10 h. After centrifuging and washing in phosphate-buffered saline (PBS), the bacteria were fixed by formalin solution for 0.5 h. Rhodamine 6G or Cy2 at 10^{-4} M was then added into the bacteria pellet. The pellet was then resuspended and incubated for 1 h. With final washing steps, 2 μL sample were dried on a CaF_2 coverslip for imaging. Shigella flexneri expressing GFP was grown overnight at 37°C on a tryptic

soy agar plate. Colonies with green fluorescence were picked up by sterile inoculation loops and then resuspended in PBS. The bacterial solution was diluted by optical density at 600 nm (OD600) to 0.1. The bacteria were then fixed by 10% Formalin for 30 min at room temperature. The bacteria solution was washed twice by PBS before imaging.

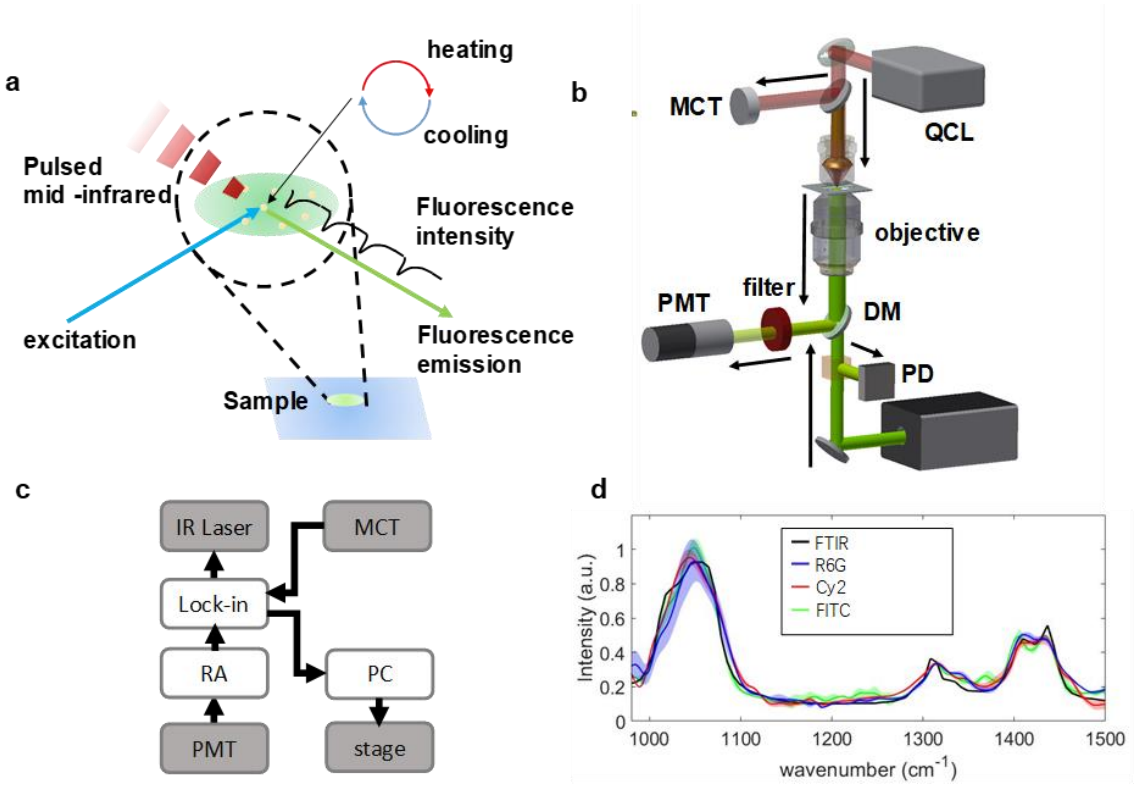

Figure 5.1 Fluorescence-detected mid-infrared photothermal (F-MIP) sensing principle, point scanning microscope, and spectral fidelity.

(a) Modulation of fluorophore emission intensity by pulsed infrared pump of surrounding molecules. (b) Schematic of a point scanning F-MIP microscope. A pulsed mid-IR pump beam from a quantum cascade laser (QCL) and a continuous visible fluorescence excitation beam are focused at the sample with a reflective objective and a water-immersion objective, respectively. The fluorescence emission is reflected by a dichroic mirror (DM), filtered and directed to a photomultiplier tube (PMT). A beam splitter is placed to reflect the scattered visible beam to a photodiode for scattering-based

MIP (Sc-MIP) imaging. (c) Electronics connection. The photothermal signal is detected by a PMT connected to a resonant amplifier (RA) and detected by a lock-in amplifier. A PC is used for controlling the scanning stage and data acquisition. (d) F-MIP spectra of DMSO supplemented with various thermo-sensitive fluorescent dyes. For each dye, standard deviation of three independent measurements is shown at each wavenumber. The FTIR spectrum of DMSO (black) is shown for comparison.

Results and Discussion

Point-scanning F-MIP microscope and spectral fidelity. Based on the principle shown in **Figure 5.1a**, we have built a scanning F-MIP microscope as shown in **Figure 5.1b**. A QCL laser provides IR pulses tunable in the entire fingerprint region. The repetition rate and pulse width were set to be 100 kHz and 900 nanoseconds, respectively. Two CW lasers at 532 nm and 488 nm were used for fluorescence excitation. The fluorescence was detected by a photomultiplier tube and the F-MIP signal was extracted by a lock-in amplifier. On the same setup, a photodiode was also installed for scattering-based MIP (Sc-MIP) imaging using the 532-nm laser as the probe beam. The electronics connections are shown in **Figure 5.1c**.

Using this system, we have validated the spectral fidelity of F-MIP microscope. We dissolved various thermo-sensitive dyes in DMSO, at 100 μM concentration. We then recorded the F-MIP signals while scanning the QCL laser. At each wavenumber, the F-MIP intensity was normalized by the IR intensity measured by MCT. In all cases (**Figure 5.1d**), the F-MIP spectra show the same peak intensity and width as the FITR spectrum of DMSO. Importantly, because the dye concentration (100 μM) is much lower than DMSO concentration (14 M), the dyes do not interfere with the F-MIP spectra.

These data demonstrate the F-MIP microscope is able to produce reliable spectral information.

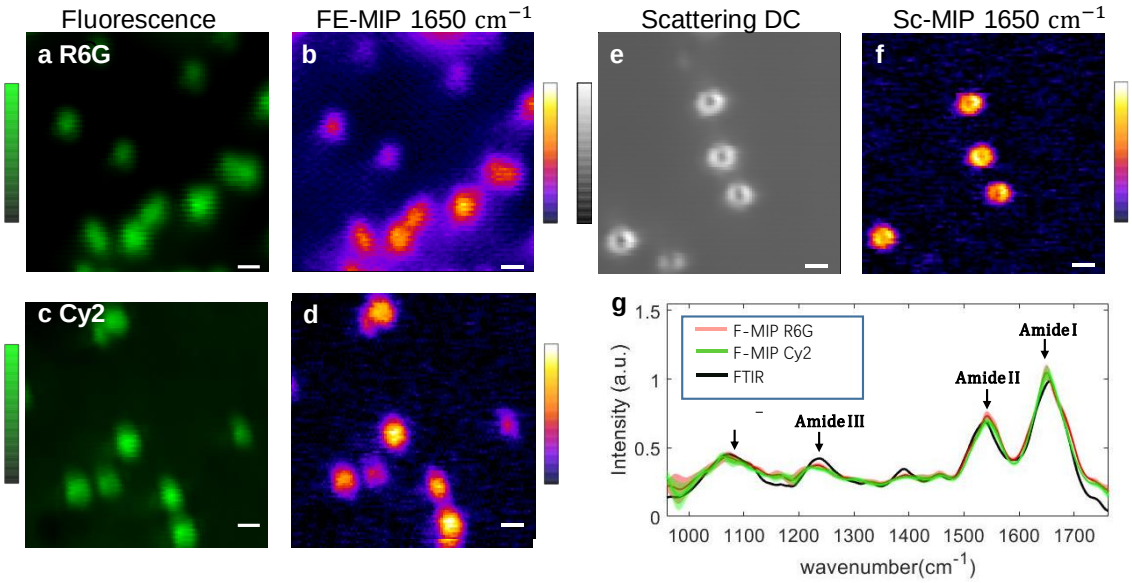

Figure 5.2 F-MIP imaging and fingerprinting single S. aureus.

(a) Fluorescence image of S. aureus stained with R6G. Scale bar: 1 μm. Pixel dwell time: 1 ms. Fluorescence excitation: 0.025 mW at 532 nm. (b) F-MIP image of same S. aureus at 1650 cm^{-1}. (c) Fluorescence image of S. aureus stained with Cy2. Fluorescence excitation: 0.025 mW at 488 nm. (d) F-MIP image of same S. aureus at 1650 cm^{-1}. (e) Scattering image of S. aureus. Pixel dwell time: 1 ms. Visible probe power: 1.5 mW. (f) Sc-MIP image of same S. aureus at 1650 cm^{-1}. (g) The fingerprint spectra of S. aureus measured by F-MIP and Sc-MIP, respectively. For both F-MIP and Sc-MIP, the IR laser power 1650 cm^{-1} was 10.2 mW at sample. The FTIR spectrum recorded from a film of dried S. aureus was adopted from ref[27].

F-MIP imaging and fingerprinting of single bacteria. We applied the F-MIP microscope to image single S. aureus bacteria to evaluate its chemical imaging capability on biological specimens (**Figure 5.2a-d**). The S. aureus culture was diluted to a concentration of around 5×10^5/mL and then dried on a CaF_2 substrate. The S. aureus

particles were stained with fluorescence dye Cy2 and R6G, respectively. For each specimen, we acquired fluorescence and F-MIP images of the same bacteria at 1650 cm^{-1} targeting the amide I band. For the F-MIP images, SNRs of 26 and 34 were achieved for R6G and Cy2 labeled bacteria at the fluorescence excitation power of 0.025 mW at the sample. For comparison, we recorded scattering and MIP images of the same specimen (**Figure 5.2e,f**). In order to obtain a similar SNR of 37, an excitation power of 1.5 mW at sample was required, which is 60 times of the probe power used for F-MIP. On a single bacterium, we recorded the vibrational fingerprint spectrum (**Figure 5.2g**). The F-MIP spectra based on R6G and Cy2 matches well the FTIR spectrum, showing distinct peaks at 1650, 1550, and 1080 cm^{-1} for protein amide I, protein amide II, and nuclei acid phosphate vibrations, respectively. This comparison demonstrates the spectral fidelity of F-MIP in single bacterium analysis. Notably, the scattering and the Sc-MIP image both show a ring structure, with bright contrast from the peripheral of the cell (**Figure 5.2e,f**), whereas the F-MIP images (**Figure 5.2b,d**) show bright contrast from the entire cell. This result indicates that F-MIP is immune to edge-enhanced back scattering from a sizable particle.

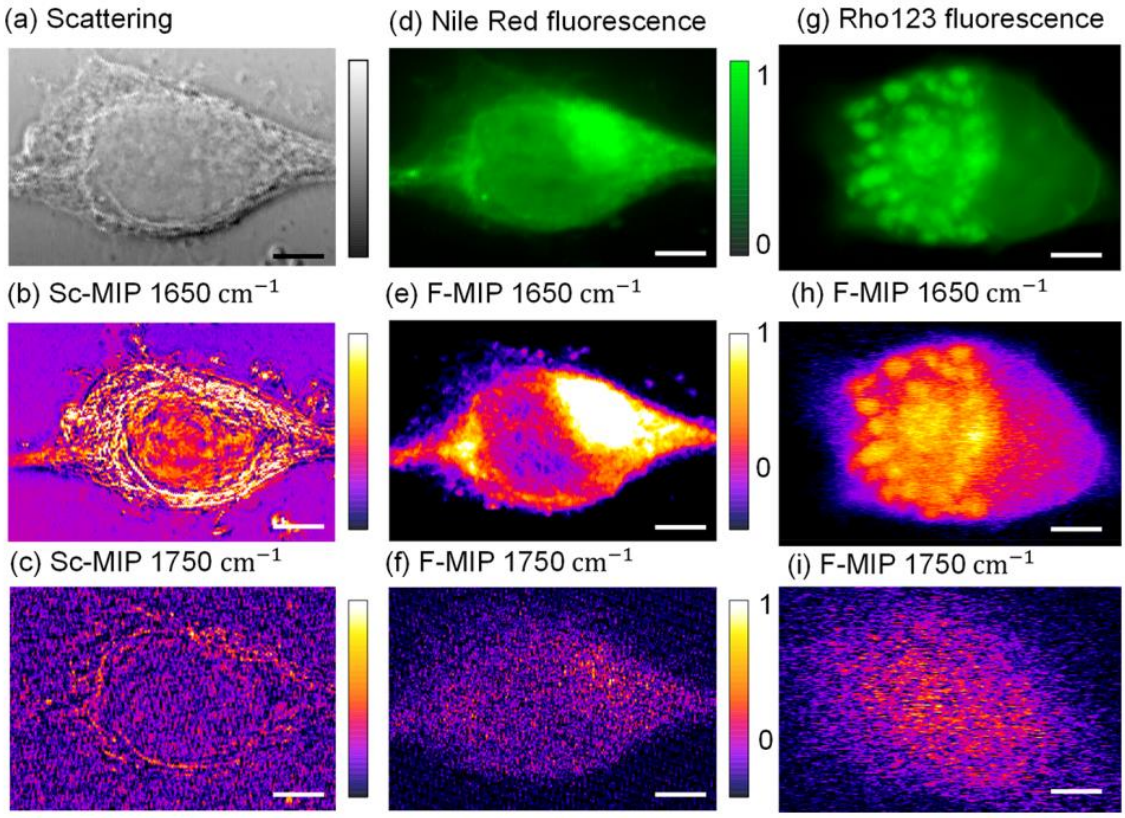

Figure 5.3 Sc-MIP and F-MIP images of living MiaPaca2 cancer cells.

(a) Scattering image of a MiaPaca2 cell. (b) Sc-MIP image of the same cell at 1650 cm^{-1}. (c) Sc-MIP image at 1750 cm^{-1}. (d) Fluorescence image of the same MiaPaca2 cell stained with Nile red. The probe laser is at 532 nm. (e) F-MIP image at 1650 cm^{-1}. (f) F-MIP image at 1750 cm^{-1}. (g) Fluorescence image of a different MiaPaca2 cell stained with Rhodamine 123 (Rho123). The probe laser is at 488 nm. (h) F-MIP image at 1650 cm^{-1}. (i) F-MIP image at 1750 cm^{-1}. Scale bar: 5 μm.

Sc-MIP and F-MIP imaging of cancer cells

Compared to bacteria, eukaryotic cells contain a nucleus and highly organized organelles in the cytoplasm. In the transmission image shown in **Figure 5.3a**, the scattering-based contrast shows the overall cell morphology. Accordingly, the Sc-MIP image (**Figure 5.3b**) at 1650 cm^{-1} corresponding to the amide I band shows the protein

content inside the nucleus and protein-rich structures in the cytoplasm, without specificity to a certain organelle. The contrast decreases when the IR laser is tuned to 1750 cm^{-1} (**Figure 5.3c**), showing the chemical specificity. In contrast, fluorescence microscopy is able to visualize specific biomolecules and/or intracellular organelles via the versatile fluorescent probes. For instance, Nile red can selectively stain the intracellular lipid droplets and membranes[160] while Rhodamine 123 is a specific probe for localizing mitochondria in living cells[161]. By staining the same cell with Nile red and excitation of the dye at 532 nm, phospholipid membranes in the cell are visualized (**Figure 5.3d**), where the brightest contrast is likely from the ER membrane. The F-MIP image at 1650 cm^{-1} gives the distribution of proteins in areas labeled by Nile red (**Figure 5.3e**). The contrast nearly disappears when the IR laser is tuned to 1750 cm^{-1} (**Figure 5.3f**), showing the chemical specificity. To show that our method is applicable to other dyes, we performed an independent experiment in which living MiaPaca2 cells were labeled by Rhodamine 123 targeting intracellular mitochondria (**Figure 5.3g**). In accordance, the F-MIP image at 1650 cm^{-1} shows selective and bright contrast from the Rhodamine 123 labeled region (**Figure 5.3h**) and the contrast disappears at 1750 cm^{-1} (**Figure 5.3i**).

From point-scanning to wide-field F-MIP. In the above experiments, the power used for F-MIP imaging is at the microwatt level and is 60 times less than the power used for scattering MIP imaging. The extremely low photon budget for F-MIP imaging opens the opportunity of increasing the throughput via wide-field illumination with IR pump pulses and visible probe pulses. Importantly, compared to scanning F-MIP, wide-field F-MIP could significantly reduce the fluorophore photobleaching rate based on the

following consideration. In our experiment, the IR pulse is 900 ns in duration and the pulse-to-pulse duration is 10 μs. In the aqueous environment, the temperature profile largely follows the IR pulse. Thus, in a scanning experiment where a continuous wave probe laser is used, the duty cycle is about 10%. Yet, in a wide field measurement, we only need two visible pulses to measure the IR-on and IR-off states. Thus, the duty cycle can be 50%. In this way, the probe laser power can be much reduced, thus alleviating the photobleaching issue. Notably, our group recently demonstrated scattering-based wide-field MIP imaging147. Yet, the signal to noise ratio at the high-speed mode is limited by the weak dependence of scattering on temperature and the small well depth of the CMOS camera. As a result, a large number of integrations were needed to accumulate sufficient photons to probe the MIP signal. Unlike the scattering photons, the fluorescence usually does not saturate the camera. Due to the high thermo-sensitivity of fluorescent probes, it is anticipated that the MIP signal can be extracted from two sequential frames (hot and cold) without further average.

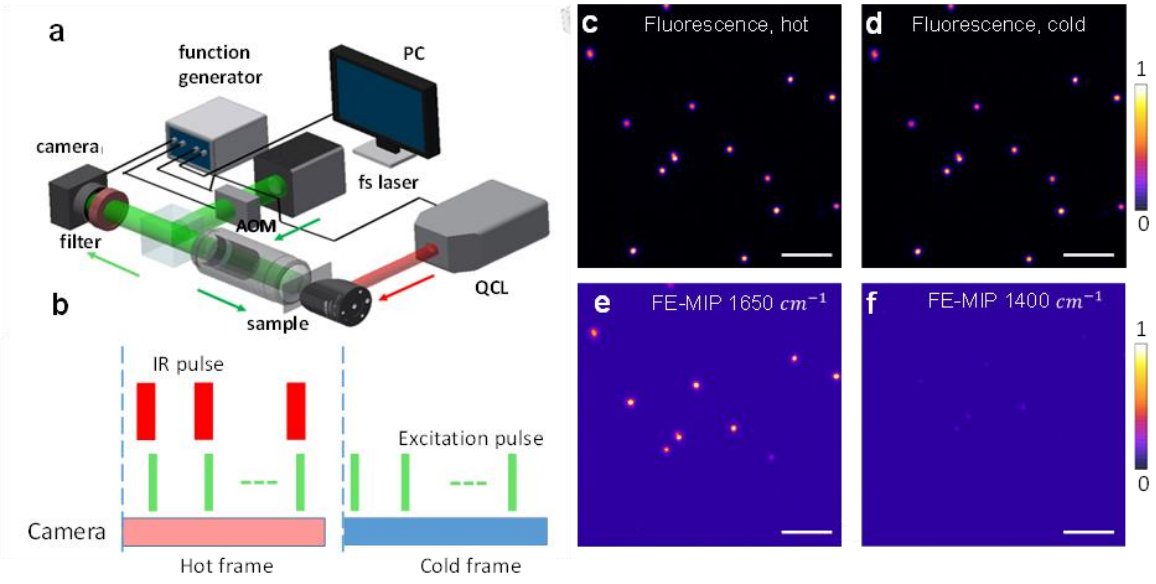

Figure 5.4 The wide field F-MIP microscope.

(a) Schematic of the wide field F-MIP microscope. The infrared laser generated by the QCL is focused by a parabolic mirror. The visible light modulated by an AOM illuminates the sample and excites the fluorescence. The fluorescence is filtered and collected by a CMOS camera. (b) Temporal synchronization of IR pump pulse, fluorescence excitation pulse, and camera exposure. (c,d) Wide field fluorescence image of Cy2-stained S. aureus with IR on and IR off, designated as hot and cold, respectively. (e) Wide field F-MIP at 1650 cm^{-1} (f) F-MIP at 1400 cm^{-1} off resonance. Scale bar: 10μ m. Fluorescence excitation: 488 nm, 1 mW. IR pulse rate: 200 KHz. Camera frame rate: 40 Hz.

Wide Field F-MIP Microscope

Based on the above rationale, we built a wide field F-MIP microscope as shown in **Figure 5.4a**. The pulsed Infrared laser is weakly focused onto a sample by a parabolic mirror. An 80-MHz femtosecond laser is modulated by an AOM and frequency-doubled to visible window. The broad bandwidth of femtosecond pulses reduces speckles in scattering-based MIP imaging. The virtual lock-in detection scheme is illustrated in **Figure 5.4b**. The fluorescence excitation pulse is synchronized with the IR pump pulse.

In the cold frame, no IR pump pulses heat the sample. The camera detects the hot and cold frames sequentially at 40 Hz frame rate. The difference (cold – hot) generates the MIP image. The average probe Laser power was around 1 mW and the exposure time was 300 ns. The IR power was in the range from 5 to 15 mW depending on the spectral window examined. To characterize the spatial resolution, we mapped Cy2-label polystyrene beads with diameter of 500 nm, the F-MIP intensity profile shows a full-width at half maxim of 610 nm. After deconvolution with particle size, the spatial resolution is estimated to be 390 nm, which is close to the diffraction limit of the 0.8 NA objective.

To demonstrate the applicability of wide-field F-MIP to biological specimens, we deposited S. aureus stained with Cy2 onto a silicon substrate and measured the fluorescence with IR on and IR off sequentially. The hot frame and the cold frame are illustrated in **Figure 5.4c** and **d**, respectively. By subtracting the hot from the cold frame, the intensity difference generates the F-MIP image shown in **Figure 5.4e**. When the IR laser is tuned to 1650 cm^{-1}, corresponding to the amide I band of proteins, a signal to noise ratio of 30 was obtained. The IR pulse only heats the upper half of the field of view. For this reason, only the S. aureus particles in the upper part give the F-MIP contrast. When the IR laser is tuned to 1400 cm^{-1}, off resonance to major IR peaks, the contrast nearly disappears (**Figure 5.4f**). We note that the wide-field F-MIP imaging speed of 20 frames per second is 2000 times faster than the scanning F-MIP imaging speed (100 seconds per frame with a pixel dwell time of 1.0 millisecond).

Performance comparison between wide-field Sc-MIP and F-MIP. Next, we

compared the performance of fluorescence-enhanced and scattering-based MIP imaging in the wide field mode, using S. aureus on a silicon substrate as testbed. **Figure 5.5a-c** shows the fluorescence and F-MIP images of individual S. aureus with the IR laser tuned to 1650 cm^{-1}. The signal to noise ratio for a single bacterium reaches 33 in single frame F-MIP and 275 after 100 frames average. **Figure 5.5d-f** shows the scattering and SC-MIP images of individual S. aureus with the IR laser tuned to 1650 cm^{-1}. **Figure 5.5g-h** shows the intensity profile across the white line indicated in the images. The Sc-MIP contrast is completely buried in the speckle pattern in singe frame acquisition. After 100 frames average, the signal to noise ratio reaches 14, which is 20 times lower than F-MIP of the same sample. The much higher signal to noise ratio in F-MIP can be attributed to the lack of shot noise from scattered photons and the much larger thermo-sensitivity of the fluorescence probe. **Figure 5.5h** shows similar line width for the bacterium in Sc-MIP and F-MIP. However, the F-MIP intensity does not suffer from the interference (i.e. the dark ring around the peak) encountered in the Sc-MIP image. **Figure 5.5i-j** shows the F-MIP and Sc-MIP intensities from a single bacterium in sequentially acquired hot and cold frames. The modulation depth, defined as percentage of intensity difference between hot and cold frames, is found to be about 4% for F-MIP, but is buried in frame to frame fluctuations in Sc-MIP. Moreover, **Figure 5.5i** shows negligible photobleaching in the recorded 50 frames over a period of 1.25 seconds.

Besides fluorescent dyes, we tested the feasibility of F-MIP imaging for cells expressing green fluorescent proteins (GFPs). It has been shown that GFPs are highly thermo-sensitive with 1% intensity decrease per degree in temperature rise [162-163].

Accordingly, in F-MIP imaging of Sheila Flexneri bacteria expressing GFP **(Figure 5.5k-m**), we observed 2% fluorescence intensity difference between cold and hot frames (**Figure 5.5n**). The signal to noise ratio reaches 10 and 97 in single frame and 100 frames average, respectively. The recorded 50 frames only experienced 3% photo-bleaching. The fluorescence fluctuation from frame to frame was due to laser instability.

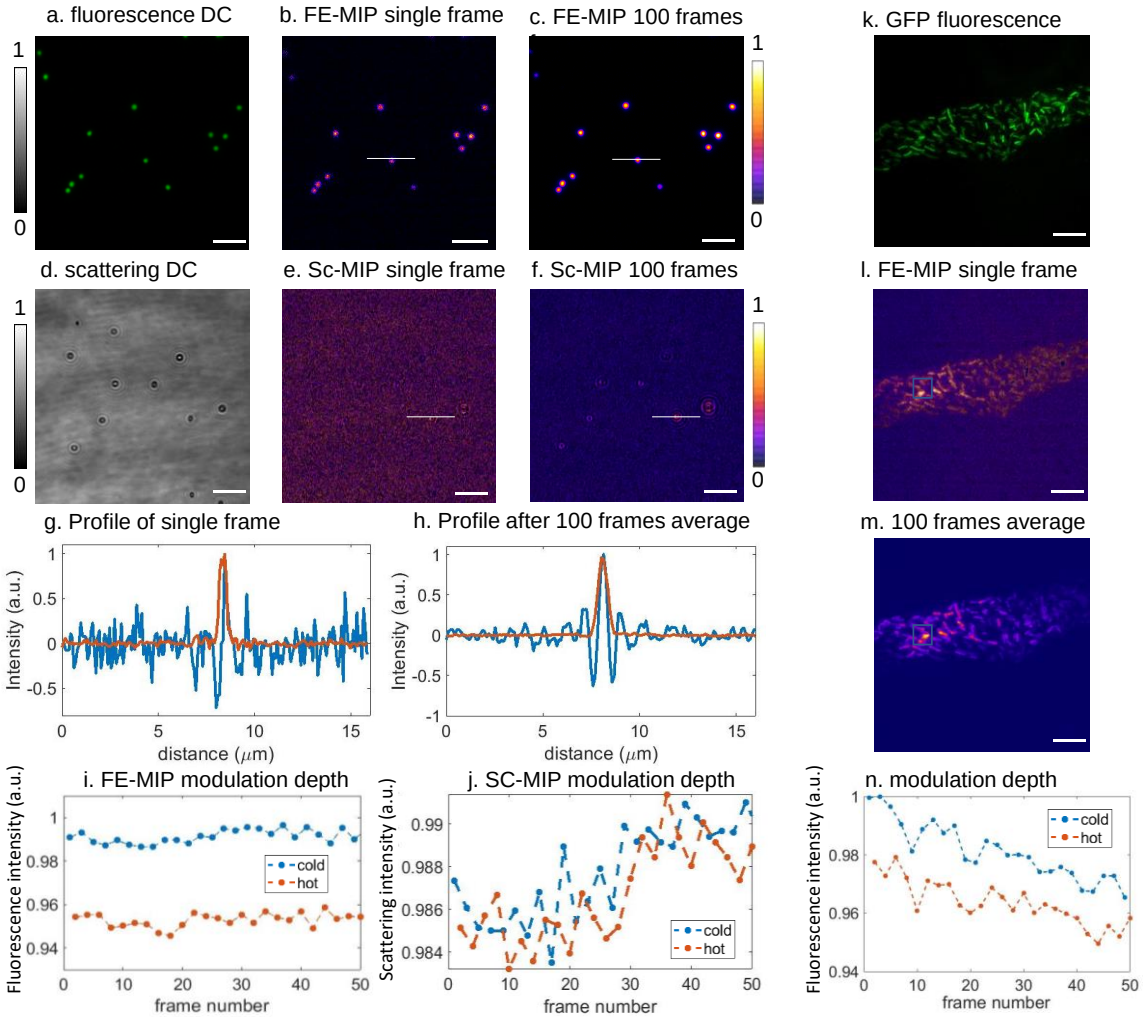

Figure 5.5 Performance comparison between wide field SC-MIP and wide field F-MIP systems.

(a) Fluorescence image of S. aureus deposited on a silicon substrate. (b) Single frame F-MIP image of the same cells at 20 Hz speed. (c) F-MIP image of the same cells with 100 frames average. (d) Scattering image of S. aureus deposited on a silicon substrate. (e) Single frame Sc-MIP of the same cells shown in panel d at 20 Hz speed. (f) Sc-MIP of the same field of view with 100 frames average. (g) Intensity profile along the white line marked in panel b and e. (h) Intensity profile along the white line marked in panel c and f. (i) Fluorescence intensity of single S. aureus in sequentially acquired hot and cold frames. (j) Scattering intensity of single S. aureus in sequentially acquired hot and cold frames. The IR laser is tuned to 1650 cm^{-1} for data in panel a to h. (k) Fluorescence image of Sheila Flexneri bacteria expressing GFP. (l) Single frame F-MIP of the same bacteria at 1650 cm^{-1}. (m) F-MIP image of the same field of view with 100 frames average. (n) Fluorescence intensity of the square area in sequentially acquired hot and cold frames.

Recently, the Tokmakoff and Min groups reported two related methods that code vibrational signatures into fluorescence spectroscopy, based on femtosecond-scale infrared pulse excitation [164] and picosecond-scale stimulated Raman excitation [165], respectively. These methods are based on the up-conversion process, in which vibrational excitation and fluorescence emission are from the same dye molecule. Our F-MIP method is fundamentally different in that fluorescence emission efficiency from a thermo-sensitive probe is modulated by nanosecond-scale pulsed infrared excitation of molecules of interest surrounding the probe. We note that the Simpson group independently developed a fluorescence-detected scanning photothermal microscope for chemical imaging of pharmaceutical samples[166]. Their work and the current study show broad applications enabled by F-MIP microscopy.

Photothermal microscopy is a pump-probe technique involving modulation of the pump beam and demodulation of the signal usually by a lock-in. In this work, the sensitivity is defined as the modulation depth, $\Delta I_{pr}/I_{pr}=\sigma I_p$, where σ is related to the

thermal sensitivity, I_p is the IR pump, and I_{pr} is the probe intensity. In this sense, fluorescence-detected MIP is more sensitive than scattering-based MIP due to the much larger thermo-sensitivity of fluorophores. Experimentally, as shown in **Figure 5.5**, the modulation depth in F-MIP is about 2%, whereas the modulation is buried in frame to frame intensity fluctuation in Sc-MIP. These data are in good agreement with our model.

We have defined the imaging SNR as the ratio of signal intensity from single particles to pixel-to-pixel background fluctuations. Thus, in Sc-MIP, the SNR = Signal / (Noise_PD + Noise_photon). In F-MIP, SNR = Signal / Noise_PMT. Under the shot noise limit, the photon noise is proportional to $\sqrt{I_{pr}}$. Based on this model, the SNR depends on the value of σ and the probe beam intensity if we assume that same IR pump beam is used. In scanning MIP microscopy, the probe power (~ 10 mW) in the scattering mode can be 10,000 times larger than that in the fluorescence mode (~ 1 μW). In this case, the SNR in Sc-MIP is dominated by the photon noise, and the SNR = $\sigma_{sc} I_p \sqrt{I_{pr}}$. In F-MIP, the SNR = $\sigma_f I_p I_{pr}$/Noise_PMT. In this case, the SNR in F-MIP is a trade-off between a much larger σ and a much smaller I_{pr} used. Experimentally, we observed similar SNR in F-MIP compared to Sc-MIP (See Figure 2). However, in wide-field MIP microscopy, limited by the well depth of a common CMOS camera, the probe power at each pixel is at the nW level for both the scattering and the fluorescence modality. In this case, the detector noises dominate, and the SNR in F-MIP can be theoretically larger by two orders of magnitude than that in Sc-MIP. In the experiment, we showed that the SNR in wide-field MIP is 20 times larger than that in wide-field Sc-MIP.

Theoretically, F-MIP microscopy is based the thermal diffusion from the target molecule to the fluorescent probe. The thermal diffusion length is defined as $\mu_t = 2\sqrt{\alpha t}$, where α is the thermal diffusivity[167-168]. In an aqueous environment, the value of α is 1.4×10^{-7} m^2/s [169]. In our wide-field F-MIP experiment, the IR pulse is 900 ns in duration and the fluorescence excitation pulse is 300 nm. If we set the pump-probe delay to be 900 ns, the thermal diffusion length is ~700 nm, which is slightly larger than the diffraction limit of the visible probe beam. If one can use IR pump and visible probe pulse of 5 ns duration and the pump-probe delay is set to be 5 ns, the thermal diffusion length can be reduced to 50 nm. In this case, one can detect the chemical content surrounding the fluorescence probe on the nanoscale. If the probe is conjugated to the target molecule, like a GFP conjugated to a protein, the intramolecular vibrational redistribution on the picosecond scale can be much faster than inter-molecular vibrational redistribution. In principle, it could create an intramolecular F-MIP signal, assuming that picosecond IR pump and probe pulses are used.

Researchers have studied the dependence of thermo-sensitivity on two important environmental factors, salt concentration and viscosity. It was shown that thermo-sensitivity is nearly independent of salt concentration in the 10 to 100 mM range[170]. Also, it was shown that PEG BODIPY lifetime in cells is due to temperature and independent of changes in viscosity[171]. These data suggest that fluorophores' thermo-sensitivity can be used as a reliable readout of the mid-infrared photothermal effect.

F-MIP microscopy opens new opportunities for live-cell chemical imaging. First, by F-MIP spectroscopic imaging of specific organelles (e.g. lipid droplets) specifically labeled by a thermo-sensitive fluorophore (e.g. BODIPY), one will be able to tell not only the amount and distribution, but also the composition of lipids, which is beyond the reach by fluorescence microscopy alone. Such capacity will allow quantitation of lipid metabolism in cells under various conditions (e.g., in response to a stress). Second, F-MIP microscopy opens new ways to push the boundary of mid-infrared photothermal microscopy. For example, integration of infrared laser excitation and light field fluorescence probing is expected to enable single-shot volumetric infrared spectroscopic imaging at sub-micron spatial resolution. Additionally, structured illumination can be harnessed to break the diffraction limit of the visible beam, which is expected to push the spatial resolution of MIP microscopy to a new level.

On the limitation side, F-MIP microscopy relies labeling the specimen with a thermo-sensitive dye and the signal level depends on the dye concentration. For quantitative analysis, one could normalize the F-MIP signal with the direct fluorescence signal. As shown in **Figure S3**, the normalized F-MIPs images exhibit a more uniform distribution of the signal arising from proteins in regions labeled by the dyes. For the same reason, the SNR in F-MIP microscopy depends on the number of fluorophores in the particles to be detected. For biological nanoparticles such as virion particles, the small number of fluorescent labels may give a low signal level and limit the SNR accordingly. In such case, detection of interferometric scattering becomes a more suitable approach. In fact,

detection and fingerprinting of single virus particles has been achieved by an interferometric mid-infrared photothermal microscope[10].

Conclusion

In efforts to push the detection limit and increase the specificity of optically detected mid-infrared photothermal microscopy, a new platform termed fluorescence-enhanced mid-infrared photothermal (F-MIP) microscopy is developed. Our platform harnesses thermo-sensitive fluorescent probes to sense surrounding temperature rise induced by pulsed infrared excitation. High spectral fidelity is demonstrated for fluorescent probes in DMSO solution and inside biological cells. In the point scanning modality, we have demonstrated F-MIP imaging and fingerprinting of a single bacterium. While using fluorescence as a read out, the fingerprint information would allow functional assessment of biological specimen, such as metabolic response of bacteria to antibiotics treatment. Furthermore, organelle-specific F-MIP imaging is achieved, which opens exciting opportunities of probing the chemical content of intracellular organelles. In the wide-field modality, we demonstrated video rate, high signal to noise ratio, speckle-free F-MIP imaging of individual bacteria. Finally, our platform is applicable to biological cells expressing GFP. This approach opens new opportunities of monitoring secondary structure of specific proteins tagged by GFP, which is beyond the reach by IR spectroscopy or fluorescence spectroscopy alone.

APPENDIX – PUBLICATIONS

[1] Hui, J., Cao, Y., **Zhang, Yi**., Kole, A., Wang, P., Yu, G., Eakins, G., Sturek, M., Chen, W., & Cheng, J. X. (2017). Real-time intravascular photoacoustic-ultrasound imaging of lipid-laden plaque in human coronary artery at 16 frames per second. *Scientific reports*, *7*(1), 1417. https://doi.org/10.1038/s41598-017-01649-9

[2] Cao, Y., Kole, A., Hui, J., **Zhang, Yi**., Mai, J., Alloosh, M., Sturek, M., & Cheng, J. X. (2018). Fast assessment of lipid content in arteries in vivo by intravascular photoacoustic tomography. *Scientific reports*, *8*(1), 2400. https://doi.org/10.1038/s41598-018-20881-5

[3] **Zhang, Yi**., Cao, Y., & Cheng, J. X. (2019). High-resolution photoacoustic endoscope through beam self-cleaning in a graded index fiber. *Optics letters*, *44*(15), 3841–3844. https://doi.org/10.1364/OL.44.003841

[4] **Zhang, Yi**., Yurdakul, C., Devaux, A. J., Wang, L., Xu, X. G., Connor, J. H., Ünlü, M. S., & Cheng, J. X. (2021). Vibrational Spectroscopic Detection of a Single Virus by Mid-Infrared Photothermal Microscopy. *Analytical chemistry*, *93*(8), 4100–4107. https://doi.org/10.1021/acs.analchem.0c05333

[5] **Zhang, Yi**., Zong, H., Zong, C., Tan, Y., Zhang, M., Zhan, Y., & Cheng, J. X. (2021). Fluorescence-Detected Mid-Infrared Photothermal Microscopy. *Journal of the American Chemical Society*, *143*(30), 11490–11499. https://doi.org/10.1021/jacs.1c03642

[6] **Zhang, Yi**, Xu, Y., Jia, D., Yang, Q., & Cheng, J.X. (2021). Volumetric Fluorescence-Detected Mid-Infrared Photothermal Microscopy through Fourier Light Field Imaging. *Optica*, **In preparation.**

[7] Zhang, Yi, Taylor, E., Huang, N., Hamilton, J., & Cheng, J.X. Longitudinal intravascular photoacoustic imaging of inflammatory atherosclerotic plaque in cholesterol fed rabbits **,** *Biomedical Optics Express.* **In preparation.**

BIBLIOGRAPHY

1. Rosamond, W.; Flegal, K.; Furie, K.; Go, A.; Greenlund, K.; Haase, N.; Hailpern, S. M.; Ho, M.; Howard, V.; Kissela, B.; Kittner, S.; Lloyd-Jones, D.; McDermott, M.; Meigs, J.; Moy, C.; Nichol, G.; O'Donnell, C.; Roger, V.; Sorlie, P.; Steinberger, J.; Thom, T.; Wilson, M.; Hong, Y., Heart disease and stroke statistics--2008 update: a report from the American Heart Association Statistics Committee and Stroke Statistics Subcommittee. *Circulation* **2008,** *117* (4), e25-146.

2. Falk, E.; Shah, P. K.; Fuster, V., Coronary plaque disruption. *Circulation* **1995,** *92* (3), 657-671.

3. Schaar, J. A.; Muller, J. E.; Falk, E.; Virmani, R.; Fuster, V.; Serruys, P. W.; Colombo, A.; Stefanadis, C.; Ward Casscells, S.; Moreno, P. R.; Maseri, A.; van der Steen, A. F., Terminology for high-risk and vulnerable coronary artery plaques. Report of a meeting on the vulnerable plaque, June 17 and 18, 2003, Santorini, Greece. *European Heart Journal* **2004,** *25* (12), 1077-1082.

4. Waxman, S.; Ishibashi, F.; Muller, J. E., Detection and treatment of vulnerable plaques and vulnerable patients: novel approaches to prevention of coronary events. *Circulation* **2006,** *114* (22), 2390-2411.

5. Oraevsky, A. A.; Karabutov, A. A., Optoacoustic tomography. In *Biomedical Photonics: Handbook*, 2003; pp 34-1-34-34.

6. Wang, B.; Karpiouk, A.; Yeager, D.; Amirian, J.; Litovsky, S.; Smalling, R.; Emelianov, S., In vivo intravascular ultrasound-guided photoacoustic imaging of lipid in plaques using an animal model of atherosclerosis. *Ultrasound in Medicine & Biology* **2012,** *38* (12), 2098-2103.

7. Zhang, D.; Li, C.; Zhang, C.; Slipchenko, M. N.; Eakins, G.; Cheng, J. X., Depth-resolved mid-infrared photothermal imaging of living cells and organisms with submicrometer spatial resolution. *Science advances* **2016,** *2* (9), e1600521.

8. Bai, Y.; Zhang, D.; Li, C.; Liu, C.; Cheng, J. X., Bond-Selective Imaging of Cells by Mid-Infrared Photothermal Microscopy in High Wavenumber Region. *The journal of physical chemistry. B* **2017,** *121* (44), 10249-10255.

9. Li, C.; Zhang, D.; Slipchenko, M. N.; Cheng, J. X., Mid-Infrared Photothermal Imaging of Active Pharmaceutical Ingredients at Submicrometer Spatial Resolution. *Analytical chemistry* **2017,** *89* (9), 4863-4867.

10. Zhang, Y.; Yurdakul, C.; Devaux, A. J.; Wang, L.; Xu, X. G.; Connor, J. H.; Ünlü, M. S.; Cheng, J. X., Vibrational Spectroscopic Detection of a Single Virus by Mid-Infrared Photothermal Microscopy. *Analytical chemistry* **2021,** *93* (8), 4100-4107.

11. Shi, J.; Wong, T. T. W.; He, Y.; Li, L.; Zhang, R.; Yung, C. S.; Hwang, J.; Maslov, K.; Wang, L. V., High-resolution, high-contrast mid-infrared imaging of fresh biological samples with ultraviolet-localized photoacoustic microscopy. *Nature photonics* **2019,** *13*, 609-615.

12. Bialkowski, S. E., *Photothermal spectroscopy methods for chemical analysis*. John Wiley & Sons: 1996; Vol. 177.

13. Li, Z.; Aleshire, K.; Kuno, M.; Hartland, G. V., Super-Resolution Far-Field Infrared Imaging by Photothermal Heterodyne Imaging. *The journal of physical chemistry. B* **2017,** *121* (37), 8838-8846.

14. Hawkes, J. B.; Astheimer, R. W., The temperature coefficient of the refractive index of water. *Journal of the Optical Society of America* **1948,** *38* (9), 804-806.

15. Tokeshi, M.; Uchida, M.; Hibara, A.; Sawada, T.; Kitamori, T., Determination of subyoctomole amounts of nonfluorescent molecules using a thermal lens microscope: subsingle-molecule determination. *Analytical chemistry* **2001,** *73* (9), 2112-2116.

16. Wang, X. D.; Wolfbeis, O. S.; Meier, R. J., Luminescent probes and sensors for temperature. *Chemical Society Reviews* **2013,** *42* (19), 7834-7869.

17. Lakowicz, J. R., *Principles of fluorescence spectroscopy*. Springer science & business media: 2013.

18. Ferguson, J.; Mau, A., Spontaneous and stimulated emission from dyes. Spectroscopy of the neutral molecules of acridine orange, proflavine, and rhodamine B. *Australian Journal of Chemistry* **1973,** *26*, 1617-1624.

19. Wienken, C. J.; Baaske, P.; Rothbauer, U.; Braun, D.; Duhr, S., Protein-binding assays in biological liquids using microscale thermophoresis. *Nat Commun* **2010,** *1*, 100.

20. Zhang, Y.; Cao, Y.; Cheng, J. X., High-resolution photoacoustic endoscope through beam self-cleaning in a graded index fiber. *Optics letters* **2019,** *44* (15), 3841-3844.

21. Jansen, K.; van Soest, G.; van der Steen, A. F., Intravascular photoacoustic imaging: a new tool for vulnerable plaque identification. *Ultrasound in medicine & biology* **2014,** *40* (6), 1037-1048.

22. Yang, J. M.; Favazza, C.; Chen, R.; Yao, J.; Cai, X.; Maslov, K.; Zhou, Q.; Shung, K. K.; Wang, L. V., Simultaneous functional photoacoustic and ultrasonic endoscopy of internal organs in vivo. *Nature medicine* **2012,** *18* (8), 1297-1302.

23. Yang, J. M.; Maslov, K.; Yang, H. C.; Zhou, Q.; Shung, K. K.; Wang, L. V., Photoacoustic endoscopy. *Optics letters* **2009,** *34* (10), 1591-1593.

24. Wang, P.; Ma, T.; Slipchenko, M. N.; Liang, S.; Hui, J.; Shung, K. K.; Roy, S.; Sturek, M.; Zhou, Q.; Chen, Z.; Cheng, J. X., High-speed intravascular photoacoustic imaging of lipid-laden atherosclerotic plaque enabled by a 2-kHz barium nitrite raman laser. *Scientific reports* **2014,** *4*, 6889.

25. Xiong, K.; Yang, S.; Li, X.; Xing, D., Autofocusing optical-resolution photoacoustic endoscopy. *Optics letters* **2018,** *43* (8), 1846-1849.

26. Wu, M.; Springeling, G.; Lovrak, M.; Mastik, F.; Iskander-Rizk, S.; Wang, T.; van Beusekom, H. M.; van der Steen, A. F.; Van Soest, G., Real-time volumetric lipid imaging in vivo by intravascular photoacoustics at 20 frames per second. *Biomedical optics express* **2017,** *8* (2), 943-953.

27. Cao, Y.; Kole, A.; Hui, J.; Zhang, Y.; Mai, J.; Alloosh, M.; Sturek, M.; Cheng, J. X., Fast assessment of lipid content in arteries in vivo by intravascular photoacoustic tomography. *Scientific Reports* **2018,** *8* (1), 2400.

28. Yang, J. M.; Li, C.; Chen, R.; Zhou, Q.; Shung, K. K.; Wang, L. V., Catheter-based photoacoustic endoscope. *Journal of biomedical optics* **2014,** *19* (6), 066001.

29. Hui, J.; Cao, Y.; Zhang, Y.; Kole, A.; Wang, P.; Yu, G.; Eakins, G.; Sturek, M.; Chen, W.; Cheng, J. X., Real-time intravascular photoacoustic-ultrasound imaging of lipid-laden plaque in human coronary artery at 16 frames per second. *Scientific Reports* **2017,** *7* (1), 1417.

30. Bai, X.; Gong, X.; Hau, W.; Lin, R.; Zheng, J.; Liu, C.; Zeng, C.; Zou, X.; Zheng, H.; Song, L., Intravascular optical-resolution photoacoustic tomography with a 1.1 mm diameter catheter. *PLoS One* **2014,** *9* (3), e92463.

31. Liu, Z.; Wright, L. G.; Christodoulides, D. N.; Wise, F. W., Kerr self-cleaning of femtosecond-pulsed beams in graded-index multimode fiber. *Optics letters* **2016,** *41* (16), 3675-3678.

32. Ceoldo, D.; Krupa, K.; Tonello, A.; Couderc, V.; Modotto, D.; Minoni, U.; Millot, G.; Wabnitz, S., Second harmonic generation in multimode graded-index fibers:

spatial beam cleaning and multiple harmonic sideband generation. *Optics letters* **2017,** *42* (5), 971-974.

33. Mafi, A., Pulse propagation in a short nonlinear graded-index multimode optical fiber. *Journal of Lightwave Technology* **2012,** *30* (17), 2803-2811.

34. Guenard, R.; Krupa, K.; Dupiol, R.; Fabert, M.; Bendahmane, A.; Kermene, V.; Desfarges-Berthelemot, A.; Auguste, J. L.; Tonello, A.; Barthélémy, A.; Millot, G.; Wabnitz, S.; Couderc, V., Kerr self-cleaning of pulsed beam in an ytterbium doped multimode fiber. *Optics express* **2017,** *25* (5), 4783-4792.

35. Mocofanescu, A.; Wang, L.; Jain, R.; Shaw, K.; Gavrielides, A.; Peterson, P.; Sharma, M., SBS threshold for single mode and multimode GRIN fibers in an all fiber configuration. *Optics express* **2005,** *13* (6), 2019-2024.

36. Yang, J. M.; Li, C.; Chen, R.; Rao, B.; Yao, J.; Yeh, C. H.; Danielli, A.; Maslov, K.; Zhou, Q.; Shung, K. K.; Wang, L. V., Optical-resolution photoacoustic endomicroscopy in vivo. *Biomedical optics express* **2015,** *6* (3), 918-932.

37. Cannon, B., Cardiovascular disease: Biochemistry to behaviour. *Nature* **2013,** *493* (7434), S2-3.

38. Yahagi, K.; Kolodgie, F. D.; Otsuka, F.; Finn, A. V.; Davis, H. R.; Joner, M.; Virmani, R., Pathophysiology of native coronary, vein graft, and in-stent atherosclerosis. *Nature Reviews. Cardiology* **2016,** *13* (2), 79-98.

39. Schaar, J. A.; van der Steen, A. F.; Mastik, F.; Baldewsing, R. A.; Serruys, P. W., Intravascular palpography for vulnerable plaque assessment. *Journal of the American College of Cardiology* **2006,** *47* (8 Suppl), C86-91.

40. Jansen, K.; Wu, M.; van der Steen, A. F.; van Soest, G., Lipid detection in atherosclerotic human coronaries by spectroscopic intravascular photoacoustic imaging. *Optics express* **2013,** *21* (18), 21472-84.

41. Virmani, R.; Kolodgie, F. D.; Burke, A. P.; Farb, A.; Schwartz, S. M., Lessons from sudden coronary death: a comprehensive morphological classification scheme for atherosclerotic lesions. *Arteriosclerosis, thrombosis, and vascular biology* **2000,** *20* (5), 1262-1275.

42. Virmani, R.; Burke, A. P.; Farb, A.; Kolodgie, F. D., Pathology of the vulnerable plaque. *Journal of the American College of Cardiology* **2006,** *47* (8 Suppl), C13-18.

43. Li, Z. Y.; Howarth, S. P.; Tang, T.; Gillard, J. H., How critical is fibrous cap thickness to carotid plaque stability? A flow-plaque interaction model. *Stroke* **2006,** *37* (5), 1195-1199.

44. Kerwin, W. S.; Hatsukami, T.; Yuan, C.; Zhao, X. Q., MRI of carotid atherosclerosis. *AJR. American journal of roentgenology* **2013,** *200* (3), W304-313.

45. Makris, G. C.; Teng, Z.; Patterson, A. J.; Lin, J. M.; Young, V.; Graves, M. J.; Gillard, J. H., Advances in MRI for the evaluation of carotid atherosclerosis. *The British journal of radiology* **2015,** *88* (1052), 20140282.

46. Gogas, B. D.; Farooq, V.; Serruys, P. W.; Garcìa-Garcìa, H. M., Assessment of coronary atherosclerosis by IVUS and IVUS-based imaging modalities: progression and regression studies, tissue composition and beyond. *The international journal of cardiovascular imaging* **2011,** *27* (2), 225-237.

47. Honda, S.; Kataoka, Y.; Kanaya, T.; Noguchi, T.; Ogawa, H.; Yasuda, S., Characterization of coronary atherosclerosis by intravascular imaging modalities. *Cardiovascular diagnosis and therapy* **2016,** *6* (4), 368-381.

48. Yabushita, H.; Bouma, B. E.; Houser, S. L.; Aretz, H. T.; Jang, I. K.; Schlendorf, K. H.; Kauffman, C. R.; Shishkov, M.; Kang, D. H.; Halpern, E. F.; Tearney, G. J., Characterization of human atherosclerosis by optical coherence tomography. *Circulation* **2002,** *106* (13), 1640-1645.

49. Brugaletta, S.; Garcia-Garcia, H. M.; Serruys, P. W.; de Boer, S.; Ligthart, J.; Gomez-Lara, J.; Witberg, K.; Diletti, R.; Wykrzykowska, J.; van Geuns, R. J.; Schultz, C.; Regar, E.; Duckers, H. J.; van Mieghem, N.; de Jaegere, P.; Madden, S. P.; Muller, J. E.; van der Steen, A. F.; van der Giessen, W. J.; Boersma, E., NIRS and IVUS for characterization of atherosclerosis in patients undergoing coronary angiography. *JACC. Cardiovascular imaging* **2011,** *4* (6), 647-655.

50. Wang, B.; Su, J. L.; Karpiouk, A. B.; Sokolov, K. V.; Smalling, R. W.; Emelianov, S. Y., Intravascular Photoacoustic Imaging. *IEEE journal of quantum electronics* **2010,** *16* (3), 588-599.

51. Wu, M.; Fw van der Steen, A.; Regar, E.; van Soest, G., Emerging Technology Update Intravascular Photoacoustic Imaging of Vulnerable Atherosclerotic Plaque. *Interventional cardiology (London, England)* **2016,** *11* (2), 120-123.

52. Wei, W.; Li, X.; Zhou, Q.; Shung, K. K.; Chen, Z., Integrated ultrasound and photoacoustic probe for co-registered intravascular imaging. *Journal of biomedical optics* **2011,** *16* (10), 106001.

53. Wang, B.; Karpiouk, A.; Yeager, D.; Amirian, J.; Litovsky, S.; Smalling, R.; Emelianov, S., Intravascular photoacoustic imaging of lipid in atherosclerotic plaques in the presence of luminal blood. *Optics letters* **2012,** *37* (7), 1244-1246.

54. Wang, P.; Rajian, J. R.; Cheng, J. X., Spectroscopic Imaging of Deep Tissue through Photoacoustic Detection of Molecular Vibration. *The journal of physical chemistry letters* **2013,** *4* (13), 2177-2185.

55. Cao, Y.; Hui, J.; Kole, A.; Wang, P.; Yu, Q.; Chen, W.; Sturek, M.; Cheng, J. X., High-sensitivity intravascular photoacoustic imaging of lipid-laden plaque with a collinear catheter design. *Scientific Reports* **2016,** *6*, 25236.

56. Cao, Y.; Alloosh, M.; Sturek, M.; Cheng, J. X., Highly sensitive lipid detection and localization in atherosclerotic plaque with a dual‐frequency intravascular photoacoustic/ultrasound catheter. *Translational Biophotonics* **2020,** *2* (3), e202000004.

57. Jansen, K.; van der Steen, A. F.; van Beusekom, H. M.; Oosterhuis, J. W.; van Soest, G., Intravascular photoacoustic imaging of human coronary atherosclerosis. *Optics letters* **2011,** *36* (5), 597-599.

58. Jansen, K.; Wu, M.; van der Steen, A. F.; van Soest, G., Photoacoustic imaging of human coronary atherosclerosis in two spectral bands. *Photoacoustics* **2014,** *2* (1), 12-20.

59. Li, X.; Wei, W.; Zhou, Q.; Shung, K. K.; Chen, Z., Intravascular photoacoustic imaging at 35 and 80 MHz. *Journal of biomedical optics* **2012,** *17* (10), 106005.

60. VanderLaan, D.; Karpiouk, A. B.; Yeager, D.; Emelianov, S., Real-Time Intravascular Ultrasound and Photoacoustic Imaging. *IEEE transactions on ultrasonics, ferroelectrics, and frequency control* **2017,** *64* (1), 141-149.

61. Xie, Z.; Shu, C.; Yang, D.; Chen, H.; Chen, C.; Dai, G.; Lam, K. H.; Zhang, J.; Wang, X.; Sheng, Z.; Gao, D.; Liu, C.; Song, L.; Gong, X., In vivo intravascular photoacoustic imaging at a high speed of 100 frames per second. *Biomedical optics express* **2020,** *11* (11), 6721-6731.

62. Phinikaridou, A.; Hallock, K. J.; Qiao, Y.; Hamilton, J. A., A robust rabbit model of human atherosclerosis and atherothrombosis. *J of Lipid Research* **2009,** *50* (5), 787-97.

63. Taylor, E.; Huang, N.; Bodde, J.; Ellison, A.; Killiany, R.; Bachschmid, M. M.; Hamilton, J., MRI of atherosclerosis and fatty liver disease in cholesterol fed rabbits. *Journal of Translational Medicine* **2018,** *16* (1), 215.

64. Guan, Y.; Poon, L. L.; Cheung, C. Y.; Ellis, T. M.; Lim, W.; Lipatov, A. S.; Chan, K. H.; Sturm-Ramirez, K. M.; Cheung, C. L.; Leung, Y. H.; Yuen, K. Y.; Webster,

R. G.; Peiris, J. S., H5N1 influenza: a protean pandemic threat. *Proceedings of the National Academy of Sciences of the United States of America* **2004,** *101* (21), 8156-161.

65. Plourde, A. R.; Bloch, E. M., A Literature Review of Zika Virus. *Emerging infectious diseases* **2016,** *22* (7), 1185-92.

66. Baize, S.; Pannetier, D.; Oestereich, L.; Rieger, T.; Koivogui, L.; Magassouba, N.; Soropogui, B.; Sow, M. S.; Keïta, S.; De Clerck, H.; Tiffany, A.; Dominguez, G.; Loua, M.; Traoré, A.; Kolié, M.; Malano, E. R.; Heleze, E.; Bocquin, A.; Mély, S.; Raoul, H.; Caro, V.; Cadar, D.; Gabriel, M.; Pahlmann, M.; Tappe, D.; Schmidt-Chanasit, J.; Impouma, B.; Diallo, A. K.; Formenty, P.; Van Herp, M.; Günther, S., Emergence of Zaire Ebola virus disease in Guinea. *The New England journal of medicine* **2014,** *371* (15), 1418-1425.

67. Minor, P. D., Live attenuated vaccines: Historical successes and current challenges. *Virology* **2015,** *479-480*, 379-392.

68. Hudry, E.; Vandenberghe, L. H., Therapeutic AAV Gene Transfer to the Nervous System: A Clinical Reality. *Neuron* **2019,** *101* (5), 839-862.

69. Kaufman, H. L.; Kohlhapp, F. J.; Zloza, A., Oncolytic viruses: a new class of immunotherapy drugs. *Nature reviews. Drug discovery* **2015,** *14* (9), 642-662.

70. Feins, S.; Kong, W.; Williams, E. F.; Milone, M. C.; Fraietta, J. A., An introduction to chimeric antigen receptor (CAR) T-cell immunotherapy for human cancer. *American journal of hematology* **2019,** *94* (S1), S3-S9.

71. Kuznetsov, Y. G.; McPherson, A., Atomic force microscopy in imaging of viruses and virus-infected cells. *Microbiology and molecular biology reviews : MMBR* **2011,** *75* (2), 268-285.

72. Daaboul, G. G.; Freedman, D. S.; Scherr, S. M.; Carter, E.; Rosca, A.; Bernstein, D.; Mire, C. E.; Agans, K. N.; Hoenen, T.; Geisbert, T. W.; Ünlü, M. S.; Connor, J. H., Enhanced light microscopy visualization of virus particles from Zika virus to filamentous ebolaviruses. *PLoS one* **2017,** *12* (6), e0179728.

73. Kim, D.; Deerinck, T. J.; Sigal, Y. M.; Babcock, H. P.; Ellisman, M. H.; Zhuang, X., Correlative stochastic optical reconstruction microscopy and electron microscopy. *PLoS one* **2015,** *10* (4), e0124581.

74. Taylor, R. W.; Mahmoodabadi, R. G.; Rauschenberger, V.; Giessl, A.; Schambony, A.; Sandoghdar, V., Interferometric scattering microscopy reveals microsecond nanoscopic protein motion on a live cell membrane. *bioRxiv* **2018**, 401133.

75. Liao, Y. H.; Lin, C. H.; Cheng, C. Y.; Wong, W. C.; Juo, J. Y.; Hsieh, C. L., Monovalent and Oriented Labeling of Gold Nanoprobes for the High-Resolution Tracking of a Single-Membrane Molecule. *ACS nano* **2019,** *13* (10), 10918-10928.

76. Yurdakul, C.; Avci, O.; Matlock, A.; Devaux, A. J.; Quintero, M. V.; Ozbay, E.; Davey, R. A.; Connor, J. H.; Karl, W. C.; Tian, L.; Ünlü, M. S., High-Throughput, High-Resolution Interferometric Light Microscopy of Biological Nanoparticles. *ACS nano* **2020,** *14* (2), 2002-2013.

77. Young, G.; Hundt, N.; Cole, D.; Fineberg, A.; Andrecka, J.; Tyler, A.; Olerinyova, A.; Ansari, A.; Marklund, E. G.; Collier, M. P.; Chandler, S. A.; Tkachenko, O.; Allen, J.; Crispin, M.; Billington, N.; Takagi, Y.; Sellers, J. R.; Eichmann, C.; Selenko, P.; Frey, L.; Riek, R.; Galpin, M. R.; Struwe, W. B.; Benesch, J. L. P.; Kukura, P., Quantitative mass imaging of single biological macromolecules. *Science (New York, N.Y.)* **2018,** *360* (6387), 423-427.

78. Avci, O.; Ünlü, N. L.; Özkumur, A. Y.; Ünlü, M. S., Interferometric Reflectance Imaging Sensor (IRIS)--A Platform Technology for Multiplexed Diagnostics and Digital Detection. *Sensors (Basel, Switzerland)* **2015,** *15* (7), 17649-17665.

79. Ortega-Arroyo, J.; Kukura, P., Interferometric scattering microscopy (iSCAT): new frontiers in ultrafast and ultrasensitive optical microscopy. *Physical chemistry chemical physics : PCCP* **2012,** *14* (45), 15625-15636.

80. Taylor, R. W.; Sandoghdar, V., Interferometric Scattering Microscopy: Seeing Single Nanoparticles and Molecules via Rayleigh Scattering. *Nano letters* **2019,** *19* (8), 4827-4835.

81. Scherr, S. M.; Daaboul, G. G.; Trueb, J.; Sevenler, D.; Fawcett, H.; Goldberg, B.; Connor, J. H.; Ünlü, M. S., Real-Time Capture and Visualization of Individual Viruses in Complex Media. *ACS nano* **2016,** *10* (2), 2827-2833.

82. Daaboul, G. G.; Gagni, P.; Benussi, L.; Bettotti, P.; Ciani, M.; Cretich, M.; Freedman, D. S.; Ghidoni, R.; Ozkumur, A. Y.; Piotto, C.; Prosperi, D.; Santini, B.; Ünlü, M. S.; Chiari, M., Digital Detection of Exosomes by Interferometric Imaging. *Scientific reports* **2016,** *6*, 37246.

83. Monroe, M. R.; Daaboul, G. G.; Tuysuzoglu, A.; Lopez, C. A.; Little, F. F.; Unlü, M. S., Single nanoparticle detection for multiplexed protein diagnostics with attomolar sensitivity in serum and unprocessed whole blood. *Analytical chemistry* **2013,** *85* (7), 3698-3706.

84. Sevenler, D.; Trueb, J.; Ünlü, M. S., Beating the reaction limits of biosensor sensitivity with dynamic tracking of single binding events. *Proceedings of the National Academy of Sciences of the United States of America* **2019,** *116* (10), 4129-4134.

85. Kukura, P.; Ewers, H.; Müller, C.; Renn, A.; Helenius, A.; Sandoghdar, V., High-speed nanoscopic tracking of the position and orientation of a single virus. *Nature methods* **2009,** *6* (12), 923-927.

86. Ortega Arroyo, J.; Andrecka, J.; Spillane, K. M.; Billington, N.; Takagi, Y.; Sellers, J. R.; Kukura, P., Label-free, all-optical detection, imaging, and tracking of a single protein. *Nano letters* **2014,** *14* (4), 2065-2070.

87. Lindfors, K.; Kalkbrenner, T.; Stoller, P.; Sandoghdar, V., Detection and spectroscopy of gold nanoparticles using supercontinuum white light confocal microscopy. *Physical review letters* **2004,** *93* (3), 037401.

88. Jacobsen, V.; Stoller, P.; Brunner, C.; Vogel, V.; Sandoghdar, V., Interferometric optical detection and tracking of very small gold nanoparticles at a water-glass interface. *Optics express* **2006,** *14* (1), 405-414.

89. Nie, S.; Emory, S. R., Probing Single Molecules and Single Nanoparticles by Surface-Enhanced Raman Scattering. *Science (New York, N.Y.)* **1997,** *275* (5303), 1102-1106.

90. Zhang, X.; Zhang, X.; Luo, C.; Liu, Z.; Chen, Y.; Dong, S.; Jiang, C.; Yang, S.; Wang, F.; Xiao, X., Volume-Enhanced Raman Scattering Detection of Viruses. *Small (Weinheim an der Bergstrasse, Germany)* **2019,** *15* (11), e1805516.

91. Kukushkin, V. I.; Ivanov, N. M.; Novoseltseva, A. A.; Gambaryan, A. S.; Yaminsky, I. V.; Kopylov, A. M.; Zavyalova, E. G., Highly sensitive detection of influenza virus with SERS aptasensor. *PLoS one* **2019,** *14* (4), e0216247.

92. Yeh, Y. T.; Gulino, K.; Zhang, Y.; Sabestien, A.; Chou, T. W.; Zhou, B.; Lin, Z.; Albert, I.; Lu, H.; Swaminathan, V.; Ghedin, E.; Terrones, M., A rapid and label-free platform for virus capture and identification from clinical samples. *Proceedings of the National Academy of Sciences of the United States of America* **2020,** *117* (2), 895-901.

93. Olschewski, K.; Kämmer, E.; Stöckel, S.; Bocklitz, T.; Deckert-Gaudig, T.; Zell, R.; Cialla-May, D.; Weber, K.; Deckert, V.; Popp, J., A manual and an automatic TERS based virus discrimination. *Nanoscale* **2015,** *7* (10), 4545-4552.

94. Krafft, C.; Schmitt, M.; Schie, I. W.; Cialla-May, D.; Matthäus, C.; Bocklitz, T.; Popp, J., Label-Free Molecular Imaging of Biological Cells and Tissues by Linear and

Nonlinear Raman Spectroscopic Approaches. *Angewandte Chemie (International ed. in English)* **2017,** *56* (16), 4392-4430.

95. Hu, F.; Shi, L.; Min, W., Biological imaging of chemical bonds by stimulated Raman scattering microscopy. *Nature methods* **2019,** *16* (9), 830-842.

96. Matthäus, C.; Bird, B.; Miljković, M.; Chernenko, T.; Romeo, M.; Diem, M., Chapter 10: Infrared and Raman microscopy in cell biology. *Methods in cell biology* **2008,** *89*, 275-308.

97. Barth, A., Infrared spectroscopy of proteins. *Biochimica et biophysica acta* **2007,** *1767* (9), 1073-1101.

98. Hansen, L.; De Beer, T.; Pierre, K.; Pastoret, S.; Bonnegarde-Bernard, A.; Daoussi, R.; Vervaet, C.; Remon, J. P., FTIR spectroscopy for the detection and evaluation of live attenuated viruses in freeze dried vaccine formulations. *Biotechnology progress* **2015,** *31* (4), 1107-1118.

99. Brehm, M.; Taubner, T.; Hillenbrand, R.; Keilmann, F., Infrared spectroscopic mapping of single nanoparticles and viruses at nanoscale resolution. *Nano letters* **2006,** *6* (7), 1307-1310.

100. Li, X.; Zhang, D.; Bai, Y.; Wang, W.; Liang, J.; Cheng, J. X., Fingerprinting a Living Cell by Raman Integrated Mid-Infrared Photothermal Microscopy. *Analytical chemistry* **2019,** *91* (16), 10750-10756.

101. Taylor, R. W.; Sandoghdar, V., Interferometric scattering microscopy: seeing single nanoparticles and molecules via Rayleigh scattering. *Nano letters* **2019,** *19* (8), 4827-4835.

102. Hulst, H. C.; van de Hulst, H. C., *Light scattering by small particles*. Courier Corporation: 1981.

103. Yurdakul, C.; Ünlü, M. S., Computational nanosensing from defocus in single particle interferometric reflectance microscopy. *Optics letters* **2020,** *45* (23), 6546-6549.

104. Selmke, M.; Braun, M.; Cichos, F., Gaussian beam photothermal single particle microscopy. *Journal of the Optical Society of America. A, Optics, image science, and vision* **2012,** *29* (10), 2237-2241.

105. Gaiduk, A.; Yorulmaz, M.; Ruijgrok, P. V.; Orrit, M., Room-temperature detection of a single molecule's absorption by photothermal contrast. *Science (New York, N.Y.)* **2010,** *330* (6002), 353-356.

106. Berciaud, S.; Lasne, D.; Blab, G. A.; Cognet, L.; Lounis, B., Photothermal heterodyne imaging of individual metallic nanoparticles: Theory versus experiment. *Physical Review B* **2006,** *73* (4), 045424.

107. Li, Z.; Aleshire, K.; Kuno, M.; Hartland, G. V., Super-resolution far-field infrared imaging by photothermal heterodyne imaging. *The Journal of Physical Chemistry B* **2017,** *121* (37), 8838-8846.

108. van den Pol, A. N.; Dalton, K. P.; Rose, J. K., Relative neurotropism of a recombinant rhabdovirus expressing a green fluorescent envelope glycoprotein. *Journal of Virology* **2002,** *76* (3), 1309-1327.

109. Dower, K.; Rubins, K. H.; Hensley, L. E.; Connor, J. H., Development of Vaccinia reporter viruses for rapid, high content analysis of viral function at all stages of gene expression. *Antiviral Research* **2011,** *91* (1), 72-80.

110. Avci, O.; Adato, R.; Ozkumur, A. Y.; Ünlü, M. S., Physical modeling of interference enhanced imaging and characterization of single nanoparticles. *Optics Express* **2016,** *24* (6), 6094-6114.

111. Sevenler, D.; Avci, O.; Ünlü, M. S., Quantitative interferometric reflectance imaging for the detection and measurement of biological nanoparticles. *Biomedical Optics Express* **2017,** *8* (6), 2976-2989.

112. Pavlovetc, I. M.; Podshivaylov, E. A.; Chatterjee, R.; Hartland, G. V.; Frantsuzov, P. A.; Kuno, M., Infrared photothermal heterodyne imaging: Contrast mechanism and detection limits. *Journal of Applied Physics* **2020,** *127* (16), 165101.

113. Li, X.; Zhang, D.; Bai, Y.; Wang, W.; Liang, J.; Cheng, J.-X., Fingerprinting a Living Cell by Raman Integrated Mid-Infrared Photothermal Microscopy. *Analytical chemistry* **2019,** *91* (16), 10750-10756.

114. Harrison, S. C.; Alberts, B.; Ehrenfeld, E.; Enquist, L.; Fineberg, H.; McKnight, S. L.; Moss, B.; O'Donnell, M.; Ploegh, H.; Schmid, S. L., Discovery of antivirals against smallpox. *Proceedings of the National Academy of Sciences* **2004,** *101* (31), 11178-11192.

115. Sebba, D.; Lastovich, A. G.; Kuroda, M.; Fallows, E.; Johnson, J.; Ahouidi, A.; Honko, A. N.; Fu, H.; Nielson, R.; Carruthers, E., A point-of-care diagnostic for differentiating Ebola from endemic febrile diseases. *Science Translational Medicine* **2018,** *10* (471).

116. Yurdakul, C.; Avci, O.; Matlock, A.; Devaux, A. J.; Quintero, M. V.; Ozbay, E.; Davey, R. A.; Connor, J. H.; Karl, W. C.; Tian, L.; Selim, U., High-throughput, high-

resolution interferometric light microscopy of biological nanoparticles. *ACS nano* **2020,** *14* (2), 2002-2013.

117. Daaboul, G. G.; Freedman, D. S.; Scherr, S. M.; Carter, E.; Rosca, A.; Bernstein, D.; Mire, C. E.; Agans, K. N.; Hoenen, T.; Geisbert, T. W., Enhanced light microscopy visualization of virus particles from Zika virus to filamentous ebolaviruses. *PLoS One* **2017,** *12* (6), e0179728.

118. Zhang, Y.; Zong, H.; Zong, C.; Tan, Y.; Zhang, M.; Zhan, Y.; Cheng, J. X., Fluorescence-Detected Mid-Infrared Photothermal Microscopy. *Journal of the American Chemical Society* **2021,** *143* (30), 11490-11499.

119. Gonçalves, M. S. T., Fluorescent labeling of biomolecules with organic probes. *Chemical reviews* **2009,** *109* (1), 190-212.

120. Dean, K. M.; Palmer, A. E., Advances in fluorescence labeling strategies for dynamic cellular imaging. *Nature chemical biology* **2014,** *10* (7), 512-523.

121. Rust, M. J.; Bates, M.; Zhuang, X., Sub-diffraction-limit imaging by stochastic optical reconstruction microscopy (STORM). *Nature methods* **2006,** *3* (10), 793-796.

122. Gustafsson, M. G., Surpassing the lateral resolution limit by a factor of two using structured illumination microscopy. *Journal of microscopy* **2000,** *198* (2), 82-87.

123. Shroff, H.; Galbraith, C. G.; Galbraith, J. A.; Betzig, E., Live-cell photoactivated localization microscopy of nanoscale adhesion dynamics. *Nature methods* **2008,** *5* (5), 417-423.

124. Moschou, E. A.; Sharma, B. V.; Deo, S. K.; Daunert, S., Fluorescence glucose detection: advances toward the ideal in vivo biosensor. *Journal of fluorescence* **2004,** *14* (5), 535-547.

125. Mukherjee, S.; Zha, X.; Tabas, I.; Maxfield, F. R., Cholesterol distribution in living cells: fluorescence imaging using dehydroergosterol as a fluorescent cholesterol analog. *Biophysical journal* **1998,** *75* (4), 1915-1925.

126. Cheng, J.-X.; Xie, X. S., Vibrational spectroscopic imaging of living systems: An emerging platform for biology and medicine. *Science* **2015,** *350* (6264).

127. Cheng, J.-X.; Xie, X. S., Coherent anti-Stokes Raman scattering microscopy: instrumentation, theory, and applications. *The Journal of Physical Chemistry B* **2004,** *108* (3), 827-840.

128. Hu, F.; Shi, L.; Min, W., Biological imaging of chemical bonds by stimulated Raman scattering microscopy. *Nature methods* **2019,** *16* (9), 830-842.

129. Liao, C.-S.; Slipchenko, M. N.; Wang, P.; Li, J.; Lee, S.-Y.; Oglesbee, R. A.; Cheng, J.-X., Microsecond scale vibrational spectroscopic imaging by multiplex stimulated Raman scattering microscopy. *Light: Science & Applications* **2015,** *4* (3), e265-e265.

130. Yue, S.; Li, J.; Lee, S.-Y.; Lee, H. J.; Shao, T.; Song, B.; Cheng, L.; Masterson, T. A.; Liu, X.; Ratliff, T. L., Cholesteryl ester accumulation induced by PTEN loss and PI3K/AKT activation underlies human prostate cancer aggressiveness. *Cell metabolism* **2014,** *19* (3), 393-406.

131. Li, J.; Condello, S.; Thomes-Pepin, J.; Ma, X.; Xia, Y.; Hurley, T. D.; Matei, D.; Cheng, J.-X., Lipid desaturation is a metabolic marker and therapeutic target of ovarian cancer stem cells. *Cell stem cell* **2017,** *20* (3), 303-314. e5.

132. Du, J.; Su, Y.; Qian, C.; Yuan, D.; Miao, K.; Lee, D.; Ng, A. H.; Wijker, R. S.; Ribas, A.; Levine, R. D., Raman-guided subcellular pharmaco-metabolomics for metastatic melanoma cells. *Nature communications* **2020,** *11* (1), 1-16.

133. Fernandez, D. C.; Bhargava, R.; Hewitt, S. M.; Levin, I. W., Infrared spectroscopic imaging for histopathologic recognition. *Nature biotechnology* **2005,** *23* (4), 469-474.

134. Findlay, C.; Wiens, R.; Rak, M.; Sedlmair, J.; Hirschmugl, C.; Morrison, J.; Mundy, C.; Kansiz, M.; Gough, K., Rapid biodiagnostic ex vivo imaging at 1 μm pixel resolution with thermal source FTIR FPA. *Analyst* **2015,** *140* (7), 2493-2503.

135. Kazarian, S. G.; Chan, K. A., ATR-FTIR spectroscopic imaging: recent advances and applications to biological systems. *Analyst* **2013,** *138* (7), 1940-1951.

136. Lasch, P.; Haensch, W.; Naumann, D.; Diem, M., Imaging of colorectal adenocarcinoma using FT-IR microspectroscopy and cluster analysis. *Biochimica et Biophysica Acta (BBA)-Molecular Basis of Disease* **2004,** *1688* (2), 176-186.

137. Sattlecker, M.; Baker, R.; Stone, N.; Bessant, C., Support vector machine ensembles for breast cancer type prediction from mid-FTIR micro-calcification spectra. *Chemometrics and Intelligent Laboratory Systems* **2011,** *107* (2), 363-370.

138. Tang, J.; Luan, F.; Chen, X., Binding analysis of glycyrrhetinic acid to human serum albumin: Fluorescence spectroscopy, FTIR, and molecular modeling. *Bioorganic & medicinal chemistry* **2006,** *14* (9), 3210-3217.

139. Miller, L. M.; Bourassa, M. W.; Smith, R. J., FTIR spectroscopic imaging of protein aggregation in living cells. *Biochimica et biophysica acta (BBA)-biomembranes* **2013,** *1828* (10), 2339-2346.

140. Zlotogorski-Hurvitz, A.; Dekel, B. Z.; Malonek, D.; Yahalom, R.; Vered, M., FTIR-based spectrum of salivary exosomes coupled with computational-aided discriminating analysis in the diagnosis of oral cancer. *Journal of cancer research and clinical oncology* **2019,** *145* (3), 685-694.

141. Zhang, D.; Li, C.; Zhang, C.; Slipchenko, M. N.; Eakins, G.; Cheng, J.-X., Depth-resolved mid-infrared photothermal imaging of living cells and organisms with submicrometer spatial resolution. *Science advances* **2016,** *2* (9), e1600521.

142. Bai, Y.; Zhang, D.; Li, C.; Liu, C.; Cheng, J.-X., Bond-selective imaging of cells by mid-infrared photothermal microscopy in high wavenumber region. *The Journal of Physical Chemistry B* **2017,** *121* (44), 10249-10255.

143. Lim, J. M.; Park, C.; Park, J.-S.; Kim, C.; Chon, B.; Cho, M., Cytoplasmic protein imaging with mid-infrared photothermal microscopy: cellular dynamics of live neurons and oligodendrocytes. *The journal of physical chemistry letters* **2019,** *10* (11), 2857-2861.

144. Shi, J.; Wong, T. T.; He, Y.; Li, L.; Zhang, R.; Yung, C. S.; Hwang, J.; Maslov, K.; Wang, L. V., High-resolution, high-contrast mid-infrared imaging of fresh biological samples with ultraviolet-localized photoacoustic microscopy. *Nature photonics* **2019,** *13* (9), 609-615.

145. Yeran Bai, J. Y., Ji-Xin Cheng, Bond-Selective Imaging by Optically Sensing the Mid-Infrared Photothermal Effect *Science advances* **2021,** *In press*.

146. Zhang, D.; Lan, L.; Bai, Y.; Majeed, H.; Kandel, M. E.; Popescu, G.; Cheng, J.-X., Bond-selective transient phase imaging via sensing of the infrared photothermal effect. *Light: Science & Applications* **2019,** *8* (1), 1-12.

147. Bai, Y.; Zhang, D.; Lan, L.; Huang, Y.; Maize, K.; Shakouri, A.; Cheng, J.-X., Ultrafast chemical imaging by widefield photothermal sensing of infrared absorption. *Science advances* **2019,** *5* (7), eaav7127.

148. Schnell, M.; Mittal, S.; Falahkheirkhah, K.; Mittal, A.; Yeh, K.; Kenkel, S.; Kajdacsy-Balla, A.; Carney, P. S.; Bhargava, R., All-digital histopathology by infrared-optical hybrid microscopy. *Proceedings of the National Academy of Sciences* **2020,** *117* (7), 3388-3396.

149. Tamamitsu, M.; Toda, K.; Shimada, H.; Honda, T.; Takarada, M.; Okabe, K.; Nagashima, Y.; Horisaki, R.; Ideguchi, T., Label-free biochemical quantitative phase imaging with mid-infrared photothermal effect. *Optica* **2020,** *7* (4), 359-366.

150. Li, C.; Zhang, D.; Slipchenko, M. N.; Cheng, J.-X., Mid-infrared photothermal imaging of active pharmaceutical ingredients at submicrometer spatial resolution. *Analytical chemistry* **2017,** *89* (9), 4863-4867.

151. Xu, J.; Li, X.; Guo, Z.; Huang, W. E.; Cheng, J.-X., Fingerprinting Bacterial Metabolic Response to Erythromycin by Raman-Integrated Mid-Infrared Photothermal Microscopy. *Analytical Chemistry* **2020,** *92* (21), 14459-14465.

152. Marcott, C.; Kansiz, M.; Dillon, E.; Cook, D.; Mang, M. N.; Noda, I., Two-dimensional correlation analysis of highly spatially resolved simultaneous IR and Raman spectral imaging of bioplastics composite using optical photothermal Infrared and Raman spectroscopy. *Journal of Molecular Structure* **2020,** *1210*, 128045.

153. Klementieva, O.; Sandt, C.; Martinsson, I.; Kansiz, M.; Gouras, G. K.; Borondics, F., Super‐Resolution Infrared Imaging of Polymorphic Amyloid Aggregates Directly in Neurons. *Advanced Science* **2020,** *7* (6), 1903004.

154. Banas, A.; Banas, K.; Lo, M. K. F.; Kansiz, M.; Kalaiselvi, S. M. P.; Lim, S. K.; Loke, J.; Breese, M. B. H., Detection of High-Explosive Materials within Fingerprints by Means of Optical-Photothermal Infrared Spectromicroscopy. *Analytical Chemistry* **2020,** *92* (14), 9649-9657.

155. Zhang, Y.; Yurdakul, C.; Devaux, A. J.; Wang, L.; Xu, X. G.; Connor, J. H.; Ünlü, M. S.; Cheng, J.-X., Vibrational Spectroscopic Detection of a Single Virus by Mid-Infrared Photothermal Microscopy. *Analytical Chemistry* **2021**.

156. Grabowski, Z. R.; Rotkiewicz, K.; Rettig, W., Structural changes accompanying intramolecular electron transfer: focus on twisted intramolecular charge-transfer states and structures. *Chemical reviews* **2003,** *103* (10), 3899-4032.

157. Chen, Y. Y.; Wood, A. W., Application of a temperature‐dependent fluorescent dye (Rhodamine B) to the measurement of radiofrequency radiation‐induced temperature changes in biological samples. *Bioelectromagnetics: Journal of the Bioelectromagnetics Society, The Society for Physical Regulation in Biology and Medicine, The European Bioelectromagnetics Association* **2009,** *30* (7), 583-590.

158. Gosse, C.; Bergaud, C.; Löw, P., Molecular probes for thermometry in microfluidic devices. *Thermal Nanosystems and Nanomaterials* **2009**, 301-341.

159. Maksimov, E. G.; Yaroshevich, I. A.; Tsoraev, G. V.; Sluchanko, N. N.; Slutskaya, E. A.; Shamborant, O. G.; Bobik, T. V.; Friedrich, T.; Stepanov, A. V., A genetically encoded fluorescent temperature sensor derived from the photoactive Orange Carotenoid Protein. *Scientific reports* **2019,** *9* (1), 1-9.

160. Greenspan, P.; Mayer, E. P.; Fowler, S. D., Nile red: a selective fluorescent stain for intracellular lipid droplets. *The Journal of cell biology* **1985,** *100* (3), 965-973.

161. Baracca, A.; Sgarbi, G.; Solaini, G.; Lenaz, G., Rhodamine 123 as a probe of mitochondrial membrane potential: evaluation of proton flux through F0 during ATP synthesis. *Biochimica et biophysica acta (BBA)-bioenergetics* **2003,** *1606* (1-3), 137-146.

162. Zhang, C.; Liu, M.-S.; Xing, X.-H., Temperature influence on fluorescence intensity and enzyme activity of the fusion protein of GFP and hyperthermophilic xylanase. *Applied microbiology and biotechnology* **2009,** *84* (3), 511-517.

163. Donner, J. S.; Thompson, S. A.; Kreuzer, M. P.; Baffou, G.; Quidant, R., Mapping intracellular temperature using green fluorescent protein. *Nano letters* **2012,** *12* (4), 2107-2111.

164. Whaley-Mayda, L.; Penwell, S. B.; Tokmakoff, A., Fluorescence-Encoded Infrared Spectroscopy: Ultrafast Vibrational Spectroscopy on Small Ensembles of Molecules in Solution. *The journal of physical chemistry letters* **2019,** *10* (8), 1967-1972.

165. Xiong, H.; Shi, L.; Wei, L.; Shen, Y.; Long, R.; Zhao, Z.; Min, W., Stimulated Raman excited fluorescence spectroscopy and imaging. *Nature photonics* **2019,** *13* (6), 412-417.

166. Li, M.; Razumtcev, A.; Yang, R.; Liu, Y.; Rong, J.; Geiger, A. C.; Blanchard, R.; Pfluegl, C.; Taylor, L. S.; Simpson, G. J., Fluorescence-Detected Mid-Infrared Photothermal Microscopy. *arXiv preprint arXiv:2104.02900* **2021**.

167. Lienhard, I.; John, H., *A heat transfer textbook*. Phlogiston press: 2005.

168. Marín, E., Characteristic dimensions for heat transfer. *Latin-American Journal of Physics Education* **2010,** *4* (1), 56-60.

169. James, D., The thermal diffusivity of ice and water between− 40 and+ 60° C. *Journal of Materials Science* **1968,** *3* (5), 540-543.

170. Liu, W. T.; Wu, J. H.; Li, E. S.; Selamat, E. S., Emission characteristics of fluorescent labels with respect to temperature changes and subsequent effects on DNA microchip studies. *Applied and Environmental Microbiology* **2005,** *71* (10), 6453-6457.

171. Ogle, M. M.; Smith McWilliams, A. D.; Ware, M. J.; Curley, S. A.; Corr, S. J.; Martí, A. A., Sensing Temperature in Vitro and in Cells Using a BODIPY Molecular Probe. *Journal of Physical Chemistry. B* **2019,** *123* (34), 7282-7289.

CURRICULUM VITAE